UNIVERSITY OF SOUTHAMPTON
FACULTY OF ENGINEERING, SCIENCE AND MATHEMATICS
INSTITUTE OF SOUND AND VIBRATION RESEARCH

CONTROL OF FLEXURAL WAVES ON A BEAM USING A SELF-TUNING VIBRATION ABSORBER

by

Hassan M. El-Khatib

Thesis submitted for the degree of Doctor of Philosophy

May 2005

UNIVERSITY OF SOUTHAMPTON

ABSTRACT

FACULTY OF ENGINEERING, SCIENCE AND MATHEMATICS

INSTITUTE OF SOUND AND VIBRATION RESEARCH

DOCTOR OF PHILOSOPHY

CONTROL OF FLEXURAL WAVES ON A BEAM USING A SELF-TUNING VIBRATION ABSORBER

by Hassan Mohsen El-Khatib

This thesis concerns the control of bending waves in beams using a self-tuning vibration absorber. An adaptive-passive vibration absorber, whose natural frequency is tuned automatically by adjusting the stiffness of the absorber, is developed and implemented.

The transmission and reflection of waves at an absorber attached to a beam are considered. The absorber may be located in the farfield or the nearfield of a point force and it can be positioned to control both the downstream-transmitted power and that reflected upstream. Analytical and numerical investigations are presented. If the absorber is located in the nearfield of the point force, the power transmitted past the absorber depends on four independent tuning parameters: the natural frequency of the absorber, the mass ratio, the damping of the absorber and the distance between the absorber and the point force. If the incident nearfield wave is insignificant, then this distance becomes unimportant in determining the optimal characteristics of the absorber for the control of vibration transmission. It is found that the absorber typically acts as a notch filter, controlling transmission over a narrow range of frequencies.

The case of a tunable absorber is then considered. The stiffness of such an absorber can be changed, thus affecting the tuned frequency. Two variable stiffness absorbers are designed. The stiffnesses of both change with temperature and electrical heating is used to change the absorber characteristics. The first absorber uses shape memory alloy as the variable stiffness element, while the second absorber employs thermoset plastics.

A closed-loop control system is developed using an appropriate error function to control the transmitted waves in real-time. The error function is found by combining the outputs of two sensors attached to the beam, one on each side of the absorber. The error function indicates the degree of mistune and whether the absorber's stiffness needs to increase or decrease to minimise the magnitude of the transmitted power. Numerical simulations are presented. These show the effectiveness of the control system, employing the error function and an adaptive absorber, in varying the stiffness of the absorber towards the optimum value.

Experimental implementation of real-time control of the adaptive-passive absorber which implements thermoset plastics as the variable stiffness element is shown to be effective in reducing the transmitted power on a beam.

ACKNOWLEDGMENTS

First and foremost I would like to express my sincere thanks to my supervisors, Professor Brian Mace and Professor Michael Brennan, for their invaluable assistance and guidance throughout this research project.

I am grateful to Dr Roger Halkyard and Dr Emiliano Rustighi for their advice on some of the software used in this project.

Thanks must also be given to Mr Dave Edwards for his help with the manufacture of the experimental rigs used in this thesis.

Finally, I must thank my wife, Souraya, and family for their tolerance and understanding shown throughout the duration of the thesis.

TABLE OF CONTENTS

APPENDICES

LIST OF FIGURES

——— $T_a = 21°C$; .... $T = 33°C$; ------ $T = 45°C$; -·-·-·- $T = 68°C$.

Figure 6.4. Experimental set-up for the self-tuning control:

○ accelerometer.

Figure 6.5. Real-time control of the farfield vibration for 3000 sec at an instantaneous frequency increase from 314 to 420 Hz at 1000 sec.

(a) error function; (b) electric current; (c) envelope of acceleration amplitudes at upstream——— A_{Ref} and downstream ·············· A_{Tra} location.

Figure 6.6. Real-time control of the farfield vibration for 3000 sec at an instantaneous frequency decrease from 420 to 314 Hz at 500 sec.

(a) error function; (b) electric current; (c) envelope of acceleration amplitudes at upstream——— A_{Ref} and downstream ·············· A_{Tra} location.

LIST OF TABLES

CHAPTER 1: INTRODUCTION

1.1 Background

There is a strong need for effective vibration control techniques in nearly every branch of engineering. These techniques are required to reduce the levels of vibration caused by disturbances to an acceptable level. In most vibrating systems, there are three possible transmission paths for vibration transmission and noise radiation to sensitive positions remote from a vibrating device (e.g. engines, pump etc). These are the acoustic radiation via the surrounding medium; the transmission of structural vibration through the system mounts; and the transmission of structural vibration through connecting structures to the receiver. In many cases, these linking structures are represented by one-dimensional elements, of which beams are among the most commonly used in engineering systems (e.g. space structures, automotive industries, building structure etc). These elements act as paths of structure-borne vibration where vibration transmits from one part of the structure to another.

The vibration transmission on a beam structure is controlled in this thesis using a self-tuning adaptive-passive vibration absorber.

1.1.1 Tuned vibration absorber

One well established device used to reduce the vibration amplitude of a vibrating machine or structure over a specific frequency range is the tuned vibration absorber (TVA). The vibration absorber comprises a tuned, secondary, resonant subsystem. In its conventional form it comprises a spring-mass-damper system used to control the vibration at the point to which it is attached [1, 2]. The system needs to be tuned accurately to reduce the vibrations effectively.

There are two classical uses for the absorber, and the tuning rules differ for each [3, 4]. In both cases the bandwidth and the effects of mistune depend on the absorber mass. The first case is where the disturbance is narrowband with a known fixed frequency. Optimal performance is provided by an undamped tuned absorber, also called a dynamic absorber, or vibration neutraliser. The natural frequency of the absorber is tuned to a troublesome excitation frequency offering very large mechanical impedance. The presence of damping deteriorates the performance somewhat. In the second case the absorber acts as a tuned damper and it is appropriate for broadband disturbances. The absorber is tuned to a problematic resonance of the host structure and an optimum amount of damping is included to reduce the motion of the vibrating structure at frequencies close to the resonance frequency.

The traditional absorbers with their fixed characteristics are called passive absorbers and can be very effective in suppressing the vibrations induced in a structure excited by a harmonic disturbance such as a machine running at a constant speed. Under these steady operating conditions, passive absorbers provide stability and robustness. However, even small amounts of mistune, or small changes in the operating frequency of the harmonic disturbance, can severely deteriorate the performance of the absorber [3, 5]. One way to overcome these problems is to implement fully active or semi-active control techniques.

1.1.2 Adaptive-passive vibration absorbers

Fully active vibration control systems involve the application of additional control forces to the vibrating system in order to cancel the vibrations produced by the original disturbance [4, 6]. Active systems can, in principle, offer much improved performance and higher control authority. Nevertheless, they are more complex, can potentially cause instability and require external power input. Furthermore, the failure of this control technique can expose the structure to high levels of vibration.

An alternative to active control is the adaptive-passive technique, also called semi-active, which is the control method adopted in this thesis. In this method, secondary forces are generated passively by a device whose characteristics can be adapted with time so that the passive system is at its most effective. In contrast to active methods, adaptive-passive strategies add no energy to the system, and require minimal power for activation. Therefore, this technique has no potential for instability. In addition, the adaptive-passive technique overcomes the disadvantages of many passive control solutions which must be precisely tuned, and cannot re-tune, and thus are only effective over a fixed, narrow frequency band [4-8].

Many designs for adaptive-tuned vibration absorbers (ATVAs) have been developed in the past to suppress the vibration of structures subjected to a variable troublesome forcing frequency. The stiffness element of the ATVA is adjustable so that the device can be retuned over a reasonable range of frequencies. Methods previously used for varying the stiffness element of the ATVAs can probably be summarised in two categories.

The first group concerns utilising smart materials in the ATVA. These materials are capable of changing their stiffness with an appropriate actuation. For instance, piezoelectric ceramic elements have been used as part of the ATVA's stiffness in many applications [9-11]. The effective stiffness of these elements was adjusted electrically to tune the resonance frequency of the device. Shape memory alloys (SMA) with their variable material properties have been recently implemented in designing ATVAs [12, 13]. The SMAs undergo a crystalline phase change when heated or cooled above certain temperatures, and this phase change is accompanied by a change in the elastic properties.

The second group concerns designing ATVAs with smart structures. Walsh and Lamancusa [14] have established an ATVA by controlling the separation between two leaf springs using a stepper motor to tune the resonance frequency. Further developments on that design have been introduced by Brennan [15] and Kidner and Brennan [16]. Changing the length of a beam absorber with a mass supported at its centre has effectively varied the tuned frequency as described by Hong and Ryu [17] where the beam stiffness is inversely proportional to the cube of the length. Franchek *et al* [18] proposed a variable stiffness absorber by simply adjusting the effective length of a coil spring by means of a D.C. motor. A recent design by Carneal *et al* [19] called the "V" type ATVA proposes an ATVA with a stepper motor to act as its active mass. The motor moves the supporting ends to change the flexural stiffness of the supporting shafts of the VATVA. Bonello *et al* [20] proposed an ATVA that uses two variable curvature beams as stiffness elements. Each curved beam consists of a piezoceramic layer sandwiched between an aluminium layer and a steel plate. The beams are supported on ball bearings at their ends, allowing freedom of rotation. The absorber mass is supported on bearings and guided vertically by a linear bearing running on the central column that is fixed to the base. The curvature of the beams is changed by adjusting the level of dc voltage applied to the piezoelectric layers. Another recent model is proposed by Cronje *et al* [21] and utilised paraffin wax to control the separation of two leaf springs. The wax is contained in a small copper cup. When the wax is heated by means of a hot-air gun, it changes from solid to liquid state with an associated volume change.

Other tuning mechanisms are also reviewed by Sun *et al* [4] and Von Flotow *et al* [7].

1.1.3 Applications of vibration suppression using adaptive absorbers

Details noted by Von Flotow *et al* [7] refer to the use of three cantilever-type adaptive self-tuning absorbers installed under the cockpit floor of the Boeing CH-47C. The absorbers are adaptively tuned to the blade passage frequency by repositioning the counterweights on the beam. An open loop control strategy was implemented where the phase relationship between the vibrations of the helicopter and the mass was evaluated and compared to the predetermined relationship for proper tune.

Long *et al* [22] implemented a two-tier approach to adaptively control a vibration absorber by adjusting the pressure in a pneumatic spring. An open-loop control was used to tune the absorber roughly, such that its working frequency was within its 3 dB bandwidth, then a closed-loop algorithm was implemented to tune the absorber precisely by forcing the main system mass and the absorber mass to vibrate in quadrature. The closed-loop algorithm utilised the steepest descent method and successful results were obtained.

A controller with a multi-objective fuzzy logic algorithm was proposed by Lai and Wang [23] for dynamic absorbers with variable stiffness to suppress structural vibrations, but only numerical simulations are presented and no means for adjusting the stiffness are described. However, Kidner and Brennan [24] designed a fuzzy controller to adjust the resonance frequency of a beam-like absorber by changing its geometry, and to adjust the gain in a velocity feedback loop to reduce the damping in the device. Reducing the damping at the tuned frequency was found to improve the accuracy of the tuning algorithm.

In recent years smart materials have been used extensively in vibration absorbers. Rustighi *et al* [12] designed a beam-like absorber made of Nitinol wires. This type of shape memory alloy is the most widely used due to its effective performance. The adaptive absorber has been tested experimentally and controlled in real-time to suppress the vibrations at the point of application. Various control algorithms were used, with proportional derivative (PD) method being the most effective. The error function chosen to be minimised was the phase between velocities of the machine and the absorber masses.

Self-tuning implementations of adaptive absorbers are still few in number and the majority concerns the suppression of vibration at a single point. In this thesis the emphasis is on the control of structure borne vibrations induced in beams using a single adaptive-passive vibration absorber.

1.1.4 Control of flexural waves on beam structures

The control of flexural waves has been discussed by many researchers over the past ten years, most of them concerned with the implementation of active control strategies. Elliot and Billet [25] introduced an active control system to suppress an incident flexural wave propagating on a beam. The control system consists of a number of elements: detection sensor, feedforward controller, secondary actuator and an error sensor. The aim of the controller was to drive the total acceleration at the error sensor position to zero. An analytical expression for the ideal controller was found. Practical results showed significant reduction in acceleration at the error sensor. Both primary and secondary excitations were generated by a coil suspended in a fixed magnetic field. An improved feedforward active control of an incident flexural wave on a beam was proposed by Halkyard and Mace [26]. Here the propagating wave amplitude in the farfield was estimated in real-time by combining and filtering the output of two velocity sensors. This avoids the problem of sensitivity and the errors introduced by using the conventional sensor-based measurement when nearfield components and noise are present.

Smart materials and structures have also been used in controlling the flexural waves propagating on beam structures. Harland *et al* [27] introduced a system comprising a tunable structural insert in a one-dimensional waveguide to control the transmission of bending waves. An auto-tuning scheme was described. The system uses a sensor to provide a measure of the vibration level downstream of the insert, and an adaptive algorithm in the feedback loop which changes the field applied to the tunable insert. A very simple algorithm was used to demonstrate the applicability of the technique. Numerical examples were presented for electro-rheological (ER) fluid-filled inserts. The tunability of these inserts is not very large due the physical properties of the fluid [28].

Clark [29] and Brennan [30] presented analytical and experimental work showing that significant suppression of a flexural wave propagating on a beam can be achieved by attaching a single tuned vibration absorber. The absorber was modelled as a point translational impedance in the farfield of a disturbance.

The disadvantages of the active control techniques and the use of smart structural inserts to control the flexural waves propagating on beams have encouraged the use of self-tuning vibration absorbers.

1.2 Aim and Objectives

The aim of the research reported in this thesis is to develop a self-tuning adaptive-passive vibration absorber to control the structure-borne vibration in beam-like structural members. Such vibrations arise from some source such as a machine, pump or engine, and the vibrational energy travels through the structure as waves, eventually reaching some remote vibration-sensitive region. The system as a whole is a smart structure, involving sensors (to detect the appropriate error function which needs to be minimised), control (to determine the optimal characteristics of the absorber based on the detected error function) and means for adapting the physical properties of the device using smart materials.

Accordingly the main objectives of this work were to:

- Model a vibration absorber attached as a point translational impedance to an infinite beam at a distance from a point disturbance.
- Investigate the absorber's tuning parameters that would satisfy the minimum power transmission or maximum absorption taking into consideration the effect of nearfield waves.
- Design and construct a tunable vibration absorber that would effectively control the transmitted power over a range of frequencies.
- Find an appropriate error function that would indicate the tuning direction of the absorber stiffness to satisfy the minimum power transmission.
- Implement the self-tuning absorber to control the vibration transmission in real-time using a simple algorithm that utilises the error function in an application in which the disturbance is tonal, but with a frequency that may vary with time.

1.3 Novel Contributions

It should be noted that neither the concept of the self-tuning vibration absorber nor the concept of controlling the vibration transmission in beam structures is novel. However, the application of these two ideas in conjunction with one another has resulted in a novel approach to this vibration engineering problem. The original contributions achieved in this thesis are briefly listed below:

- Modelling a tuned vibration absorber located in either the nearfield or the farfield of a harmonic point force and its effect on the control of transmitted flexural waves.
- Controlling both the downstream transmitted power and that reflected upstream of a point force by positioning the tuned absorber at optimum locations along a beam structure.
- Designing a simple adaptive-passive vibration absorber using smart materials to control the flexural waves on a beam.

- Determining an appropriate error function that indicates both the performance of the adaptive-passive vibration absorber and the direction of required tuning.
- Implementing a self-tuning adaptive-passive vibration absorber to control the power transmission in a beam structure.

1.4 Overview of the Thesis

Wave propagation in rods and beams is reviewed in Chapter 2. The principle types of wave motion are discussed and the equations of motion are stated with emphasis on the understanding of flexural waves which need to be controlled. Methods for measuring the amplitude of propagating waves and the flexural wavenumber are described. An example of the experimental measurement of the wavenumber is presented. This wavenumber will be used in the following chapters in the design of the devices to suppress the flexural waves. The reflection and transmission of flexural waves due to point discontinuities are discussed.

Chapter 3 provides a wave model of a tuned vibration absorber attached to a beam. Analytical expressions for the power transmitted and reflected are derived as functions of independent tuning parameters. The optimal tuning parameters of the absorber are investigated analytically and numerically. Experimental validation of the theoretical predictions is reported using a passive vibration absorber.

The effect of varying the absorber stiffness on the control of the flexural waves is discussed in Chapter 4. A simple design of an adaptive-tuned vibration absorber that implements wires of Nitinol (SMA) is proposed and constructed. The Nitinol wires are held together at the centre using epoxy-resins. Following the experimental validation of the performance of the SMA ATVA, another variable stiffness absorber is constructed and proved effective. This adaptive absorber only implements epoxy-resins as the variable stiffness elements. The properties of the materials chosen to be implemented in the absorbers are investigated. Experimental results validating the tunability of the absorbers are presented showing the effectiveness of the ATVA that only implements epoxy-resins compared with the performance of the SMA ATVA.

Chapter 5 describes some possible control strategies that can be implemented to achieve a self-tuning control system to suppress the flexural propagating waves. One optimisation method is considered; this is the gradient descent algorithm. An appropriate error function that indicates the degree of mistune and the direction towards the optimum tuning, at which the transmitted power is minimum, is presented. Numerical simulations showing the effectiveness of the control algorithm which employs the error function, in varying the stiffness of an ATVA towards the optimum value, is presented.

Following on from the work introduced in previous chapters, Chapter 6 presents experimental implementation of real-time control of the adaptive-passive absorber, which implements epoxy-resins as the variable stiffness elements, to suppress the transmitted vibration. Prior to the experimental control, the effectiveness of the error function in indicating the optimum direction for tuning is validated.

Finally, Chapter 7 includes a summary of the main conclusions from this work and recommendations for further study.

CHAPTER 2: WAVE MOTION IN ONE-DIMENSIONAL STRUCTURAL ELEMENTS

2.1 Introduction

In Chapter 1 propagating waves on a beam and possible methods that could be used to control these waves were discussed. The design of efficient control methods requires understanding of the behaviour of waves in one-dimensional structures. This is considered in this chapter.

From the fundamental knowledge describing the motion in beam-like structures, expressions for the transmitted power in one-dimensional structural elements can be determined. In this chapter, elastic wave motion in these elements is addressed. Such elements are represented by rods, beams and pipes vibrating at low frequency. The principle types of wave motion through which energy may propagate in this class of structure are longitudinal motion, torsional motion and flexural motion.

The chapter is organised in 6 sections. Following this introduction, section 2.2 discusses the principle types of wave motion in one-dimensional structural elements. Particular attention is focused on flexural wave motion in beam structures for reasons which will be discussed. The energy flow in beams is discussed in section 2.3. Methods for measuring the beam wavenumber and estimating the propagating wave amplitudes are illustrated in section 2.4. An experimental example of measuring a beam wavenumber is also included. The reflection and transmission of flexural waves due to point discontinuities are discussed in Section 2.5. Finally, in section 2.6 some conclusions are drawn.

2.2 Wave Propagation

Vibrations propagate through structures as waves. A wave can be described as a disturbance that travels through the medium from one location to another. To understand fully the nature of a wave, one can consider the medium as a series of interconnected elements or particles. The interaction of one element in the medium with the next adjacent one allows the disturbance to travel through the medium. Therefore, a mechanical wave can be defined as a phenomenon in which a physical quantity (e.g. energy or strain) propagates in a medium without net transport of the medium [31, 32]. Accordingly, a wave is a means of transmitting energy from one point to another. The principle types of structural wave motion are introduced in this section.

2.2.1 Longitudinal waves

The wave in which the direction of motion of the particles coincides with the direction of wave propagation is defined as the longitudinal wave or the axial wave. Figure 2.1 shows an element of an elastic uniform beam or rod, of length δx, undergoing longitudinal motion. It should be noted that pure longitudinal motion could only occur in solids whose dimensions in all directions are much greater than a wavelength [33]. However, for a bar undergoing low frequency in-plane motion, the dimensions of the cross-section of the bar will be very much less than the resulting wavelength. For this case, contraction in the cross-section of the bar occurs in addition to the axial extension. Because of the cross-contraction phenomenon, lateral displacements occur in addition to the longitudinal displacement, and therefore a wave travelling along the bar cannot be a pure longitudinal one. The motion for this case can be described as quasi-longitudinal wave motion [33].

Assuming the longitudinal displacement $u(x)$ is uniform over the normal cross-sectional area A and the lateral deflection is insignificant then consideration of the conditions for the dynamic equilibrium of the beam element, under axial stress σ_x, and shown in Figure 2.1 yields the equation of motion in the x-direction [34]

$$E\frac{\partial^2 u}{\partial x^2} = \rho\frac{\partial^2 u}{\partial t^2}, \tag{2.1}$$

where E and ρ are respectively the Young's modulus and the density of the rod material. The solution to this second order differential equation is, for a time harmonic motion, of the form $\exp(i\omega t)$ e.g. [33-35]

$$u(x,t) = a^{+}e^{i(\omega t - k_l x)} + a^{-}e^{i(\omega t + k_l x)}, \tag{2.2}$$

where $k_l = \omega\sqrt{\rho / E}$ is the longitudinal wavenumber and ω is the circular frequency. The wavenumber indicates the phase change per unit length. A phase change of 2π occurs over a distance of one wavelength λ (the distance over which a complete cycle occurs [36]). Thus $k = 2\pi / \lambda$. Hereafter, the harmonic time dependence $e^{i\omega t}$ will be suppressed. The solution consists of two waves harmonic in space and time: a^{+} is a wave travelling in the positive x-direction and is called a positive-going propagating wave, while the wave a^{-} is travelling in the negative direction and is called a negative-going propagating wave.

It is worthy of note that the longitudinal waves are non-dispersive, in that the phase velocity (the speed at which a wave propagates in a structure) of the longitudinal waves $c_l = \omega / k_l$ does not vary with frequency (all harmonic waves travel at the same velocity).

Torsional waves may also propagate in one-dimensional structures. The governing equation for torsional motion is identical in form to that of longitudinal motion, see for example [37]. Similar to longitudinal waves, the torsional waves are also non-dispersive.

2.2.2 Flexural waves

When a beam is excited transversely, it gives rise to flexural wave motion in the structure. If the excitation frequency is low (the resulting wavelength is large compared to the beam dimensions) then the high frequency effects associated with the shear deformation and rotary inertia of the cross-section can be assumed to be negligible. For this case, the motion is described by the simple "Euler-Bernoulli" beam theory [33, 37]. The theory assumes that plane sections remain plane and perpendicular to the neutral axis of bending. This beam theory is only considered in this thesis for simplicity and its suitability to the design issues discussed in the coming chapters. Note that at high frequencies the Euler-Bernoulli beam assumptions are no longer valid and shear deformation and rotational inertia need to be considered (e.g. Timoshenko beam theory).

The sign convention adopted for an element of a beam, δx, vibrating with a transverse displacement $w(x)$ is shown in Figure 2.2 together with the shear forces and bending moments acting on the element.

The shear force Q and bending moment M shown in Figure 2.2 are given by [37]

$$Q = -EI\frac{\partial^3 w}{\partial x^3}, \quad M = EI\frac{\partial^2 w}{\partial x^2}, \tag{2.3a, b}$$

where EI is the flexural rigidity of the beam.

Consideration of the dynamic equilibrium of the beam element results in the Euler Bernoulli flexural wave equation [37]

$$EI\frac{\partial^4 w}{\partial x^4} + \rho A\frac{\partial^2 w}{\partial t^2} = 0, \tag{2.4}$$

where A is the cross-sectional area of the beam.

For simple harmonic motion $w(x,t) = W(x)e^{i\omega t}$, and the equation of motion becomes

$$EI\frac{d^4 W}{dx^4} - \rho A\omega^2 W = 0. \tag{2.5}$$

The solution to this fourth order equation is

$$W(x) = a^+ e^{-ikx} + a^- e^{ikx} + a_N^+ e^{-kx} + a_N^- e^{kx}, \tag{2.6}$$

where

$$k = \sqrt{\omega}\sqrt[4]{\frac{\rho A}{EI}}, \tag{2.7}$$

is the flexural wavenumber. Hence, the displacement of the beam structural element is considered as the sum of four wave components: two propagating waves – a positive going wave a^+ and a negative going one a^- – and two nearfield or non-propagating waves – a_N^+ in the positive direction and a_N^- in the negative direction. The nearfield waves are also called evanescent waves and the presence of these waves is a result of the wave equation being of fourth order and the fact that a beam in flexure supports both bending and shear forces [35]. The amplitudes of these waves decrease exponentially with distance, by a factor of over 500 in one wavelength [38], and can therefore be ignored at large distances. However, in the nearfield of a disturbance source, an attachment such as a TVA or a boundary, these waves are important. It is generally accepted that propagating waves can transmit energy and nearfield waves hold energy, but they cannot transmit it through the structure. However, the energy flow in a solitary evanescent wave is zero, two such waves of opposite directions can produce non-zero flow of energy as discussed in the next section [39, 40].

From equation (2.7) the phase velocity of the flexural wave $c_f = \omega / k = \sqrt{\omega}\sqrt[4]{EI / \rho A}$ is frequency dependent. Hence flexural waves are dispersive. Thus waves at different frequencies propagate at different speeds; these differences in speed cause spreading or dispersion of wave packets [37].

Flexural waves are the easiest to excite in beams, however axial and torsional vibrational motions may also exist. In this project, only the control of flexural waves will be considered for a number or reasons. Firstly, because they are often the most important wave type in many kinds of structure, where they have large lateral displacements and can readily cause the radiation of sound. Secondly, flexural waves are dispersive, and have nearfield components associated with their generation which in turn complicates their behaviour. Lastly, if the detection of flexural waves is understood then the behaviour of other wave types can be deduced by cancelling the nearfield terms in the general expression [35].

2.3 Energy Flow in Flexural Waves

The flow of vibrational energy through a beam structure due to the propagation of flexural waves and the interaction of two nearfields is discussed in this section. The flow of energy along the beam, which is also called the structural intensity, is given in terms of the beam deformation and internal forces by [41]

$$i(x,t) = -Q\frac{\partial w}{\partial t} - M\frac{\partial^2 w}{\partial x \partial t}, \tag{2.8}$$

where $\partial w / \partial t$ and $\partial^2 w / \partial x \partial t$ are the transverse and rotational velocities of the beam respectively. The shear force Q and bending moment M are given in equations (2.3a) and (2.3b) respectively.

Consider a positive-going propagating flexural wave with a complex amplitude a^+, so that

$$w(x,t) = \mathrm{Re}\left\{a^+ e^{i\phi_1} e^{i(\omega t - kx)}\right\} = \left|a^+\right| \cos\left(\omega t - kx + \phi_1\right), \tag{2.9}$$

where ϕ_1 is the argument of the complex amplitude. The structural intensity of the positive propagating wave, from equations (2.3) and (2.8), is

$$i(x,t) = EIk^3\omega\left|a^+\right|^2\left\{\cos^2\left(\omega t - kx + \phi_1\right) + \sin^2\left(\omega t - kx + \phi_1\right)\right\} = EIk^3\omega\left|a^+\right|^2. \tag{2.10}$$

It is clear that the energy flow is proportional to the square of the wave amplitude [38].

Consider an evanescent wave with amplitude a_N^+. Therefore

$$w(x,t) = \mathrm{Re}\left\{a_N^+ e^{i\phi_2} e^{(i\omega t - kx)}\right\} = \left|a_N^+\right| e^{-kx} \cos(\omega t + \phi_2), \tag{2.11}$$

where ϕ_2 is the argument of a_N^+. Subsequently, one can find that the energy flow in a beam due to single evanescent wave, is given by

$$\begin{aligned} i(x,t) &= EIk^3\omega\left|a_N^+\right|^2 \left\{\cos(\omega t + \phi_2)\sin(\omega t + \phi_2) - \cos(\omega t + \phi_2)\sin(\omega t + \phi_2)\right\} \\ &= 0. \end{aligned} \tag{2.12}$$

Hence a single evanescent wave transmits no energy.

Two evanescent waves decaying in opposite directions with amplitudes a_N^+ and a_N^- would give the following displacement:

$$\begin{aligned} w(x,t) &= \mathrm{Re}\left\{a_N^+ e^{i\phi_2} e^{(i\omega t - kx)} + a_N^- e^{i\phi_3} e^{(i\omega t + kx)}\right\} \\ &= \left|a_N^+\right| e^{-kx} \cos(\omega t + \phi_2) + \left|a_N^-\right| e^{kx} \cos(\omega t + \phi_3), \end{aligned} \tag{2.13}$$

where ϕ_2 and ϕ_3 are the arguments of a_N^+ and a_N^-, respectively. Therefore, one can find that two evanescent waves decaying in opposite directions would give rise to the energy flow

$$i(x,t) = 2EIk^3\omega\left|a_N^+\right|\left|a_N^-\right|\sin(\phi_2 - \phi_3). \tag{2.14}$$

This energy flow depends on the amplitudes of the evanescent waves and on the arguments of the complex amplitudes. When the displacements in the two opposite evanescent waves are not in phase, and not in counter-phase, the work done by the stresses in one wave through the displacements in the other wave is not zero, and that leads to a uniform flow of energy along the structure [39].

2.4 Measurement of Wavenumber and Wave Amplitudes

This section discusses methods that can be implemented experimentally to estimate the wavenumber of a beam structure and the wave amplitudes of flexural waves propagating on a beam from measured physical variables.

2.4.1 Measuring wavenumber

From equation (2.7), the flexural wavenumber k is a function of the beam properties and the frequency of excitation. However, k can be estimated experimentally by considering the motion of the beam at three different locations with spacing Δ, in the farfield of any point disturbance (see Figure 2.3). The beam motion at the different locations can be written as sums of positive and negative propagating wave amplitudes as

$$\begin{aligned} w_1 &= a^+ e^{ik\Delta} + a^- e^{-ik\Delta}, \\ w_2 &= a^+ + a^- \qquad\qquad , \\ w_3 &= a^+ e^{-ik\Delta} + a^- e^{ik\Delta}. \end{aligned} \tag{2.15}$$

In the presence of damping, k has a (usually small) negative imaginary part so that the amplitude of a propagating wave component decays gradually in the direction of propagation. In this thesis, it will be assumed that this decay is negligible over distances of the order of the sensor separation.

One can find the following relation by summing equations (2.15a) and (2.15c) and dividing the resultant by equation (2.15b):

$$\cos(k\Delta) = 0.5\left(\frac{w_1}{w_2} + \frac{w_3}{w_2}\right). \tag{2.16}$$

The above relation can be used to estimate k as a function of frequency.

2.4.2 Measuring wave amplitudes

The motion of a beam under flexural vibration can be decomposed into wave components which can then be used to evaluate reflection and transmission coefficients. These are used in the next chapters to indicate the performance of the TVA's in attenuating incident waves. The output of an array of sensors is decomposed into a set of constituent flexural wave amplitudes [35, 42].

Consider two flexural waves propagating on a beam in opposite directions. An array of two sensors is required to measure these two components independently. The sensors are spaced along the beam as indicated in Figure 2.4. It is assumed that the sensors have negligible mass and rotary inertia (i.e. the perturbation induced by the sensors to the dynamics of the vibrating system is insignificant), a condition discussed, for example, by Mace [43]. The general expression for the transverse displacement of the beam is given by

$$w(x) = a^{+}e^{-ikx} + a^{-}e^{ikx}. \tag{2.17}$$

The vector of displacements measured at two sensor locations symmetrically positioned about the origin ($x = 0$), at $x = \Delta$ and $-\Delta$, may be written in terms of the propagating wave amplitudes, a^{+} and a^{-}, as

$$\begin{bmatrix} w_1 \\ w_2 \end{bmatrix} = \begin{bmatrix} e^{ik\Delta} & e^{-ik\Delta} \\ e^{-ik\Delta} & e^{ik\Delta} \end{bmatrix} \begin{bmatrix} a^{+} \\ a^{-} \end{bmatrix}. \tag{2.18}$$

The vector of propagating wave amplitudes may be obtained in this case, by inversion of the 2×2 matrix in equation (2.18), which gives

$$\begin{bmatrix} a^{+} \\ a^{-} \end{bmatrix} = \frac{1}{2i\sin 2\Delta k} \begin{bmatrix} e^{ik\Delta} & -e^{-ik\Delta} \\ -e^{-ik\Delta} & e^{ik\Delta} \end{bmatrix} \begin{bmatrix} w_1(-\Delta) \\ w_2(\Delta) \end{bmatrix}. \tag{2.19}$$

The matrix is singular when the spacing between the sensors 2Δ is zero or an integer number of half-wavelengths. At spacings close to those which result in singularity, ill-conditioning occurs, making calculations prone to large errors. Ill-conditioning refers to instances when typical levels of error, e.g. in sensor spacing or measurement noise, cause unacceptable errors in the calculated wave amplitudes [42].

It is worthy of note that the wave amplitudes are referred to as displacement wave amplitudes. However, all response quantities (velocity, acceleration, etc) vary time harmonically under the passage of a wave. Thus, one could equally define the amplitudes of the wave components in terms of the amplitude of any such response quantity. For example, one may equally refer to velocity waves, which have amplitudes $a_V^+ = i\omega a^+$, or acceleration waves which have amplitudes $a_A^+ = -\omega^2 a^+$. The superposition of these waves then gives the velocity or acceleration of the waveguide respectively.

2.4.3 Experimental measurement of the wavenumber of a beam

The flexural wavenumber of a beam structure is required for estimating the wave amplitudes, which in turn will be used to indicate the performance of a point discontinuity (i.e. TVA) in controlling the transmitted waves. The wave amplitudes are used to find the reflection and transmission coefficients of a TVA as discussed in the next chapter.

The wavenumber k of a thin steel beam $6.4\text{mm} \times 50.6\text{mm} \times 5630\text{mm}$ was determined experimentally using three PCB accelerometers type 352C22 and an HP frequency analyser type 3566A. The beam was suspended at four points along its length and the ends of the beam were embedded in sandboxes. The presence of the sandboxes reduces any resonant effects, so that the spectra of the wave amplitudes incident on the sensors become more uniform. The experimental set-up is shown in Figure 2.5. The accelerometers were equally spaced such that the spacing between each two accelerometers was $\Delta = 0.5\text{m}$. From equation (2.16), there is no restriction on the choice of Δ, however the spacing between the accelerometers has to be identical and the accelerometers should be far enough away from any point discontinuity or boundary so that the amplitudes of nearfield waves are negligible. The accelerometers were calibrated relative to one another and the relative calibration factors were found to be very close to 1 (see Appendix 1).

The beam was excited with band-limited random noise over a frequency range 50 to 1600 Hz using a Ling V201 shaker, and the frequency response functions between the acceleration A_2 at $x=0$ (see Figure 2.5) and the accelerations A_1 and A_3 were measured. The measured frequency response functions A_1/A_2 and A_3/A_2 were implemented in equation (2.16) to estimate $\cos(k\Delta)$ as a function of frequency as shown in Figure 2.6. The wavenumber was found to equal $0.83\sqrt{f}$ using the best fit by eye to the measured $\cos(k\Delta)$. One can find the best fit by taking the cosine of the product of Δ and k that is given by equation (2.7) and comparing it to the measured $\cos(k\Delta)$ as shown in Figure 2.6. The best fit was found by taking the cosine of $k\Delta=0.42\sqrt{f}$.

2.5 Reflection and Transmission of Flexural Waves

A wave propagates unchanged along a uniform member. If incident on a boundary or point discontinuity, then it will give rise to reflected and transmitted waves [32]. This section briefly introduces the reflection and the transmission of waves at a point attachment with a translational impedance.

Suppose a propagating and/or a nearfield wave (a^+ and/or a_N^+) is incident on a discontinuity. It gives rise to reflected (a^-, a_N^-) and transmitted waves (b^+, b_N^+) of both kinds (nearfield and propagating waves) as shown in Figure 2.7. The amplitudes of the reflected and transmitted waves can be found from the reflection and transmission coefficients described by Cremer *et al* [33], thus

$$r=\frac{a^-}{a^+};r_N=\frac{a_N^-}{a^+};t=\frac{b^+}{a^+};t_N=\frac{b_N^+}{a^+}, \tag{2.20}$$

where r and t are the reflection and transmission coefficients respectively. The subscript N refers to reflected (r_N) or transmitted (t_N) nearfield waves. The reflection and transmission coefficients can be found by systematically applying equilibrium and continuity conditions. The case of an incident propagating wave has been considered frequently (e.g. [33]) while [32] considered the general case of incident propagating and nearfield waves.

As an example, consider a propagating wave (a^+) incident upon a point impedance $\overline{Z}$. It will give rise to propagating and evanescent waves as shown in Figure 2.7. The beam displacement is given by

$$w_+ = b^+ e^{-ikx} + b_N^+ e^{-kx}; \; w_- = a^+ e^{-ikx} + a^- e^{ikx} + a_N^- e^{kx}, \tag{2.21}$$

where w_+ and w_- are the displacements of the beam in the regions $x \geq 0$ and $x \leq 0$, respectively. The reflection and transmission coefficients can be found by considering the continuity and equilibrium equations of the system. Continuity of displacement $(w_+(0) = w_-(0))$ gives, from equation (2.21)

$$a^+ + a^- + a_N^+ = b^+ + b_N^+. \tag{2.22}$$

Continuity of rotation ($\partial w_+(0)/\partial x = \partial w_-(0)/\partial x$) gives

$$-ia^+ + ia^- + a_N^- = -ib^+ - b_N^+. \tag{2.23}$$

From the equilibrium of bending moments at cross-sections of the beam at either side of the point impedance $\overline{Z}$, then one can derive the following relation

$$-a^+ - a^- + a_N^- = -b^+ + b_N^+, \tag{2.24}$$

and from the force equilibrium

$$ia^+ - ia^- + a_N^- - ib^+ + b_N^+ = Z(b^+ + b_N^+), \tag{2.25}$$

where $Z = i\overline{Z}\omega / EIk^3$ is the dimensionless impedance. After solving the above equations, the reflection and transmission coefficients are given by

$$r = \frac{iZ}{4 - Z(1+i)}$$

$$t = \frac{4-Z}{4 - Z(1+i)}$$

$$r_N = t_N = \frac{Z}{4 - Z(1+i)}. \tag{2.26a, b, c}$$

For the special cases of a mass m, damper with constant c_t or a spring $\overline{k}_t$ the impedance is $i\omega m$, c_t or $\overline{k}_t / i\omega$ respectively.

If the point impedance is assumed to be infinite, then it is in effect a pinned support and equations (2.26) become

$$r = -\frac{(1+i)}{2}$$

$$t = \frac{(1-i)}{2}$$

$$r_N = t_N = \frac{(i-1)}{2}. \tag{2.27a, b, c}$$

For a uniform beam the transmitted and reflected powers are therefore equal to $\tau_t = |t|^2$ and $\tau_r = |r|^2$ times the power in the incident wave. If there is no energy loss at the discontinuity then $|t|^2 + |r|^2 = 1$.

2.6 Discussion and Conclusions

In this chapter, the theory of waves in beam-like or one dimension structural elements has been discussed.

Three main wave types, i.e. longitudinal, torsional and flexural waves, can be excited in a beam structure. The importance of controlling the flexural waves was highlighted.

The displacement of a beam element is considered as the sum of four wave components: two farfield propagating waves and two nearfield non-propagating waves. The effect of propagating waves in the transmission of energy has been discussed. In addition, evanescent waves may cause energy to flow via the interaction of two nearfields. This feature becomes of practical significance in structures with discontinuities or constraints from which evanescent waves of various directions are generated.

Experimental work in this chapter included the estimation of the flexural wavenumber for a thin beam as a function of frequency.

Reflection and transmission coefficients of a general point discontinuity have been discussed in this chapter. However, these coefficients will be developed in the next chapter for a more complicated discontinuity (i.e. tuned vibration absorber) with the aim of controlling the transmitted propagating waves.

FIGURES FOR CHAPTER 2

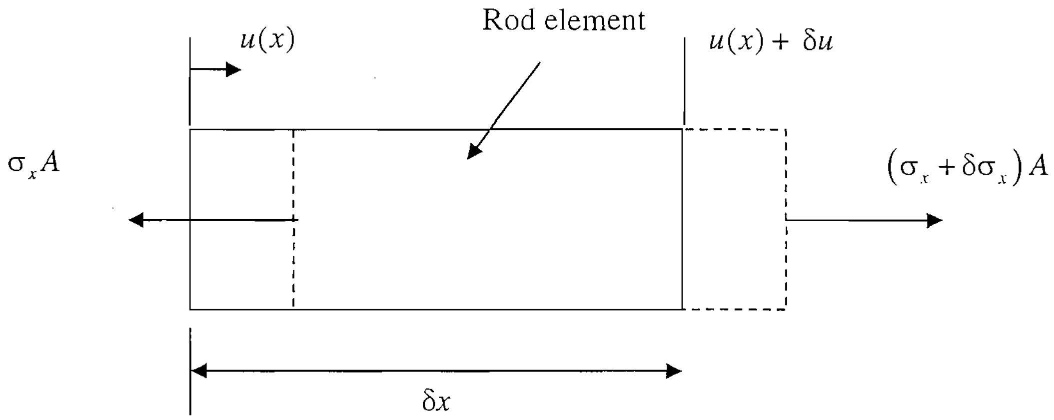

Figure 2.1. Rod element in axial vibration.

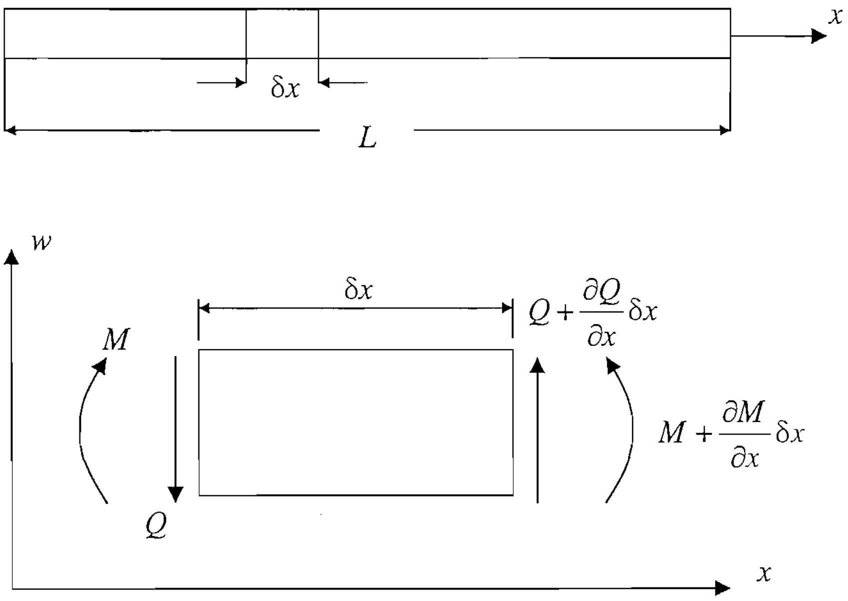

Figure 2.2. Beam element vibrating in flexure.

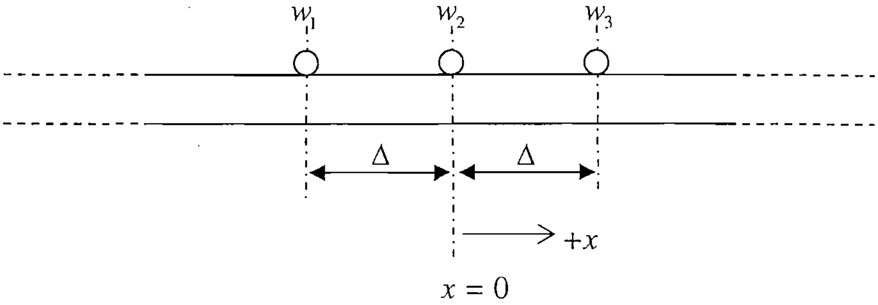

Figure 2.3. Beam with sensors at three equally spaced locations.

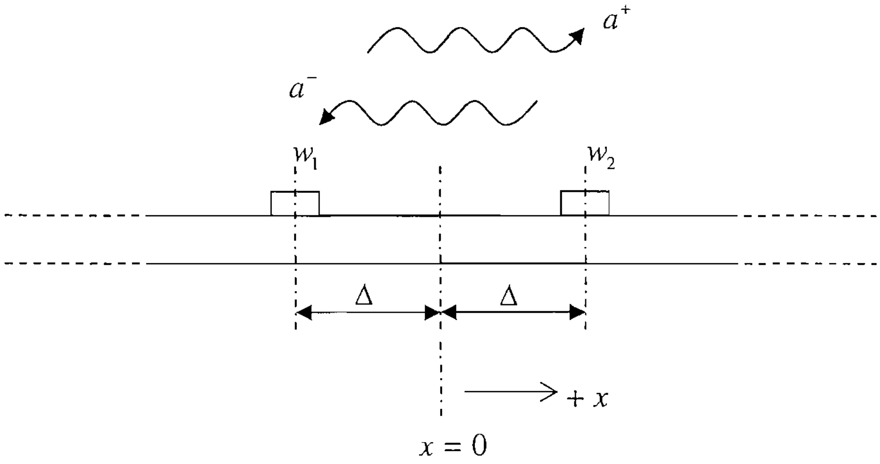

Figure 2.4. A two sensor array used to decompose the flexural wave field into two propagating wave amplitudes.

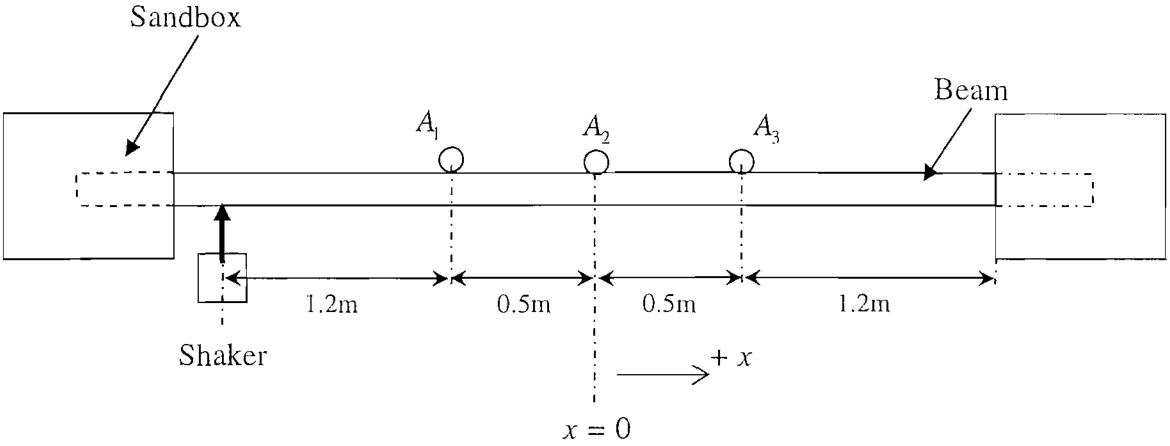

Figure 2.5. Experimental set-up used to measure the wavenumber of a beam

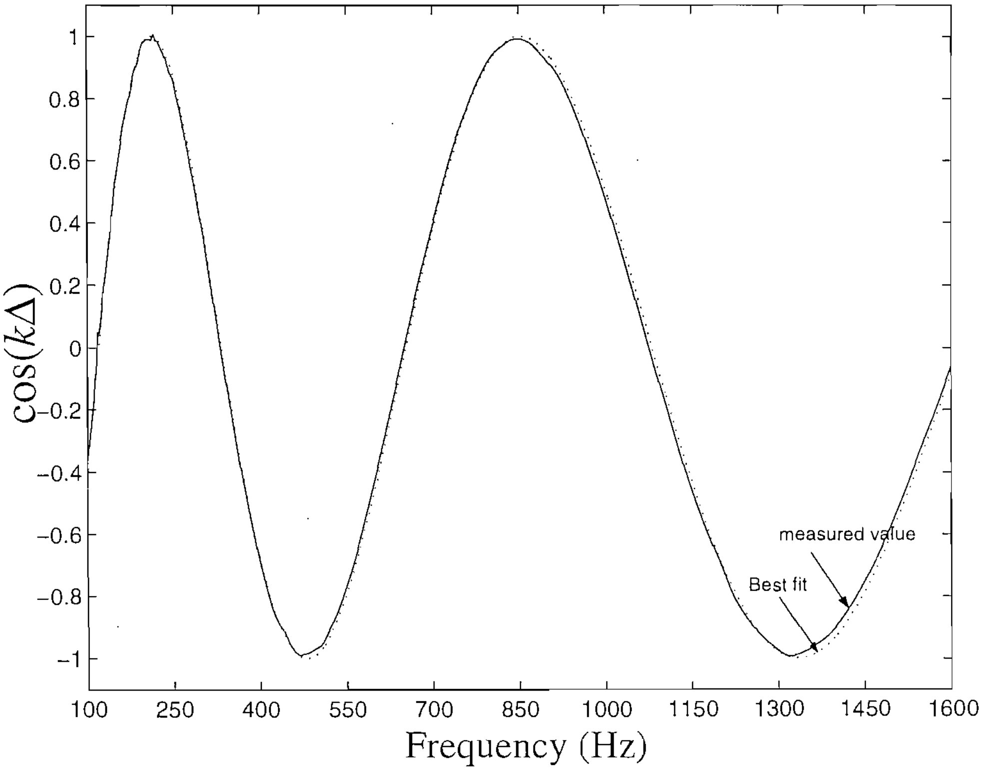

Figure 2.6. Comparison between (———) the measured value of $\cos(k\Delta)$ and (.........) the best fit.

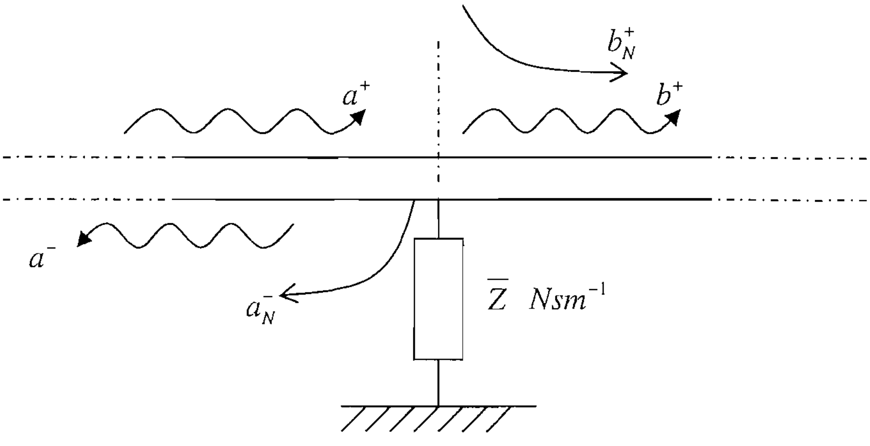

Figure 2.7. Reflected and transmitted waves around point impedance.

CHAPTER 3: PASSIVE CONTROL USING A TUNED VIBRATION ABSORBER

3.1 Introduction

It was seen in Chapter 2 that a wave propagates unchanged along a uniform beam unless it is incident on a discontinuity, where part of it is reflected and part is transmitted. This chapter is concerned with how the transmission of flexural waves in a beam can be controlled using a single tuned vibration absorber (TVA) located in either the nearfield or the farfield of a point disturbance.

Tuned vibration absorbers have been used in many applications since their inception nearly a century ago by Frahm in 1911. These devices can be considered as spring-mass systems which are either tuned to a problematic natural frequency of the host structure or to a troublesome excitation frequency.

The use of a TVA to control a flexural wave on an infinite Euler-Bernoulli beam has been discussed previously. Mead [44] described how tuning the resonance frequency of an undamped absorber to the excitation frequency could pin the beam at the excitation position. Complete suppression of a flexural wave can be achieved by attaching a single undamped TVA and has been discussed by Clark [29] and Brennan [30] who modelled the TVA as a point translational impedance in the farfield of a disturbance.

The purpose of this chapter is to expand on previous work, which assumed the farfield condition, by discussing the behaviour of the TVA located in either the nearfield or the farfield of a harmonic point force. New tuning parameters are determined and expressions derived for the tuned frequency and the bandwidth of attenuation. The cases of optimal energy absorption by the device or minimisation of the transmission of a propagating wave are considered. The presence of an incident evanescent wave, together with the incident propagating wave, affects the optimal characteristics of the

TVA. The net upstream propagating wave is also considered. This is given by the superposition of the wave reflected by the TVA and the upstream wave generated by the point force, and depends on the location of the TVA together with its parameters.

The concept of vibrational power transmission has been considered for the numerical predictions and the experimental measurements in preference to other methods for a number of reasons. The measurement of vibration amplitude at various points around the structure will reveal little detail of the dominant paths of energy transfer. The measurement of vibration amplitude in the presence of standing waves in the structure will result in high levels of vibration being detected while the net power transmitted to adjacent points will be small. Furthermore, it makes little sense for future work to compare the amplitudes of vibration associated with different transmission paths (i.e. linear displacement in flexural motion and angular displacement in torsion).

The chapter is set out as follows. The next section concerns the dynamic behaviour of the TVA and the way in which it affects wave transmission. The reflection and transmission matrices are found. The power transmitted downstream of the TVA is found in terms of four independent parameters: the ratio of the tuned frequency to the TVA frequency, the loss factor of the TVA, the mass of the TVA and the distance between the TVA and the source of disturbance. The net power propagating upstream is also investigated. Non-dimensional parameters are then introduced. The optimum tuning parameters of the TVA are discussed in section 3.3. This includes the tuned frequency, bandwidth of attenuation, location of the TVA and the optimum damping for the maximum power absorption. Section 3.4 is devoted to numerical examples, investigating the performance of the TVA and the optimum tuning parameters of the absorber for both nearfield and farfield cases. Experimental validation of the theoretical predictions is reported in section 3.5. Finally, conclusions are presented.

3.2 Wave Model of a Tuned Vibration Absorber on a Beam

The aim of this section is to investigate the reflection and transmission of waves at a TVA on an infinite beam when the TVA is in either the nearfield or the farfield of a point force disturbance.

3.2.1 Reflection and transmission coefficients

Consider the TVA modelled as a single degree of freedom (SDOF) system and mounted on a beam at $x=0$ and at a distance l from an applied force $F\exp(i\omega t)$ as shown in Figure 3.1. Here m_a, k_a and η are the mass, stiffness and the loss factor of the TVA respectively. The force generates waves, which are incident on the TVA and are partly reflected and partly transmitted. The ratios of the reflected and transmitted wave amplitudes to those of the incident waves depend on the characteristics of the TVA. The wave components shown in Figure 3.1 represent positive- and negative-going propagating waves generated by the point force (a^+, a^-), positive- and negative-going propagating waves at a distance l from the point force (b^+, b^-) and the transmitted propagating wave (c^+). The amplitudes a, b and c are complex; the subscript N refers to evanescent waves. The net upstream propagating wave ($a^- + b^- e^{-ikl}$) is the superposition of the wave reflected from the TVA and the upstream wave generated by the point force.

Suppressing the $e^{i\omega t}$ time dependence for clarity, the beam displacement is given by

$$w_+ = c^+ e^{-ikx} + c_N^+ e^{-kx}; \quad w_- = b^+ e^{-ikx} + b_N^+ e^{-kx} + b^- e^{ikx} + b_N^- e^{kx}, \tag{3.1a, b}$$

where w_+ and w_- are the displacements of the beam in the regions $x \geq 0$ and $-l \leq x \leq 0$ respectively. Here $k = \sqrt[4]{\rho A / EI}\sqrt{\omega}$ is the flexural wavenumber of the beam and ρ, A and EI are the density, cross-sectional area and flexural rigidity of the beam respectively.

The force generates waves of amplitudes [33]

$$\begin{Bmatrix} a^+ \\ a_N^+ \end{Bmatrix} = \begin{Bmatrix} a^- \\ a_N^- \end{Bmatrix} = \frac{-F}{4EIk^3}\begin{Bmatrix} i \\ 1 \end{Bmatrix}, \tag{3.2}$$

the waves incident on the TVA are

$$\begin{Bmatrix} b^+ \\ b_N^+ \end{Bmatrix} = \begin{bmatrix} e^{-ikl} & 0 \\ 0 & e^{-kl} \end{bmatrix} \begin{Bmatrix} a^+ \\ a_N^+ \end{Bmatrix}, \tag{3.3}$$

while the amplitudes of the reflected and transmitted waves are given by

$$\begin{Bmatrix} b^- \\ b_N^- \end{Bmatrix} = \mathbf{r} \begin{Bmatrix} b^+ \\ b_N^+ \end{Bmatrix}; \quad \begin{Bmatrix} c^+ \\ c_N^+ \end{Bmatrix} = \mathbf{t} \begin{Bmatrix} b^+ \\ b_N^+ \end{Bmatrix}. \tag{3.4a, b}$$

Here $\mathbf{r}$ and $\mathbf{t}$ are the reflection and transmission matrices for the TVA.

The reflection and transmission matrices can be found by considering the continuity and equilibrium conditions. Continuity of displacement ($w_+(0) = w_-(0)$) gives, from equations (3.1a) and (3.1b)

$$c^+ + c_N^+ = b^+ + b_N^+ + b^- + b_N^-. \tag{3.5}$$

Continuity of rotation ($\partial w_+(0)/\partial x = \partial w_-(0)/\partial x$) gives

$$-ic^+ - c_N^+ = -ib^+ - b_N^+ + ib^- + b_N^-. \tag{3.6}$$

From equilibrium of shear forces

$$ic^+ - c_N^+ - ib^+ + b_N^+ + ib^- - b_N^- = \frac{k_a}{EIk^3}(1+i\eta)(y - w(0)). \tag{3.7}$$

The term on the right is the force on the beam from the absorber, whose mass has a displacement y. Equilibrium of bending moments gives

$$-c^{+}+c_{N}^{+}=-b^{+}+b_{N}^{+}-b^{-}+b_{N}^{-}. \tag{3.8}$$

The equation of motion of the absorber's mass is given by

$$k_a\left(1+i\eta\right)\left(y-w\left(0\right)\right)=m_a\omega^2 y. \tag{3.9}$$

Finally, the displacement of the absorber's mass is given by

$$y=\left(\frac{k_a\left(1+i\eta\right)}{k_a\left(1+i\eta\right)-m_a\omega^2}\right)w\left(0\right). \tag{3.10}$$

Equations (3.1), (3.5-3.8) and (3.10) can be solved for the reflection and transmission matrices $\mathbf{r}$ and $\mathbf{t}$, which are

$$\mathbf{r}=\beta\begin{bmatrix} i & i \\ 1 & 1 \end{bmatrix};\ \mathbf{t}=\mathbf{I}+\mathbf{r}, \tag{3.11a, b}$$

where $\mathbf{I}$ is the identity matrix and

$$\beta=\frac{\gamma\Omega^{1/2}(1+i\eta)}{\Omega^2-(1+i\eta)(1+\gamma\Omega^{1/2}(1+i))}. \tag{3.12}$$

The dimensionless parameters

$$\gamma=\frac{\pi m_a}{2\rho A\lambda_a};\ \Omega=\frac{\omega}{\omega_a}, \tag{3.13a, b}$$

represent, respectively, the mass ratio γ at the absorber frequency $\omega_a=\sqrt{k_a/m_a}$, i.e. the ratio of the mass of the absorber to the mass in a length $2\lambda_a/\pi$ of the beam (where λ_a is the wavelength at ω_a) and the frequency ratio Ω, which is the ratio of the excitation frequency ω to the absorber frequency ω_a. The variable kl that appears in equation (3.3) can now be re-written in terms of the non-dimensional parameters as

$$kl = 2\pi\sqrt{\Omega}\left(\frac{l}{\lambda_a}\right). \tag{3.14}$$

The wave amplitudes can thus be found by solving equations (3.2-3.4) and (3.11). In the following subsections attention is focused on the transmitted propagating waves c^+ and the net reflected propagating wave $a^- + b^- e^{-ikl}$.

3.2.2 Transmitted power

The transmitted propagating wave c , which carries energy to the farfield downstream of the TVA, has components arising from both the propagating and nearfield incident waves b and b_N^+. It is given by

$$c^+ = \frac{-iFe^{-ikl}}{4EIk^3}\left[\frac{\Omega^2 - (1+i\eta)\left(1+\gamma\Omega^{1/2}\left(1-e^{-kl(1-i)}\right)\right)}{\Omega^2 - (1+i\eta)\left(1+\gamma\Omega^{1/2}(1+i)\right)}\right]. \tag{3.15}$$

It can be seen that c^+ depends on the location of the TVA with respect to the disturbance through the terms involving kl.

The transmission ratio τ_t of the absorber is now defined as the ratio of the power transmitted to that which would be transmitted if the absorber were absent, i.e. $\tau_t = \left|c^+ / a^+\right|^2$ and is given by

$$\tau_t = \left|\frac{\Omega^2 - (1+i\eta)\left(1+\gamma\Omega^{1/2}\left(1-e^{-kl(1-i)}\right)\right)}{\Omega^2 - (1+i\eta)\left(1+\gamma\Omega^{1/2}(1+i)\right)}\right|^2. \tag{3.16}$$

Therefore, the transmitted power also depends on the distance l.

If the TVA is attached at the source of disturbance, then $l = 0$ and the transmission ratio becomes

$$\tau_t = \left| \frac{\Omega^2 - (1 + i\eta)}{\Omega^2 - (1 + i\eta)\left(1 + \gamma\Omega^{1/2}(1 + i)\right)} \right|^2 . \tag{3.17}$$

If the TVA is attached in the farfield of the disturbance, then kl is large and the transmitted power becomes

$$\tau_t = \left| \frac{\Omega^2 - (1 + i\eta)\left(1 + \gamma\Omega^{1/2}\right)}{\Omega^2 - (1 + i\eta)\left(1 + \gamma\Omega^{1/2}(1 + i)\right)} \right|^2 . \tag{3.18}$$

The transmission ratio depends on the absorber parameters and the frequency ratio in a somewhat complicated manner.

3.2.3 Upstream power

The net wave propagating upstream of the point force $(a^- + b^- e^{-ikl})$ is given by

$$(a^- + b^- e^{-ikl}) = \frac{-iF}{4EIk^3}\left[1 + ie^{-2ikl}\left[\frac{\gamma\Omega^{1/2}(1 + i\eta)\left(1 - ie^{-kl(1-i)}\right)}{\Omega^2 - (1 + i\eta)\left(1 + \gamma\Omega^{1/2}(1 + i)\right)} \right]\right] . \tag{3.19}$$

The reflection ratio τ_r is defined as the ratio of the power reflected upstream to that which would propagate upstream if the absorber were absent, i.e. $\tau_r = \left|(a^- + b^- e^{-ikl}) / a^-\right|^2$ and is given by

$$\tau_r = \left| 1 + ie^{-2ikl}\left[\frac{\gamma\Omega^{1/2}(1 + i\eta)\left(1 - ie^{-kl(1-i)}\right)}{\Omega^2 - (1 + i\eta)\left(1 + \gamma\Omega^{1/2}(1 + i)\right)} \right] \right|^2 . \tag{3.20}$$

If the TVA is attached at the source of disturbance then the reflection ratio is equal to the transmission ratio given by equation (3.17), while if the TVA is attached in the farfield of the disturbance, then τ_r reduces to

$$\tau_r = \left| 1 + ie^{-2ikl} \left[\frac{\gamma\Omega^{1/2}(1+i\eta)}{\Omega^2 - (1+i\eta)\left(1+\gamma\Omega^{1/2}(1+i)\right)} \right] \right|^2 . \tag{3.21}$$

3.3 Optimum Tuning of the TVA

In this section some comments are made concerning the optimum tuning parameters of the TVA. It is possible to either minimise the power transmitted both downstream and upstream or to maximise the power absorbed by the TVA. For a time harmonic disturbance, in the first case ideally $\eta = 0$ while in the second case there is an optimum value of structural damping in the TVA. If the incident evanescent wave is significant, then the distance l between the force and the position of the TVA also affects the optimum tuning parameters. In general, numerical solutions are required to determine the optimum tuning parameters. However, for the case of an undamped TVA, analytical expressions exist for various special cases and some are given in this section, together with certain approximations valid for small values of the absorber parameters.

3.3.1 Tuned frequency and bandwidth of attenuation

If the TVA is undamped $\eta = 0$ then the transmission and reflection ratios become

$$\tau_t = \left| \frac{\Omega^2 - \left(1+\gamma\Omega^{1/2}\left(1-e^{-kl(1-i)}\right)\right)}{\Omega^2 - \left(1+\gamma\Omega^{1/2}(1+i)\right)} \right|^2 ;$$

$$\tau_r = \left| 1 + ie^{-2ikl} \left[\frac{\gamma\Omega^{1/2}\left(1-ie^{-kl(1-i)}\right)}{\Omega^2 - \left(1+\gamma\Omega^{1/2}(1+i)\right)} \right] \right|^2 . \tag{3.22a, b}$$

The tuned frequency Ω_t is now defined to be the frequency ratio at which the transmitted power is minimum. If the TVA is attached to the source of disturbance (i.e. $kl = 0$), then $\Omega_t = 1$, so that minimum transmission occurs at the absorber frequency, where the impedance of the absorber is infinite. At this frequency the transmission and reflection ratios are both zero.

If the TVA is located in the farfield (i.e. $kl \to \infty$), then the tuned frequency ratio satisfies

$$\Omega_t^2 - \gamma\Omega_t^{1/2} - 1 = 0. \tag{3.23}$$

Increasing the mass ratio increases Ω_t. At this frequency the transmitted power is zero. There is no analytical solution for Ω_t, but approximate solutions can be found for small and large γ, namely

$$\begin{aligned} &\Omega_t \approx 1 + \gamma/2; \qquad && \gamma << 1 \\ &\Omega_t \approx \gamma^{2/3}; && \gamma >> 1. \end{aligned} \tag{3.24a, b}$$

This case is discussed in detail by Brennan [30].

The tuned frequency ratio $\Omega_t \geq 1$ depends on the mass ratio as well as the location of the absorber. If $kl \ll 1$ for an undamped absorber, then the tuned frequency can be approximated as the solution to

$$\mathrm{Re}\left\{\Omega_t^2 - \gamma\Omega_t^{1/2}\left(1 - e^{-kl(1-i)}\right) - 1\right\} = 0. \tag{3.25}$$

This can be simplified by using a Taylor's series ($e^{-kl} \approx 1 - kl + \ldots$) to give

$$\Omega_t \approx 1 + \frac{\gamma kl}{2}. \tag{3.26}$$

The small and large kl asymptotes of equations (3.24a) and (3.26) intersect when $kl = 1$.

The transmission ratio varies with Ω and its maximum value is greater than 1 and occurs at a frequency ratio $\Omega_m > \Omega_t$ which also depends on the TVA location. If the TVA is attached at the disturbance location then

$$\Omega_m^2 - 2\gamma\Omega_m^{1/2} - 1 = 0, \tag{3.27}$$

and the maximum power transmitted is $\tau_{t,\max} = 2$. For small γ, $\Omega_m \approx 1 + \gamma$. Hence increasing the mass ratio increases the frequency ratio Ω_m at which the maximum transmission occurs. The maximum transmission arises due to matching of the impedance of the undamped absorber to the reactive part of the impedance of the beam at this frequency. The maximum power transmitted decreases as kl increases, reaching 1 as $kl \to \infty$.

The TVA is effective over a narrow bandwidth $\Delta\Omega$ as discussed by Brennan [30]. The bandwidth of attenuation here is defined as the width of the stop-band in which less than half the incident power is transmitted. The lower and the upper half-power points, for an undamped TVA located in the farfield, can be found by equating the transmission ratio in equation (3.18) when to 0.5. The lower half-power point is $\Omega_1 = 1$; this is independent of γ. At this frequency, the beam is effectively pinned and $\tau_t = 0.5$. The upper half-power point Ω_2 depends on $\eta = 0$. For $kl \to \infty$ and small γ, this is given approximately by

$$\Omega_2 \approx 1 + \gamma. \tag{3.28}$$

Hence the bandwidth of attenuation $\Delta\Omega \approx \gamma$.

3.3.2 Optimum damping for power absorption

The maximum power that can be absorbed by the TVA cannot exceed half the incident power, since the beam is only restrained translationally, and the TVA cannot affect energy flow due to rotational (bending moment) components [45].

An approximation for the optimum mass ratio, which achieves the maximum power absorption, can be attained by taking the impedance of the TVA and that of the beam into consideration. The translational impedance of an infinite beam excited by a point force (i.e. the ratio of applied force to the velocity it produces) is given by Mead [44]

$$Z_{beam} = \frac{2EIk^3}{\omega}(1+i). \tag{3.29}$$

The impedance of the TVA that ensures that it absorbs the maximum power Z_{opt} is the complex conjugate of the impedance of the beam as stated in the "maximum-power-transfer theorem" [46] between two devices in a network, and is given by

$$Z_{opt} = \frac{2EIk^3}{\omega}(1-i) \tag{3.30}$$

The impedance of a TVA, Z_{TVA}, given by Brennan [30, 47] is

$$Z_{TVA} = \frac{m_a\omega(i-\eta)}{1-\Omega^2+i\eta}. \tag{3.31}$$

Equation (3.31) can be reformulated using the parameters given in equations (3.13a) and (3.13b) and written in non-dimensional form as

$$\frac{i\omega Z_{TVA}}{4EIk^3} = \frac{-\gamma\Omega^{1/2}(1+i\eta)}{1-\Omega^2+i\eta}. \tag{3.32}$$

Now consider the behaviour of the absorber at the tuned frequency when $\eta << 1$ (i.e. $\Omega_t^2 \approx 1 + \gamma\Omega_t^{1/2}$)

$$\frac{i\omega Z_{TVA}}{4EIk^3} = \frac{-\gamma\Omega_t^{1/2}(1+i\eta)}{-\gamma\Omega_t^{1/2} + i\eta}. \tag{3.33}$$

Assuming $\gamma << 1$ and $\Omega_t^{1/2} \approx 1$, which are often the case in practice, then

$$\frac{i\omega Z_{TVA}}{4EIk^3} = \frac{1+i(\eta/\gamma)}{1+(\eta/\gamma)^2}. \tag{3.34}$$

The value of the TVA impedance which is optimal can be found by substituting equation (3.30) into equation (3.34) resulting in the relationship $\eta/\gamma = 1$. This means that for maximum power absorption by the TVA the loss factor should be approximately equal to the mass ratio.

3.3.3 Optimum location of the absorber

The net wave propagating upstream for a TVA attached in the farfield can be written as

$$\left(a^- + b^- e^{-ikl}\right) = a^- \left(1 + |r_{11}| e^{-i(2kl+\phi)}\right), \tag{3.35}$$

where $|r_{11}|$ and ϕ are the magnitude and phase of the (1,1) element of the reflection matrix. If the absorber is undamped and optimally tuned, then the transmission coefficient $t_{11} = 0$ and the reflection coefficient $r_{11} = -1$. Therefore equation (3.35) becomes

$$\left(a^- + b^- e^{-ikl}\right) = a^- \left(1 - e^{-i2kl}\right). \tag{3.36}$$

If the total phase shift $2kl = (2n-1)\pi$, where n is any integer, then the amplitude of the upstream wave in the farfield is $2a^-$: the reflected wave interferes constructively with the upstream wave injected by the disturbance. On the other hand, if $2kl = 2n\pi$, then the amplitude of the upstream-going wave is zero: the two wave components interfere destructively. Thus the location l of the undamped absorber can be chosen in order to obtain zero transmission upstream if the absorber is located in the farfield. Therefore, the transmitted and reflected power can be completely suppressed at a single frequency using a single undamped TVA located in the correct position in the farfield. If the TVA is not in the farfield then the phase of r_{11} is somewhat different from $-\pi$, while its magnitude is somewhat less than 1, so that total cancellation of the upstream going wave does not occur.

3.4 Numerical Examples

The dependence of the power transmitted and absorbed on the TVA parameters is illustrated numerically in this section.

3.4.1 Effect of TVA location

Figure 3.2 shows the transmission ratio τ_t as a function of the frequency ratio Ω for two different mass ratios γ and various locations of the TVA, l/λ_a, where $\lambda_a = 2\pi/k$ is the flexural wavelength at the absorber frequency. The TVA is assumed to be undamped. Generally, in each case the transmission has a minimum at a certain frequency Ω_t. However, in all cases $\Omega_t = 1$ when $l = 0$ and the transmission ratio asymptotes to 1 as $\Omega \to \infty$. It can be seen that $\tau_t > 1$ for some $\Omega > \Omega_t$ and increasing l/λ_a reduces the maximum transmission ratio. Also, increasing l/λ_a increases the tuned frequency. When the nearfield wave is significant, the transmission ratio of the undamped absorber is no longer zero at Ω_t. Moreover, increasing the mass ratio increases Ω_t.

3.4.2 TVA located in the farfield

If the TVA is positioned in the farfield of the point disturbance then evanescent waves incident on the TVA are negligibly small. The effect of the mass ratio on the power transmitted for an undamped TVA is shown in Figure 3.3a. Increasing the mass ratio increases the tuned frequency ratio Ω_t.

Figure 3.3b illustrates the effect of damping on the performance of the TVA. Although damping reduces the attenuation of the power transmitted at Ω_t, it also increases the proportion of the incident power absorbed by the TVA as shown in Figure 3.4. Increasing the damping gradually increases the maximum power absorbed P_a (the power absorbed per input power) for a constant mass ratio until the damping reaches a particular limit. This is approximately when $\eta \approx \gamma$, as discussed in the previous section, when half of the incident power is absorbed, while the other half is equally transmitted and reflected. When $\eta > \gamma$, then the maximum power absorbed decreases as shown in Figure 3.4a, while the frequency Ω_b at which the maximum absorption occurs increases with η. The effect of γ on the proportion of incident power absorbed by the TVA is shown in Figure 3.4b. Increasing γ increases P_a as well as Ω_b for a fixed level of damping as long as $\gamma < \eta$. This latter effect is insignificant if the TVA is lightly damped.

3.4.3 Optimum tuning

It was seen that the location of the TVA affects the power reflected upstream of the point force. Figure 3.5a shows the effect of l/λ_a on the reflection ratio for different mass ratios. Changing the mass ratio changes the value of τ_r at certain locations of the TVA. This effect becomes insignificant as $\eta \to 0$ as shown in Figure 3.5b.

The optimum location of the absorber at which the minimum power flows up- and down-stream can be chosen by taking both τ_t and τ_r into consideration as shown in Figure 3.6. The optimum location of the TVA is at one of the normalised distances

(l/λ_a) that give the maximum attenuation of τ_r (approximately at multiples of $0.5\lambda_a$). The minimum values of τ_r and the value of τ_t for a farfield location depend on η, and tend to zero as $\eta \rightarrow 0$.

Figure 3.7 shows the tuned frequency ratio Ω_t as a function of l/λ_a for various γ. Generally, Ω_t increases with l/λ_a and asymptotes to the values given by equations (3.24a) and (3.26) when the TVA is in the farfield and nearfield respectively. These asymptotes are shown in Figure 3.7 for $\gamma = 0.05$. Increasing the mass ratio increases Ω_t for a given location of the TVA. The minimum power transmitted generally occurs at higher tuned frequency ratios if the TVA is located further away from the point disturbance. This is not the case in the farfield, when the position of the TVA no longer affects Ω_t for a given γ.

The optimum tuning parameters of an absorber attached in the farfield can be found from equations (3.18) and (3.21). Figure 3.8 shows the relation between Ω_t and the damping of the absorber for various γ. Increasing η and/or γ increases Ω_t. However, when $\eta << 1$ then damping slightly affects Ω_t. A trade off should combine the beneficial effects of both η and γ for the best exploitation of the absorber, where increasing η would reduce the attenuation of the transmitted power.

The effects of the mass ratio and damping on Ω_p are similar to their effects on Ω_t as shown in Figure 3.9. It is also worthy of note that Ω_p is greater than Ω_t.

The optimum parameters of the TVA at which the maximum power is absorbed are found numerically and are illustrated in Figure 3.10. Designing a TVA with a higher value of structural damping than the optimum value indicated in Figure 3.10 for a given mass ratio will reduce the maximum power absorbed by the TVA.

The variation of the frequency bandwidth $\Delta\Omega$ as function of l/λ_a is shown in Figure 3.11. In general, the maximum bandwidth is achieved in the nearfield. Increasing

l/λ_a decreases $\Delta\Omega$ for a given η and/or γ. However, this effect becomes insignificant in the farfield. The effect of the mass ratio on the frequency bandwidth is shown in Figure 3.11a. It is clear that increasing γ increases $\Delta\Omega$ and $\Delta\Omega \approx \gamma$ when the nearfield waves are insignificant. Also increasing η increases $\Delta\Omega$ as shown in Figure 3.11b.

3.5 Experimental Validation

A design for a passive vibration absorber is introduced in this section. The absorber is characterised experimentally then attached to a beam to control the power transmission. The experimental results are compared with the theoretical and numerical predictions presented in the previous sections.

3.5.1 The passive beam-like absorber

A TVA was implemented using a beam with masses attached at its ends as shown in Figure 3.12a. The centre of the beam is attached to the host structure. The stiffness of the TVA is provided by the beam vibrating in bending while the mass comes mostly from the tip masses and partly from the mass of the beam. The first mode of the TVA occurs at the absorber frequency ω_a, where the absorber is in effect clamped at the centre [48].

The absorber can be modelled as two symmetric cantilevers with masses at the end (see Figure 3.12b for a single cantilever). The natural frequency of the cantilever (the absorber frequency ω_a) can be derived using Dunkerley's equation [48, 49] such that

$$\frac{1}{\omega_a^2} \approx \frac{1}{\omega_1^2} + \frac{1}{\omega_2^2}, \tag{3.37}$$

where

$$\omega_1^2 = \frac{3EI}{M_e L^3}, \tag{3.38}$$

is the natural frequency of the massless cantilever with a tip mass M_e, EI is the flexural rigidity and L is the length of the cantilever, while

$$\omega_2^2 = \frac{12.4EI}{M_b L^3}, \tag{3.39}$$

is the natural frequency of a cantilever of mass M_b without the tip mass. Thus

$$\omega_a^2 \approx \frac{3EI}{L^3\left(0.243M_b + M_e\right)}, \tag{3.40}$$

The characteristics of the absorber can be predicted by modelling the absorber as a simple two degree of freedom system (see Figure 3.12c). Thus, the impedance of the model introduced by Hixon [50] can be implemented. This is given by

$$Z_{TVA} = \frac{m_a \omega k_a \left(1 + i\eta\right)}{i m_a \omega^2 - k_a \left(i - \eta\right)} + i m_b \omega, \tag{3.41}$$

where m_a is the effective mass of the absorber while m_b is the mass of the absorber that is effectively attached to the host structure.

3.5.2 Characterisation of the absorber

A beam-like absorber was made of a steel beam ($1.7\text{mm} \times 20.5\text{mm} \times 80.4\text{mm}$) with blocks of brass ($10.3\text{mm} \times 10.2\text{mm} \times 20.5\text{mm}$) attached at each end as shown in Figure 3.13. The theoretical prediction of the absorber frequency is $\hat{f}_a = 314.2$ Hz. This was obtained using equation (3.40) with the dimensions shown in Figure 3.13 and the data provided in Table 3.1.

The absorber was attached to a PCB impedance head type 288D01 fitted to a Ling V201 shaker which excited the absorber with band-limited random noise over a frequency range of 0 to 800 Hz. The measured impedance of the absorber is plotted in Figure 3.14. The absorber frequency was obtained experimentally as $f_a = 343\,\text{Hz}$. In addition, the resonance frequency f_r (i.e. the frequency at which the impedance is minimum) was also obtained and equals $603\,\text{Hz}$. The loss factor of the absorber was estimated to be $\eta = 0.01$ using the circle fit method [51].

The effective masses m_a and m_b of the absorber were estimated using knowledge of the experimental absorber frequency f_a and resonance f_r. Also $\omega_a = \sqrt{k_a / m_a}$ and $\omega_r = \sqrt{k_a (m_a + m_b) / m_a m_b}$ which are given in [50]. The total mass of the absorber ($m_a + m_b = 67.6\,\text{g}$) was found experimentally from the point accelerance at low frequencies. Therefore, $m_a = 45.7\,\text{g}$ and $m_b = 21.9\,\text{g}$. The stiffness of the model was thus found to be $k_a = 212.6\,\text{kN/m}$. The absorber parameters found experimentally were used in equation (3.41) and the comparison between the theoretical and the measured point impedance of the absorber is shown in Figure 3.14. It is seen that the numerical prediction of the absorber's point impedance, from equation (3.41), agrees well with the experimental measurement.

3.5.3 Implementation of the TVA for vibration control on a beam

The absorber was attached at its centre to a $6.4\text{mm} \times 50.6\text{mm} \times 5630\text{mm}$ straight steel beam suspended at four points along its length. The ends of the beam were embedded in sand boxes to reduce reflections. The measured wavenumber of the beam was such that $k = 0.83\sqrt{f}$ as discussed in Chapter 2. The ratio of the mass of the beam in a length $2\lambda_a / \pi$ to m_b is about 30:1, and therefore m_b is negligible. The mass ratio of the TVA was predicted to be $\gamma = 0.07$ using equation (3.12a).

The beam was excited by a Ling V201 shaker with band limited random noise over a frequency range of 50 – 800 Hz. The propagating wave amplitudes were estimated using the frequency domain wave decomposition approach described in the previous chapter. This requires measuring the acceleration along the beam at four different points. Four PCB type 352C22 accelerometers were employed to measure the required accelerations. Other equipment included an 8 channel HP 3566A spectrum analyser, Ariston 910 power amplifier and a PCB 441A42 signal conditioner.

The accelerometers were divided into two pairs as shown in Figure 3.15. The first pair (A_1 and A_2) was used to estimate the amplitude of the upstream propagating wave, while the second pair (A_3 and A_4) was used to estimate the amplitude of the downstream propagating wave. This allows measurement of wave amplitudes with or without the absorber attached to the beam, and hence estimation of the transmission and reflection ratios.

The distance between the two accelerometers in each array was chosen to be 40mm (less than half the shortest wavelength as discussed in Chapter 2). In order to avoid the effects of nearfield waves above 150 Hz, the distance between each of the sand boxes, the absorber, the source of disturbance and the accelerometer arrays was chosen to be greater than a wavelength at 150 Hz (0.62m). Nevertheless, the distance between the point disturbance and the TVA took one of five different values ($l/\lambda_a = 0$, 0.34, 0.49, 0.73 and 0.98, where $\lambda_a = 0.41$ m) to examine the effects of the location of the TVA.

Figure 3.16 shows the numerical predictions of equation (3.16) and the experimental measurements when the TVA is attached to the point where the disturbance acts ($l/\lambda_a = 0$). For this case τ_r and τ_t should be equal. Control at the absorber frequency of 343 Hz can be clearly seen. The measured powers transmitted downstream and upstream are nearly equal. Moreover, the tuned frequency is seen to be the same as the absorber frequency as predicted. The maximum attenuation achieved was approximately 34dB in the transmitted power as shown in Figure 3.16a and 25dB in the upstream power as shown in Figure 3.16b. These values are very sensitive to the level of damping in the TVA.

The effects of the location of the TVA were investigated experimentally by choosing four different locations of the TVA. Results are shown in Figure 3.17. Agreement is generally good. A clear notch in τ_t is seen around the tuned frequency, while τ_r

depends strongly on the location of the TVA. In Figure 3.17a $l/\lambda_a = 0.34$, so that the TVA is well within the nearfield of the disturbance. However, in Figure 3.17b $l/\lambda_a = 0.49$, so that there are still significant nearfield effects. Now there is also a clear notch in τ_r, due to the interference of the two wave components a^- and $b^- e^{-ikl}$. Locating the TVA at $l/\lambda_a = 0.73$ has increased the reflection ratio by approximately 5dB as shown in Figure 3.17c. The tuned frequency here has slightly increased to 356 Hz. Figure 3.17d shows the case where choosing an optimum location for the TVA achieves attenuation in both τ_t and τ_r. The tuned frequency here was found to be approximately 356Hz as predicted (the tuned frequency is independent of position in the farfield for a given mass ratio).

The disagreement at low and high frequencies is due to measurement errors and sensor miscalibration. Moreover, it is difficult to estimate the structural damping accurately which affects the response around the tuned frequency.

3.6 Discussion and Conclusions

This chapter has presented theoretical and experimental investigations of the behaviour and the optimum tuning parameters of a TVA which suppresses flexural waves in thin beams. The location of the TVA with respect to a point disturbance has been taken into account.

The reflection and transmission ratios for the TVA were derived and depend on four independent tuning parameters: the absorber frequency ω_a, the mass ratio γ, the damping η, and the non-dimensional distance l/λ_a between the TVA and the disturbance. Emphasis was placed on finding the tuning parameters, which ensure the minimum power transmitted and reflected or the maximum power absorbed.

Analytical expressions for the transmitted and reflected powers were found to have components arising from both the propagating and evanescent incident waves. The location of the TVA only affects the tuned frequency if the incident evanescent waves are significant. In general, increasing the distance between the TVA and the source of disturbance would achieve the maximum attenuation in the transmitted power at a higher frequency ratio regardless of the power reflected upstream. Attenuation in the power flow in both directions can be achieved at the tuned frequency if the absorber is attached at certain distances from the point disturbance. These locations are approximately multiples of half the wavelength at the absorber frequency.

Numerical investigations have shown how increasing the mass ratio increases the tuned frequency, i.e. the frequency at which the maximum power is absorbed, and the bandwidth of attenuation. Conversely, damping was found to reduce the attenuation of the transmitted power but it increases the tuned frequency.

Damping was also found to reduce the maximum transmission ratio which occurs when the TVA is attached in the nearfield of the disturbance. It was shown that the frequency at which the maximum power transmission occurs is greater than the tuned frequency.

The theoretical predictions have been successfully validated by experimental measurements.

The effects of the TVA on wave transmission and reflection depend on the TVA parameters. The net effect is similar to that of a notch filter. The effectiveness of a TVA for narrow band disturbances thus depends crucially on how accurately the properties of the TVA are tuned. This raises the possibility of adaptive-passive control, in which the passive properties of the TVA can be adjusted to be optimal under changing conditions. Simplicity in design and a lower cost than active control are advantages of such an approach. The design of adaptive tuned vibration absorbers to control the flexural waves transmitting on a beam is discussed in the next chapter.

FIGURES FOR CHAPTER 3

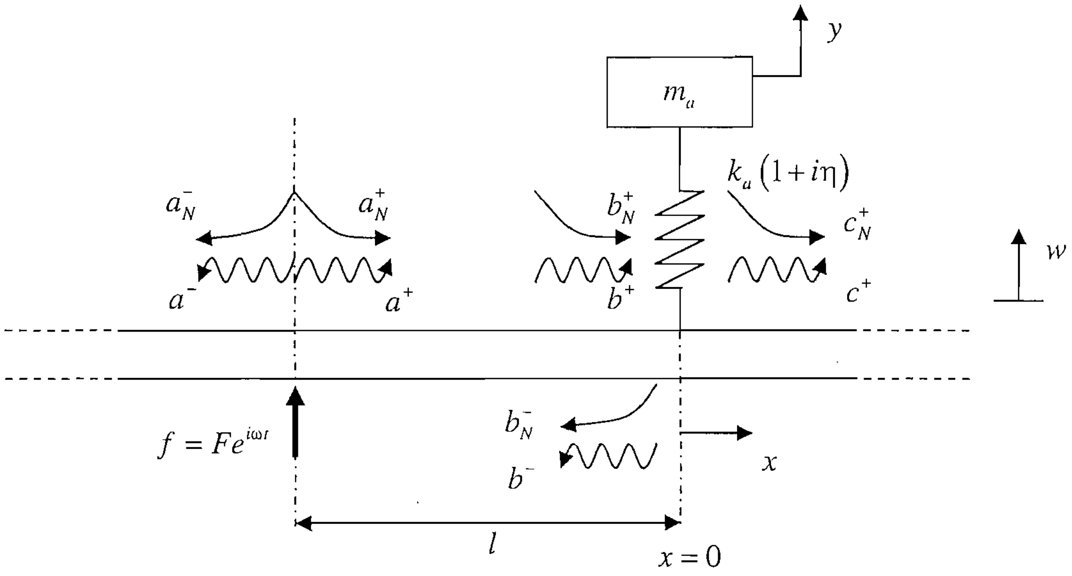

Figure 3.1. TVA in nearfield of point force.

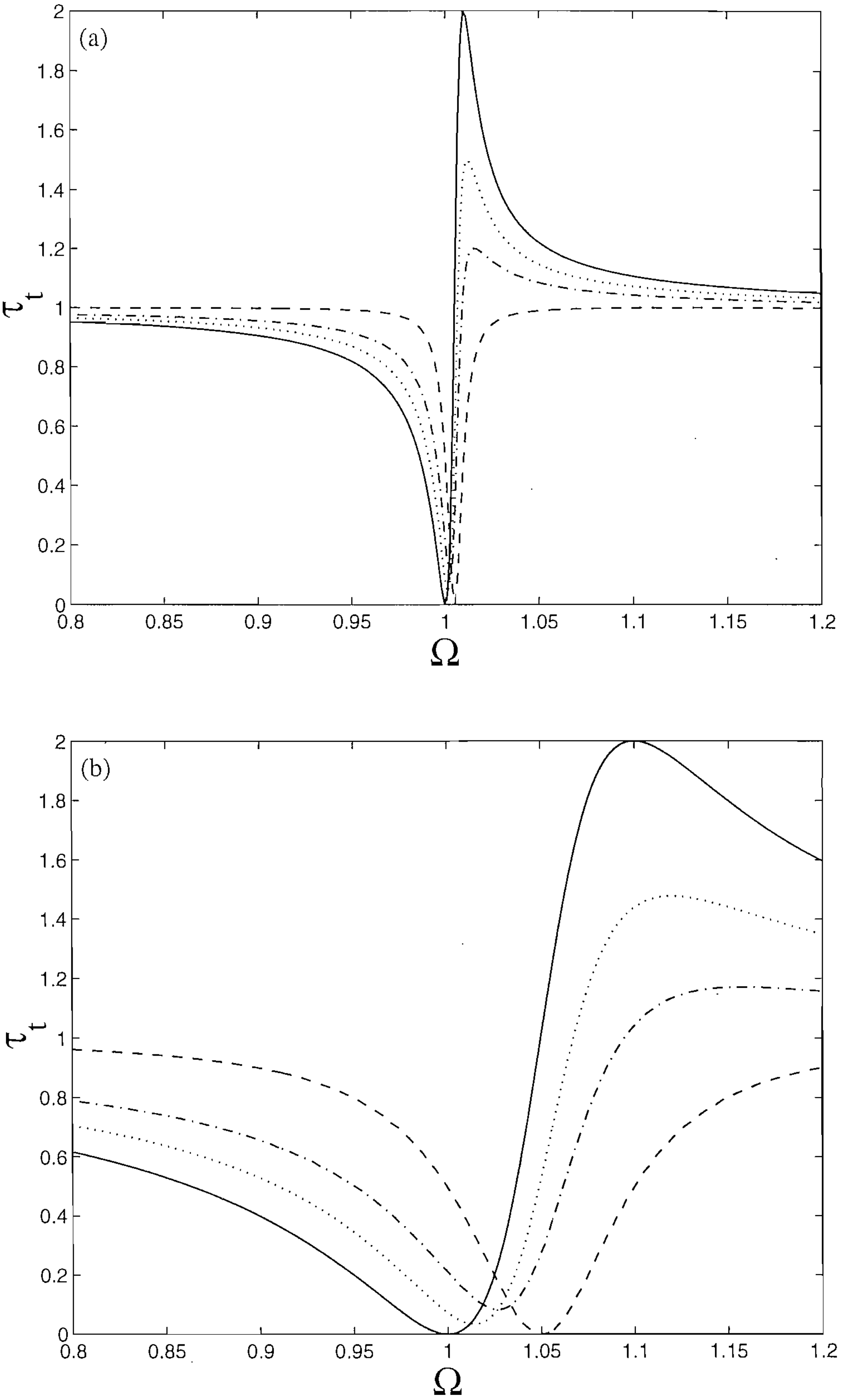

Figure 3.2. The transmission ratio as a function of Ω for various l/λ_a, $\eta = 0$:

(a) $\gamma = 0.01$; (b) $\gamma = 0.1$

_____ $l/\lambda_a = 0$; .... $l/\lambda_a = 0.05$; _._._._ $l/\lambda_a = 0.1$; _ _ _ _ _ $l/\lambda_a >> 1$.

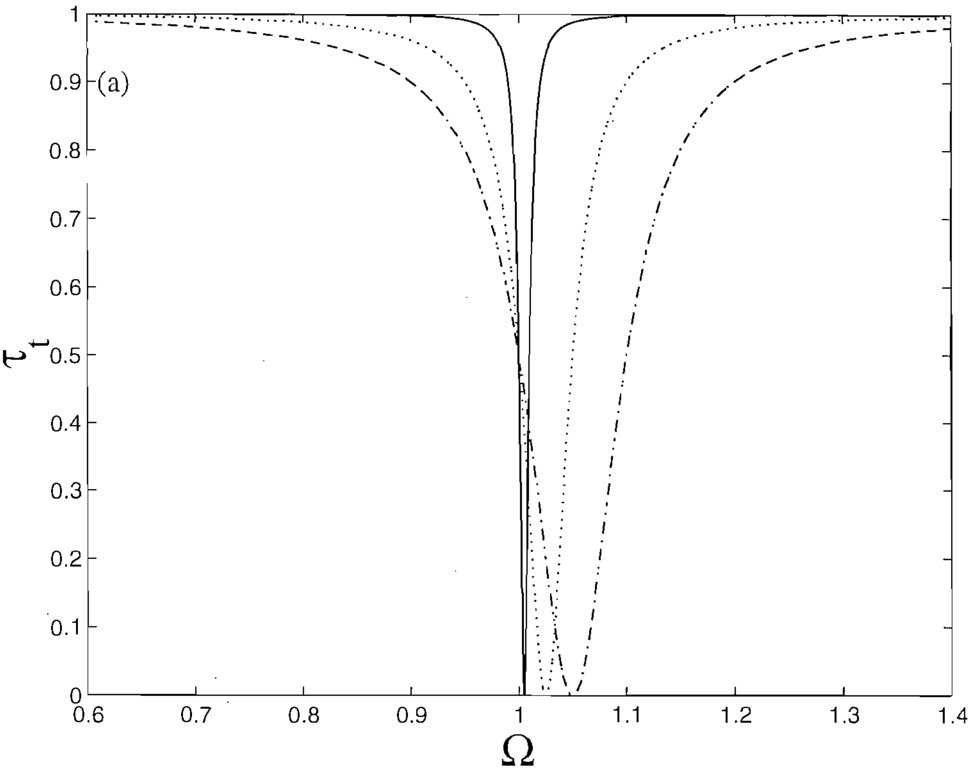

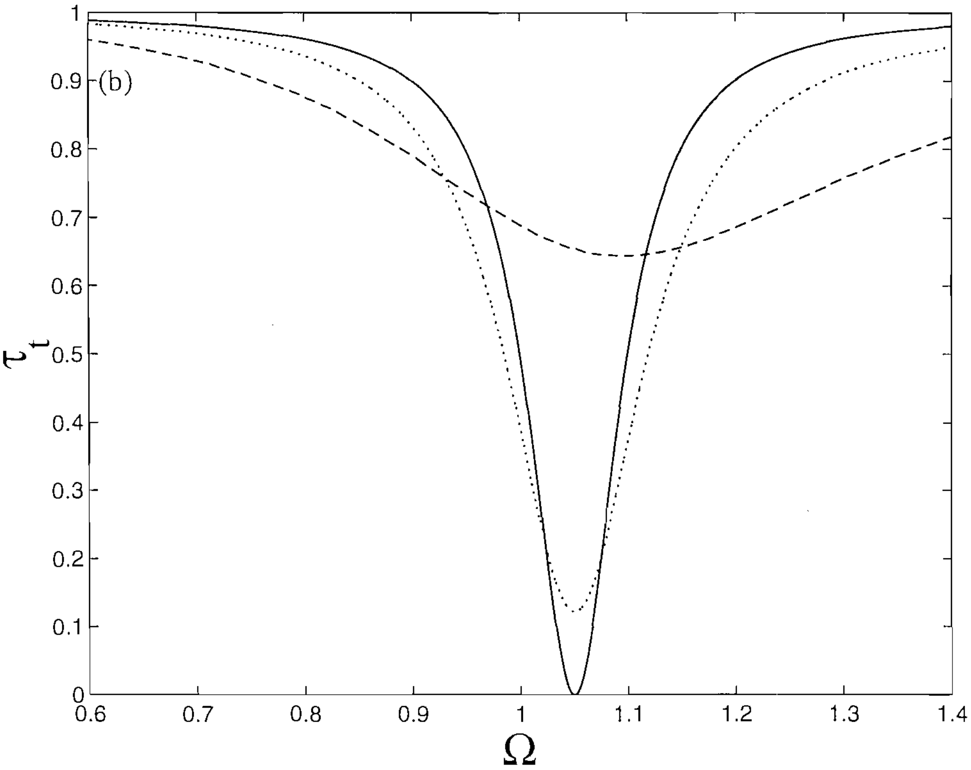

Figure 3.3. The transmission ratio as a function of Ω, TVA in the farfield:
(a) undamped TVA: _____ $\gamma = 0.01$; .... $\gamma = 0.05$; -.-.-.- $\gamma = 0.1$;
(b) damped TVA ($\gamma = 0.1$): _____ $\eta = 0$; .... $\eta = 0.05$; _ _ _ _ _ $\eta = 0.1$.

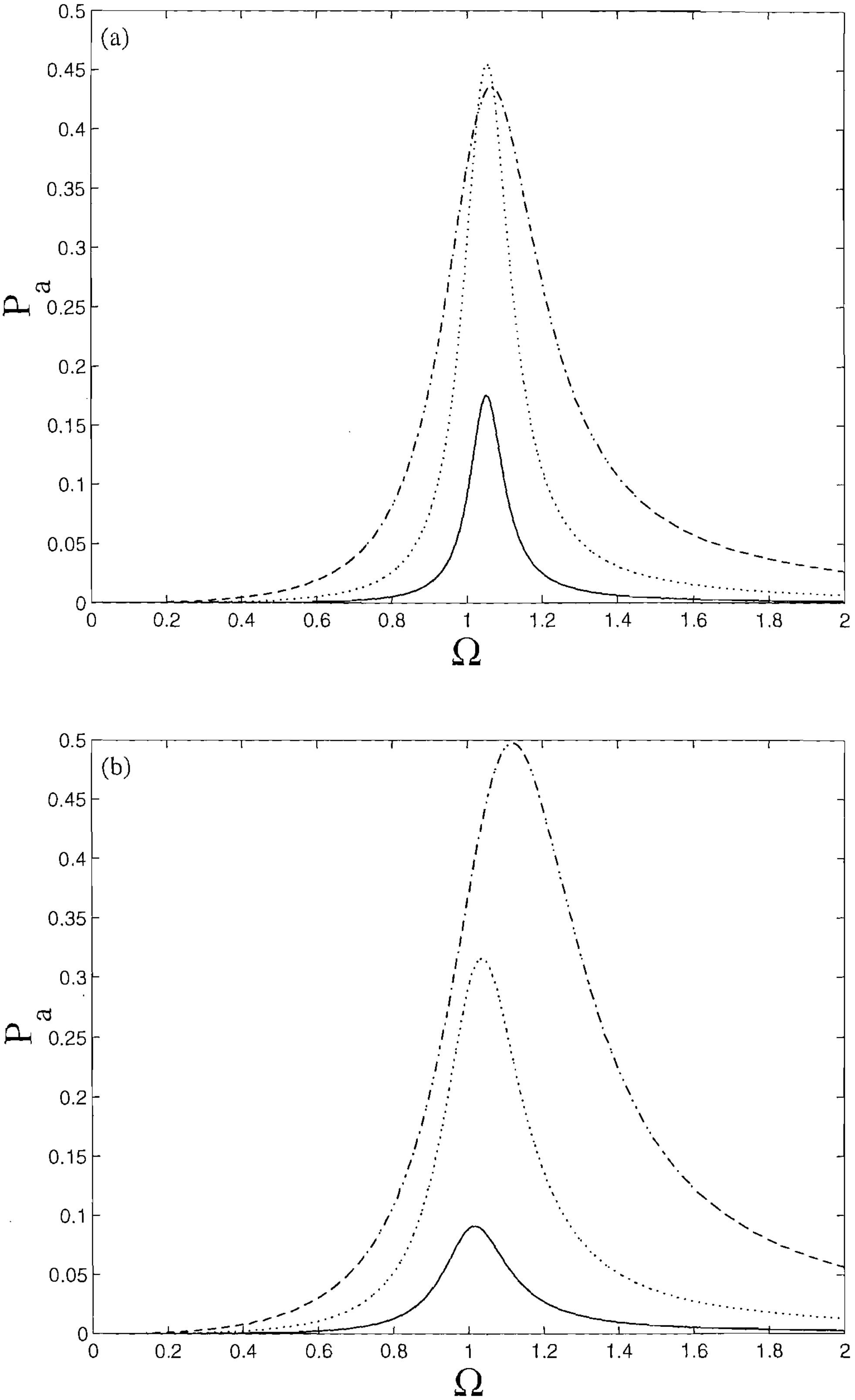

Figure 3.4. The normalised power absorbed by the TVA as function of Ω, $l/\lambda_a >> 1$.

(a) $\gamma = 0.1$: ——— $\eta = 0.01$; ………$\eta = 0.05$; -·-·-· $\eta = 0.2$.

(b) $\eta = 0.2$: ——— $\gamma = 0.01$; ………$\gamma = 0.05$; -·-·-· $\gamma = 0.2$.

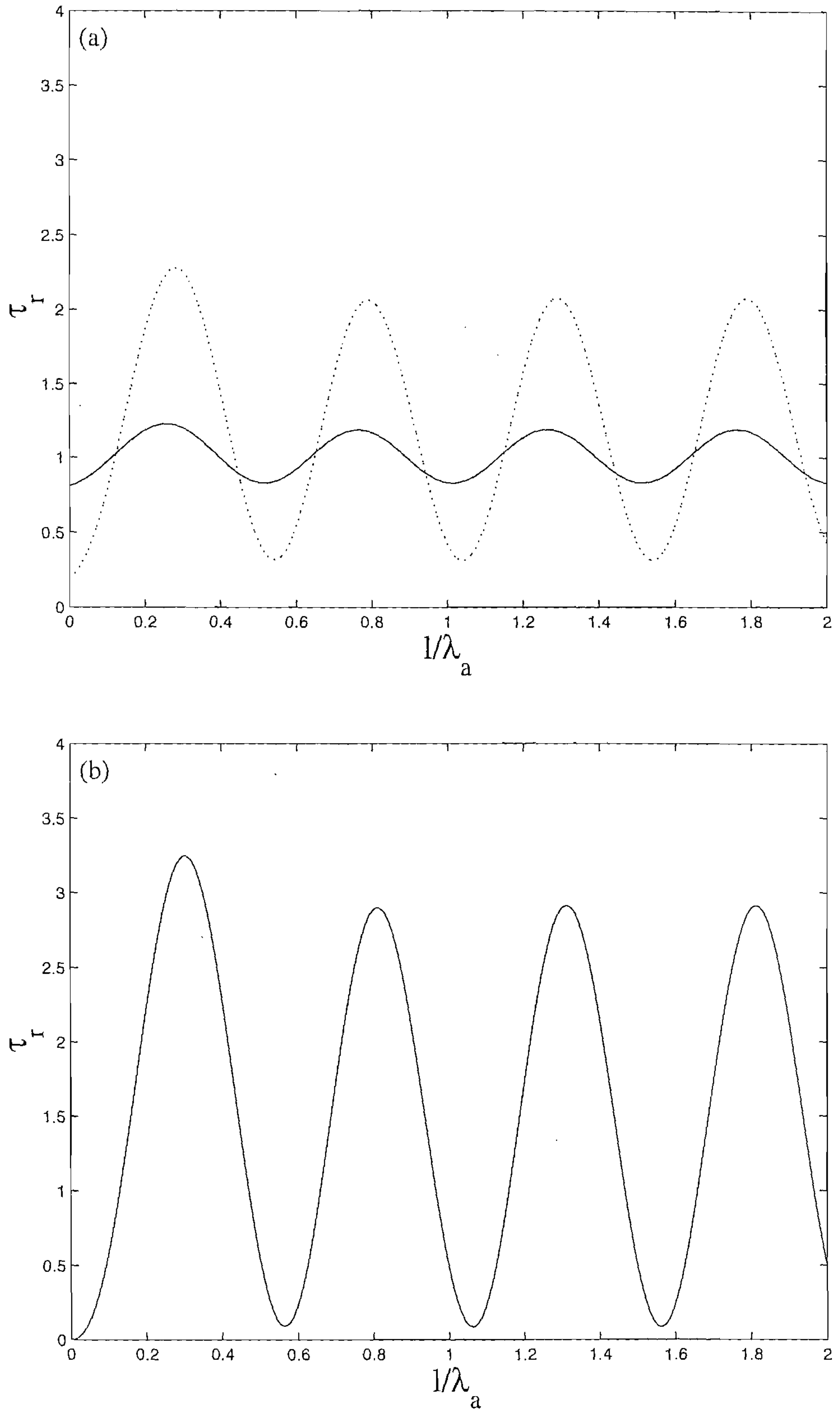

Figure 3.5. Reflection ratio as function of normalised length at frequency ratio $\Omega = 1$,

(a) $\eta = 0.1$; (b) $\eta = 0$.

—— $\gamma = 0.01$; ………. $\gamma = 0.1$.

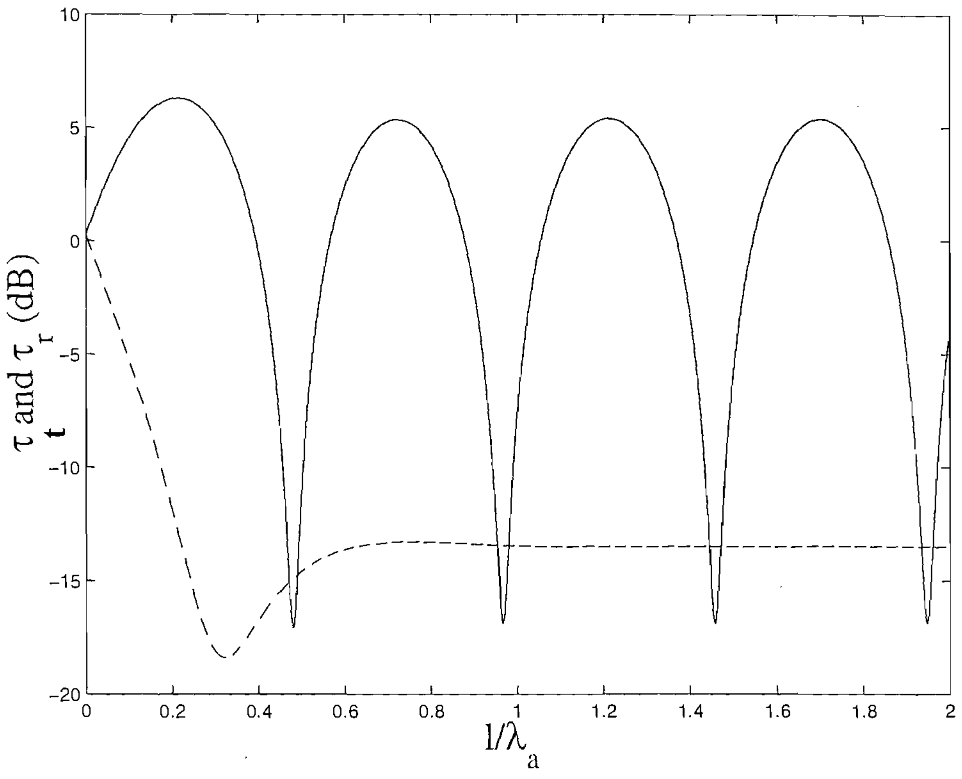

Figure 3.6. Reflection and transmission ratios as function of normalised length at tuned frequency ratio $\Omega = 1.04$, $\gamma = 0.07$ and $\eta = 0.01$.

———————τ_r ;- - - - - - - - - - - τ_t

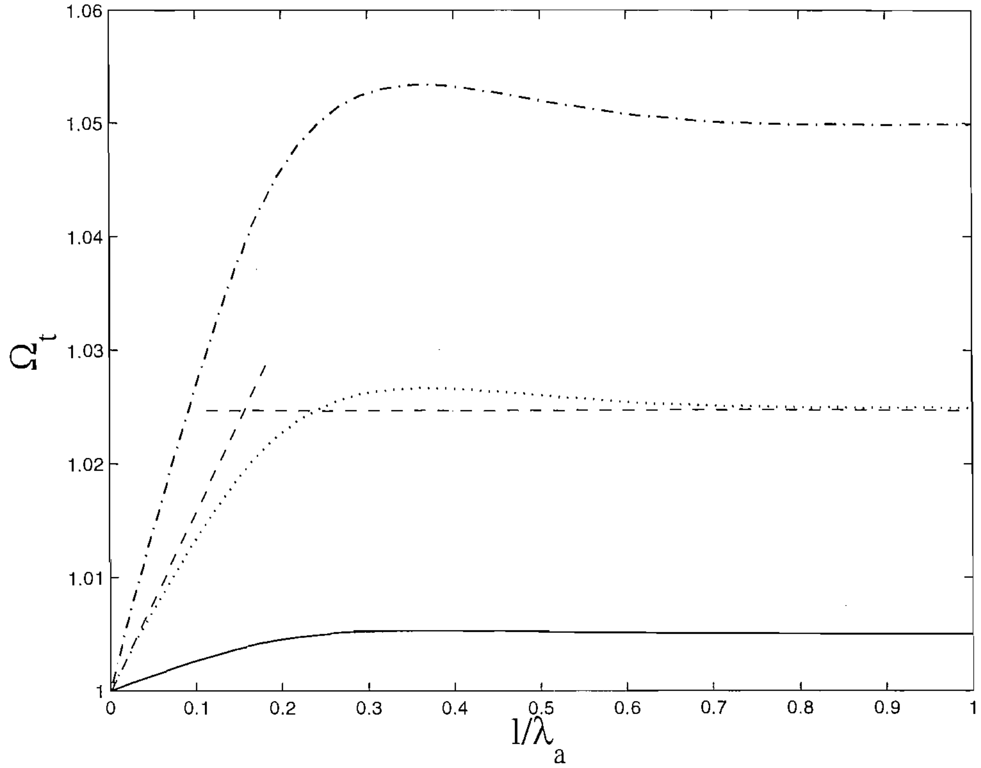

Figure 3.7. Optimum tuning frequency as a function of l/λ_a, $\eta = 0$.

_____ $\gamma = 0.01$; ....$\gamma = 0.05$; _._._._ $\gamma = 0.1$;

- - - - low and high l/λ_a asymptotes for $\gamma = 0.05$.

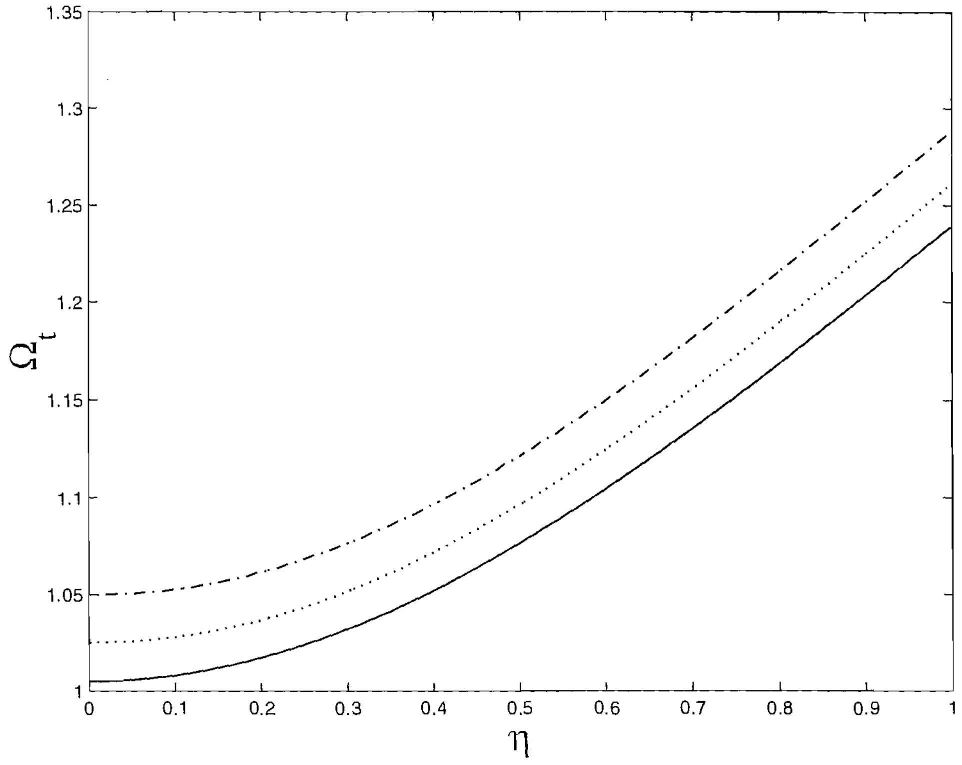

Figure 3.8. The effect of damping on the tuned frequency ratio Ω_t for an absorber located in the farfield:
——— $\gamma = 0.01$; ········ $\gamma = 0.05$; -·-·-·- $\gamma = 0.1$.

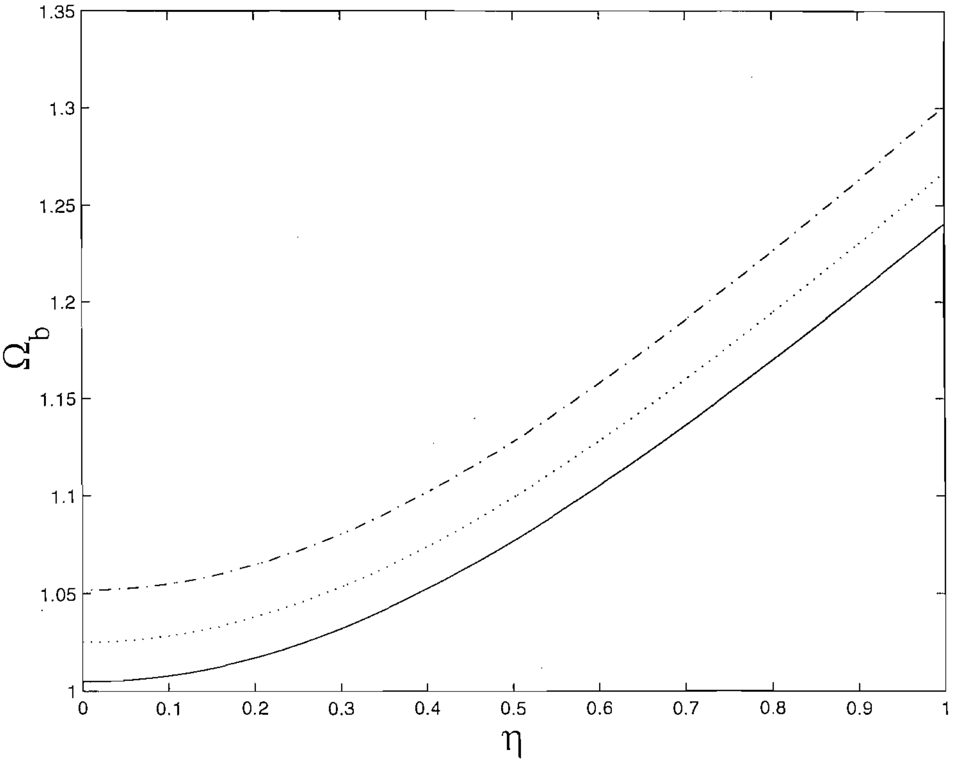

Figure 3.9. The effect of damping on the frequency at which the maximum power is absorbed Ω_b for an absorber located in the farfield:

——— $\gamma = 0.01$; ·········· $\gamma = 0.05$; -·-·-· $\gamma = 0.1$.

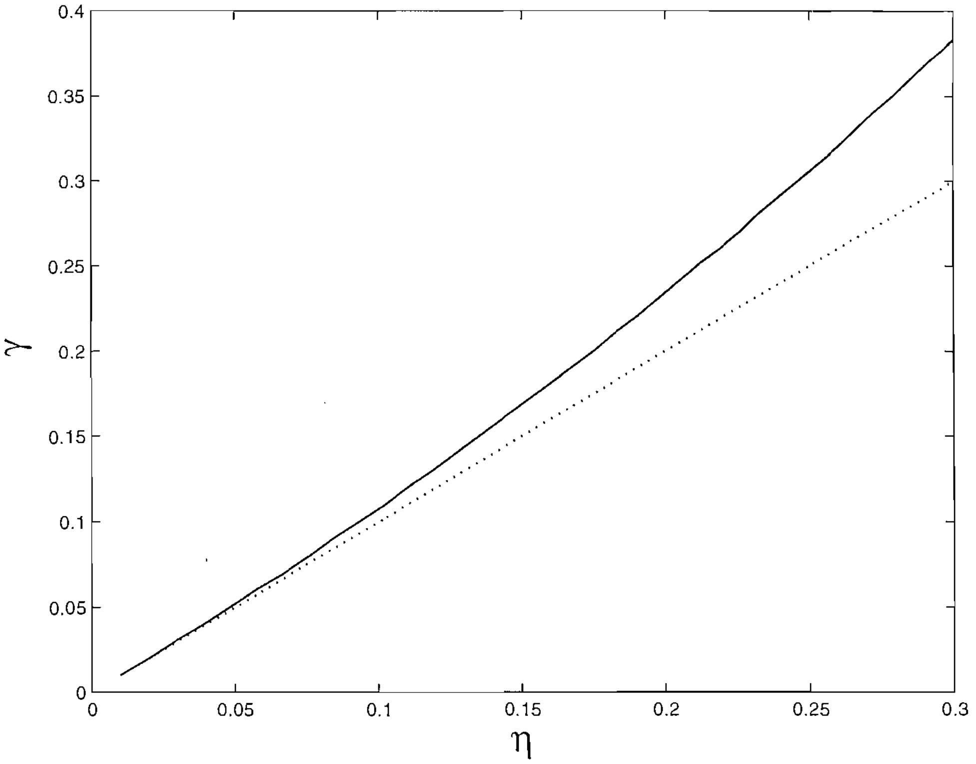

Figure 3.10. Optimum parameters for maximum power absorption.
———Numerical prediction; ··········approximation ($\gamma = \eta$)

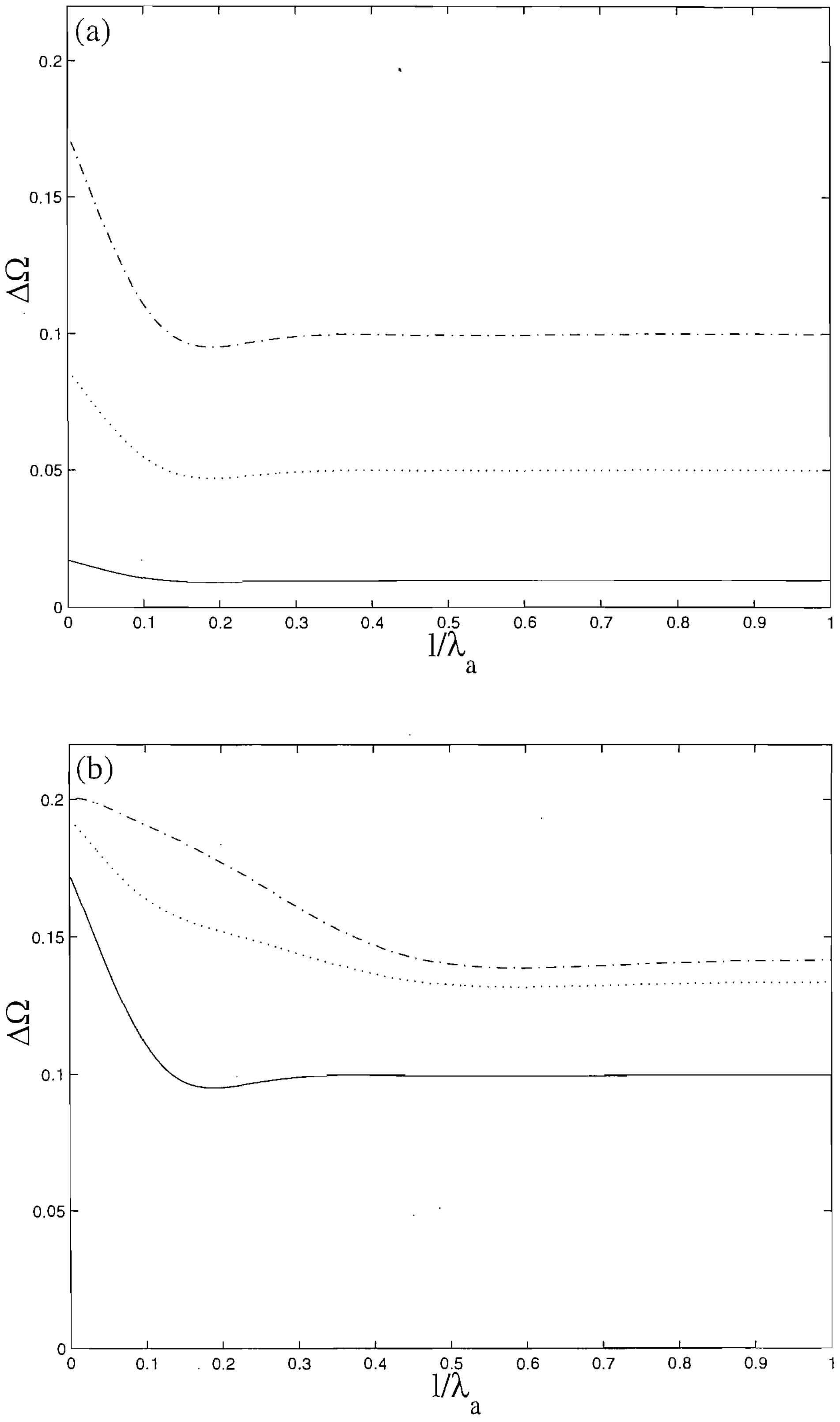

Figure 3.11. Frequency bandwidth as function of l/λ_a.

(a) undamped TVA: ———— $\gamma = 0.01$; .... $\gamma = 0.05$; -·-·-· $\gamma = 0.1$;

(b) damped TVA ($\gamma = 0.1$): ———— $\eta = 0$; .... $\eta = 0.05$; -·-·-· $\eta = 0.1$.

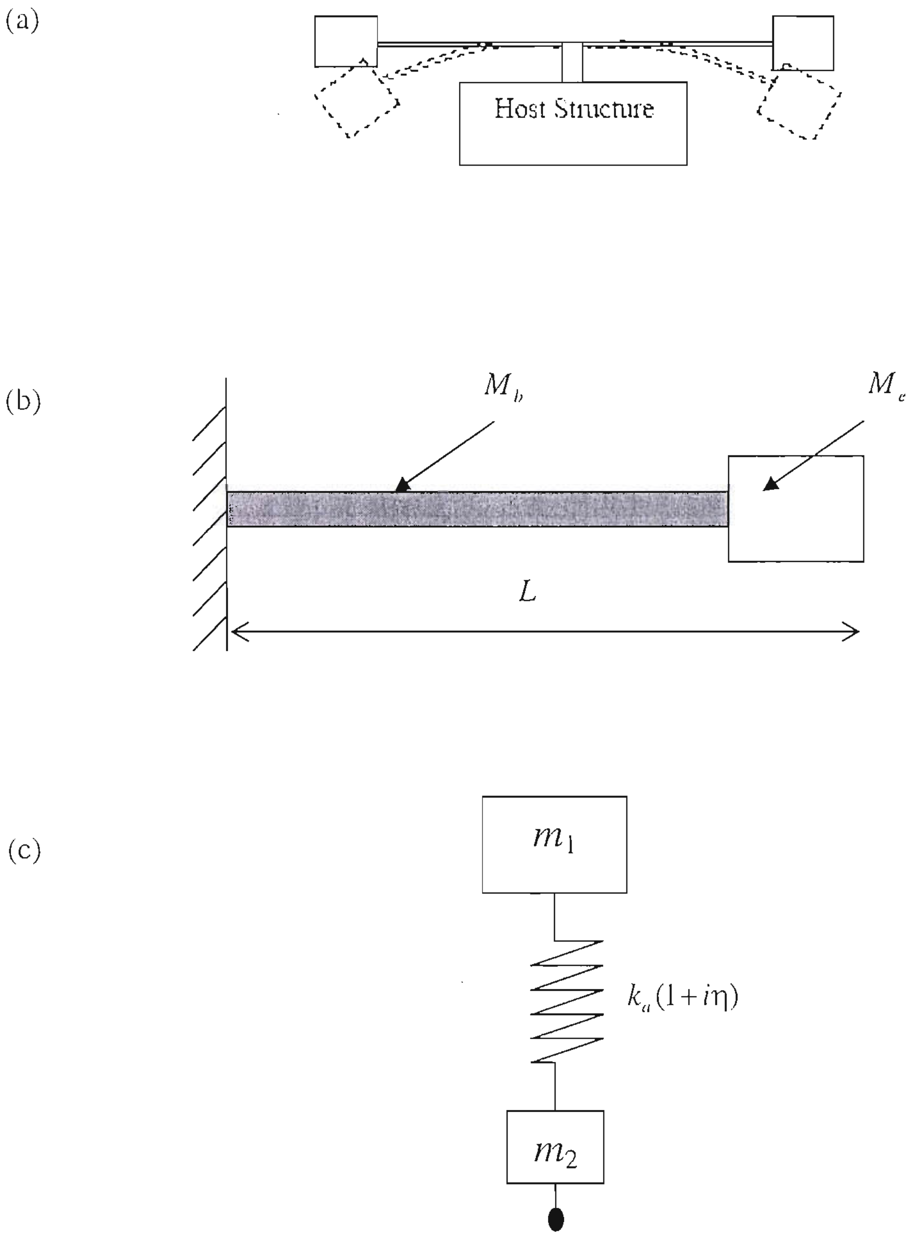

Figure 3.12. Beam-like absorber: (a) shape of vibration in a beam-like absorber at f_a; (b) a cantilever beam; (c) absorber modelled as a 2 degree of freedom system.

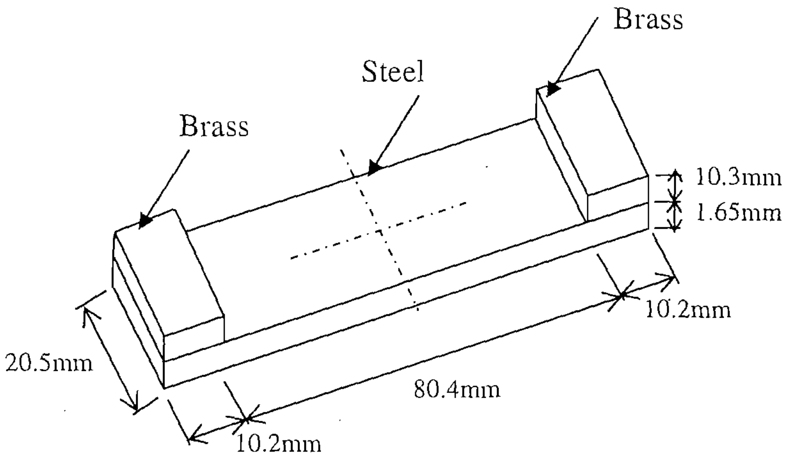

Figure 3.13. Sketch of the passive beam-like TVA

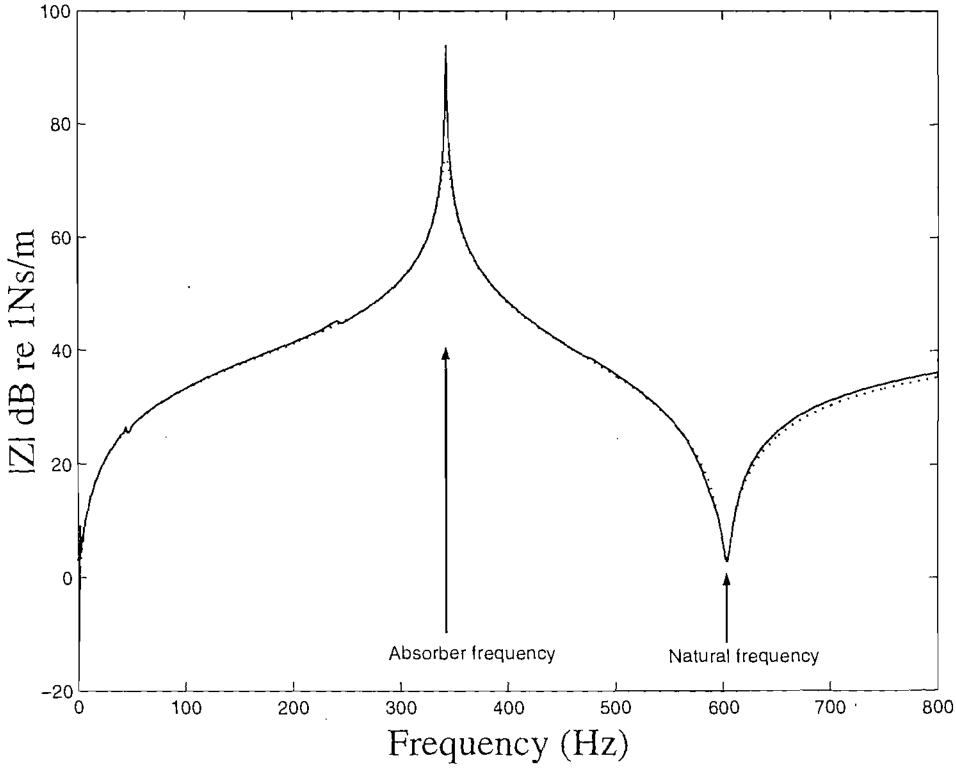

Figure 3.14. Impedance of the absorber:
——— experimental; ········· theoretical.

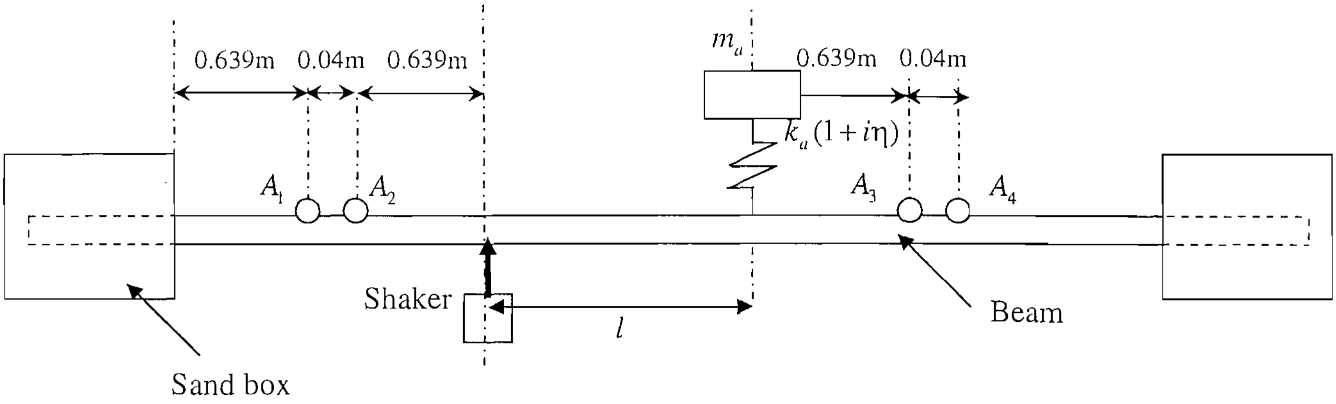

Figure 3.15. Experimental set-up.

○ accelerometer

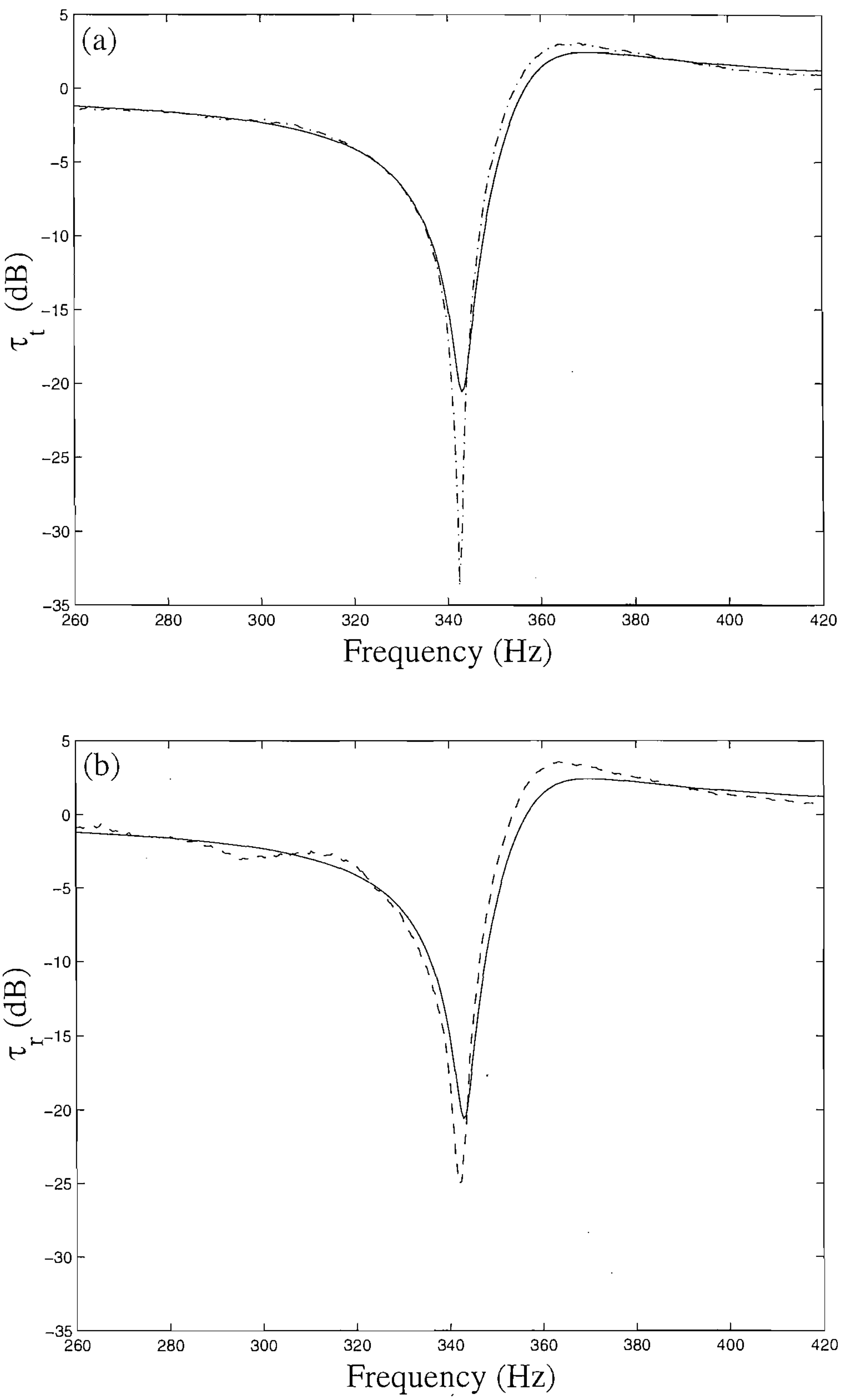

Figure 3.16. Transmission and reflection ratios, $l/\lambda_a = 0$:

(a) τ_t ; (b) τ_r ;

_____ $\tau_t = \tau_r$,theory;_._._._ τ_t ,experiment;_ _ _ _ τ_r ,experiment.

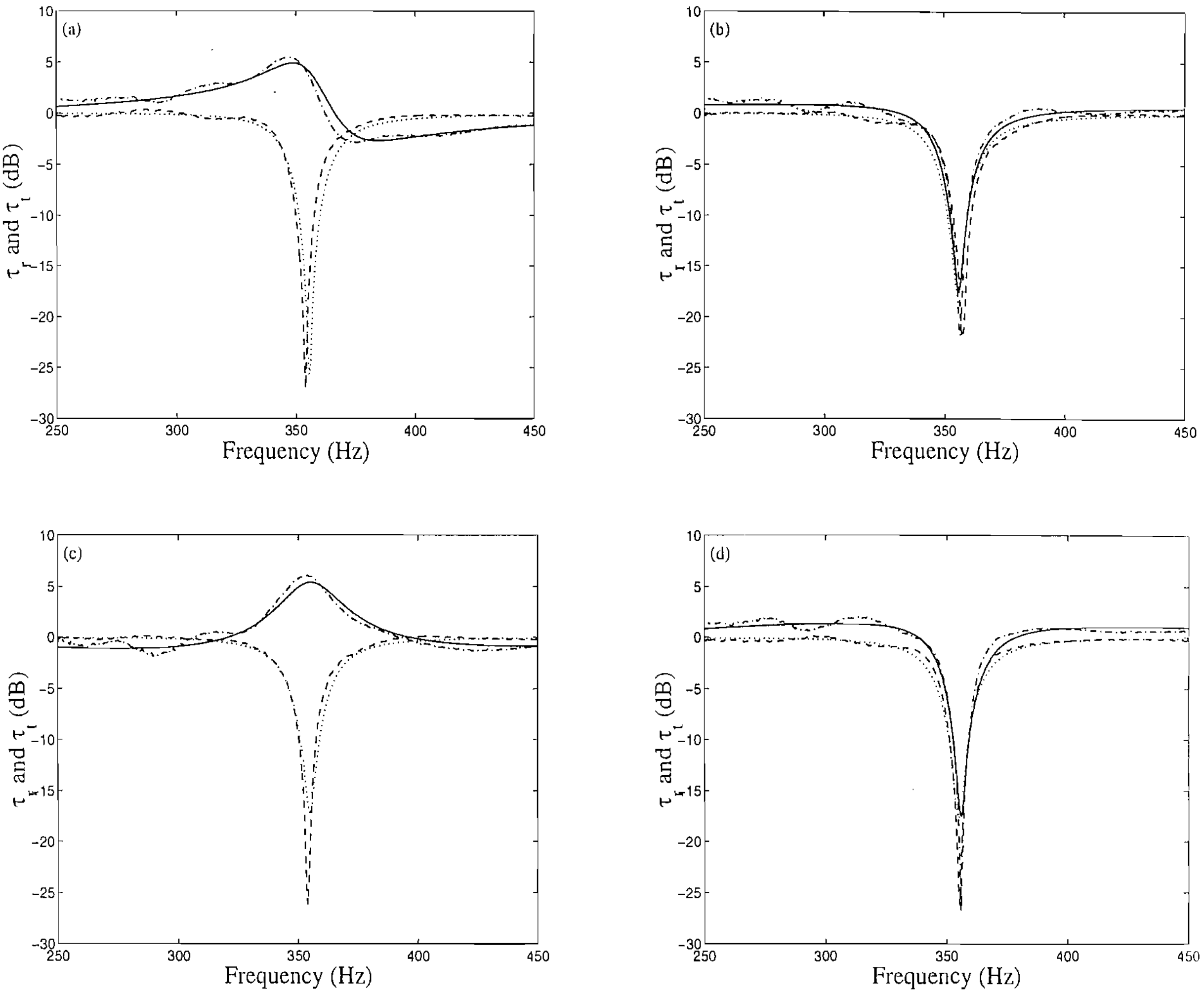

Figure 3.17. Power reflection and transmission: (a) $l/\lambda_a = 0.34$; (b) $l/\lambda_a = 0.49$; (c) $l/\lambda_a = 0.73$; (d) $l/\lambda_a = 0.98$;

_____ τ_r, theory; _._._._ τ_r, experiment; .... τ_t, theory; _ _ _ _ _ τ_t, experiment.

Property / Material	Young's Modulus E (GPa)	Density ρ (kg/m^3)
Steel	210	7850
Brass	105	8450

Table 3.1. Mechanical properties of the tuned vibration absorber.

CHAPTER 4: CONTROL OF VIBRATIONS WITH A VARIABLE STIFFNESS ABSORBER

4.1 Introduction

In Chapter 3 it was seen how flexural waves propagating on a beam structure can be significantly controlled at a specific frequency using a passive TVA. However, the passive absorber may become mistuned and lose its effectiveness if the disturbance frequency lies away from the narrow frequency band in which significant attenuation can be achieved.

Controlling the transmitted propagating wave at the tuned frequency requires that the TVA presents a spring-like impedance to the beam [30]. This fact can be used to overcome the limited effectiveness of the TVA, by changing the TVA's stiffness adaptively to suppress the flexural waves over a range of possible excitation frequencies. The adaptive change of the TVA's stiffness during operation is an example of adaptive-passive control discussed in Chapter 1. The device is therefore called an adaptive tuned vibration absorber (ATVA).

The aim of this chapter is to present the design and characterisation of an ATVA. The ATVA is then used to control the flexural waves propagating on a beam structure when the ATVA is located in the farfield of a point disturbance. Two different designs of ATVA are considered, both being thermal devices whose stiffness changes with temperature. One involves shape memory alloy (SMA) wires together with elastic elements for mounting purposes, while the other involves the same elastic elements with stainless steel wires. This absorber is designed to examine the performance of the elastic elements on changing the tuned frequency.

Originally the SMA ATVA was designed to control the transmitted waves on a beam. Following initial experimental work, the absorber that includes the elastic elements as the only elements whose stiffness varies with temperature, was used to control the transmitted waves.

Following this introduction, section 4.2 emphasises the influence of the TVA's stiffness on the tuned frequency. Section 4.3 investigates the adaptive properties of the materials chosen to be implemented in designing the ATVA. The geometric design of the ATVA is discussed in section 4.4. Experimental results validating the tunability of the ATVA are presented in section 4.5. Finally, section 4.6 contains the conclusion of the chapter.

4.2 The Influence of the Absorber Stiffness

The flexural waves propagating on an infinite beam can be completely suppressed at a single frequency if an undamped spring is fitted between a rigid foundation and the beam as discussed by Brennan [30]. The existence of damping in the spring permits some transmission of the propagating incident waves. However, fixing a spring to a rigid foundation might not be possible in practice. Therefore, the resultant TVA (spring-mass system) has to present a spring-like impedance to the beam at the tuned frequency.

For an undamped TVA ($\eta = 0$), the absorber impedance Z_{TVA} given by equation (3.31) is infinite when $\Omega = 1$. However, tuning a TVA attached to a beam to this frequency would pin the beam and only 3dB attenuation in the transmitted wave would be achieved. Furthermore, the TVA has a mass-like impedance for $\Omega < 1$, while for $\Omega > 1$ the TVA has a spring-like impedance. Consequently the tuned frequency $\Omega_t > 1$. This supports the analytical results derived in Chapter 3 for Ω_t.

4.3 Variable Stiffness Materials

Materials with variable elastic properties when simply actuated have been an interest of many researchers in the field of vibration control. One possibility is shape memory alloys (SMAs). Rustighi *et al* [12] and Williams *et al* [13] have shown that significant attenuation in the vibrations of a host structure can be achieved using an SMA ATVA.

Approximately 15% change in the tuned frequency was obtained. Other smart materials such as electro- and magneto-rheological fluids [52-54] can also be used. Nevertheless, the range of the elastic modulus of rheological fluids would seem to be much less than that of the SMAs, while the structural damping is much greater. This has a significant effect on the attenuation of the transmitted waves as discussed in Chapter 3 (i.e. increasing damping in the absorber reduces the transmission ratio).

Due to the proven effectiveness of SMA ATVAs in attenuating the vibrations of a host structure over a reasonable frequency range (i.e. approximately 15% change in tuned frequency), SMA wires were used in an ATVA to control the transmitted waves on a beam. These wires were used to construct a beam-like absorber. Non-metallic stiff materials, epoxy-resins and jelutong (i.e. type of wood) were used to mount the SMA wires and to form the centre of the absorber which is then attached to the beam. The elastic properties of the non-metallic materials are discussed in this section together with a brief description of SMAs. Another absorber identical to the SMA ATVA but with stainless steel wires replacing the SMA wires, was built to examine the effectiveness of the non-metallic materials in varying the tuned frequency. This absorber is called the thermo-elastic absorber.

4.3.1 Shape memory alloys

In 1932, Olander discovered an interesting phenomenon when working with an alloy of gold (Au) and cadmium (Cd). The Au-Cd alloy could be plastically deformed when cool and then heated to return to, or "remember", the original shape [55]. The phenomenon is known as the Shape Memory Effect (SME). Further research revealed other materials that demonstrate this phenomenon. In 1962, a group of researchers from the U.S. Naval Ordnance Laboratory lead by Buehler *et al* [56] discovered a nickel-titanium (Ni-Ti) alloy, Nitinol, which demonstrated this shape memory effect. The Nitinol shape memory alloy proved to be significantly less expensive, easier to work with, and less dangerous than previously discovered alloys. The term shape memory alloy (SMA) is applied to the group of metallic materials that has the ability to return to some previously defined shape or size when subjected to appropriate thermal and/or mechanical changes [57].

The unique behaviour shown by the SMAs is because they undergo a phase change in the solid state. The phases are called martensite and austenite. The martensitic phase exists at low temperatures and has a relatively soft and easily deformed phase. The molecular structure in this phase is twinned. The austenitic phase is the stiffer phase of shape memory alloys and exists at elevated temperatures. The molecular structure in this phase is body-centred cubic. In most SMAs, a temperature change of only 10°C is necessary to initiate this phase change. A mixture of both martensite and austenite phases may be exhibited by the SMA. The amount of the material that exists in the martensite phase is measured by the martensitic fraction (ξ) where $0 \leq \xi \leq 1$ [57]. When $\xi = 0$, then the only phase that exists in the molecular structure is the austenitic phase. On the other hand, $\xi = 1$ indicates that only the martensitic phase forms the molecular structure.

The characteristic temperatures at which the phase transformations take place are identified as M_s, M_f, A_s, and A_f, which represent the temperatures at the start and finish of the martensite transformation and, start and finish of the austenite transformation. A sketch of the temperature cycle with an illustration of the characteristic temperatures is shown Figure 4.1. At A_f and M_s, the martensitic fraction $\xi = 0$ while at M_f and A_s, $\xi = 1$ [52]. In this context, the shape memory effect is observed when the temperature of the shape memory alloy is cooled to below the temperature M_f where the alloy is completely composed of martensite. When the Nitinol SMA is below its transformation temperature, it can be deformed into any new shape. However, when the material is heated above its transformation temperature it undergoes the above described change in the crystal structure.

Cross *et al* [58] presented experimental results showing the variation of modulus of elasticity of an SMA rod with temperature. The elastic modulus of the Nitinol SMA is significantly increased by approximately 65% when the austenitic phase is reached. This change was found to be reversible upon cooling. Further experimental work that validated the significant variation of elastic modulus with temperature was presented by Rustighi *et al* [12]. About 47% change in the elastic modulus was achieved by changing the temperature of an SMA wire (i.e. changing the phase). The difference between the changes in the elastic modulus obtained by Cross *et al* [58] and Rustighi *et al* [12] can be due to using SMA specimens with different material composition, or due to the fact that Rustighi measured changes in the dynamic elastic modulus.

In addition to the change in material properties, there is some hysteresis which is an indicator of energy dissipation during the austenite to martensite and martensite to austenite transformations [59, 60]. An appropriate heat treatment to SMA would eliminate the hysteresis effect as discussed by Williams *et al* [61]. In addition to the two phases discussed earlier, an intermediate phase known as the rhombohedral phase (R-phase) can be achieved in the material without significant hysteresis. In addition, the R-phase has some attractive properties such as stability to thermal cycling and ageing. The existence of the R-phase depends on a number of factors like thermal history, cold work and solution treatment of the sample. Uchil *et al* [62] investigated the effect of the heat-treatment temperature on the R-phase transformation and associated hysteresis in prior cold-worked Nitinol by means of thermal analysis and electrical resistivity measurement. The width of thermal hysteresis associated with the R-phase transformation is small and decreases with increasing heat-treatment temperature.

The structural damping of SMA is important for this research as damping has a direct effect on the attenuation as pointed out previously in Chapter 3. Liang and Rogers [60] discussed the damping variation in SMA with temperature. The martensitic phase has a high damping capacity compared to the higher temperature phase (austenite). The high damping capacity in the martensitic phase is due to the stress-induced movement of the twin boundaries. This also occurs in the intermediate R-phase as discussed by Wu and Lin [63], though, as with other alloys, the interfacial mobility of crystals, transformation hysteresis, stress and strain amplitude, and excitation affect the damping characteristics of SMA. Piedboeuf and Gauvin [64] presented experimental results showing the effects of frequency and strain amplitudes on damping behaviour of Nitinol SMA. The structural damping increases when the strain amplitude increases. In contrast, increasing the frequency decreases the damping.

4.3.2 Non-metallic materials

The effect of temperature on the elastic modulus of the epoxy-resins and jelutong which are chosen for mounting the SMA wires is discussed in this section.

Epoxy-resins are man-made thermoset polymers and are used as adhesives, high performance coating and encapsulating materials. These polymers are formed from a chemical reaction where resin and hardener are mixed and then undergo a non-reversible chemical reaction to form a hard infusible product [65, 66]. This chemical reaction is called the curing process. Once cured, thermosets will not become liquid again if heated. In general, epoxy resins cure quickly and easily at practically any temperature from 5-150 °C depending on the choice of curing agent (hardener). The choice of resin and hardeners depend on the application and the properties desired.

Above a certain temperature, the mechanical properties of epoxy-resins will change significantly. This temperature is known as the "glass transition temperature (Tg)" and varies widely according to the particular resin system used, its degree of cure and whether it was mixed correctly. At temperatures above Tg, the molecular structure of the thermoset changes from that of a rigid crystalline polymer to a more flexible amorphous polymer. This change is reversible on cooling back below Tg. It is worthy of note that above Tg, properties such as modulus of elasticity drop sharply, and as a result the compressive and shear strength of the system do too. Other properties such as water resistance and colour stability also reduce markedly above Tg.

Jelutong (*Dyera cosulata*) is the other material that is chosen to mount the SMA wires at the centre of the absorber by containing the epoxy resins. Jelutong is classified as a hardwood type; however, the term has no reference to the actual hardness of the wood and is related to the porosity of the wood cells. In general, the mechanical properties (i.e. elastic modulus and density) of wood decrease when heated and increase when cooled [67]. This property is related to the moisture content. Nevertheless, at a constant moisture content and below $\approx 150°C$, the mechanical properties are approximately linearly related to temperature. The change in properties that occurs when wood is quickly heated or cooled at that condition is termed an immediate effect. This effect is reversible at temperatures below 100°C; that is the property will return to the value at the original temperature if the temperature change is rapid. Figure 4.2 shows the effect of temperature on the modulus of elasticity parallel to the grain. It is clear that increasing the temperature above the room temperature up to 100°C decreases the modulus of elasticity by about 30%. This effect slightly increases with moisture. The results are obtained from several investigations [67]. In addition to the reversible effect of temperature on wood, there is an irreversible effect at elevated temperature. This permanent effect indicates the degradation of the wood substance as the net weight and strength decrease.

4.4 Design of the Adaptive Absorber

In this section, the Nitinol material discussed previously is employed for designing an SMA ATVA. This is achieved with the aid of some mounting materials (i.e. epoxy-resins and jelutong). The design technique and the geometrical dimensions of the absorber are described. The effect of varying the ATVA dimensions on the overall stiffness and in turn on the tuned frequency is also discussed. In order to investigate the tunable range the mounting materials would exhibit, a typical design to the SMA ATVA is established using the same mounting system with an alloy whose mechanical properties do not change with temperature up to 700°C and which has the same electrical resistivity (i.e. stainless steel).

4.4.1 Design and construction

The principal of operation of the ATVA is the same as that of the passive beam-like absorber implemented in Chapter 3. Thus, the ATVA is realised as two symmetric cantilevers with masses at the ends. However, each cantilever is represented by n SMA wires where n is an integer. Each wire has a diameter d and a second moment of area $I = (\pi / 64) d^4$. Consequently, the absorber frequency ω_a given by equation (3.40) can be rewritten as

$$\omega_a^2 \approx \frac{3nEI}{L^3 \left(0.243 n M_b + M_e\right)}. \tag{4.1}$$

The other variables are the same as those in equation (3.40).

The design of the absorber can be manipulated to target a specific frequency. This will be the default frequency of the absorber ω_a. Increasing the number and the diameter of the wires n and d respectively, increases the absorber frequency since the stiffness of each cantilever $k = 3EI / L^3$ increases. On the other hand, increasing the length of the wires L and/or the concentrated tip mass M_e decreases ω_a (i.e. $\omega_a \propto L^{-3/2}$).

Attaching a concentrated mass at the end of each cantilever would increase the mass ratio γ. In addition, changing the position of the concentrated mass on the cantilever would vary the effective length of the absorber. This in turn would allow the absorber frequency to be adjusted.

4.4.2 Shape memory alloy absorber

An SMA ATVA was constructed using 4 pairs of Nitinol SMA wires (2 mm diameter and 45 mm long each). The wires are connected in parallel such that the DC current passes from one wire to another to increase their temperature. Figure 4.3a shows a sketch of the electrical circuit of the SMA ATVA. The relevant properties of the Nitinol wires are tabulated in Table 4.1. A block of brass of dimension $3\text{mm} \times 6\text{mm} \times 25.5\text{mm}$ was attached on each side and a block of jelutong was fitted at the centre and filled with epoxy-resins to mount the SMA wires and form a stiff compound. Nevertheless, the compound has a relatively very low density to ensure that there is little influence on the dynamics of the system. This construction should simulate a beam-like absorber (two identical cantilevers). The total mass of the SMA ATVA is about 40.7g. Table 4.2 shows the mechanical properties of the mounting materials (i.e. epoxy-resins and jelutong). The brass blocks are designed such that the effective length of the cantilevers can be altered as required (see Figure 4.3b). In addition, an electrical/thermal insulator is used to prevent the brass blocks from causing a short circuit. Table 4.3 shows the physical properties of brass.

4.4.3 Thermo-elastic absorber

In order to investigate any effect the mounting materials may exhibit, 4 pairs of stainless steel wires (grade 316) were used in a design and with dimensions similar to those of the SMA ATVA shown in Figure 4.3. This absorber is called the Thermo-elastic absorber. The net mass of this absorber is about 45.7g.

Stainless steel has electrical resistivity similar to that of the Nitinol material. Therefore, the stainless steel wires heat up in a similar way to the Nitinol wires. However, the crystalline structure of stainless steel does not change with temperature up to 700°C [68]. Table 4.4 includes the physical properties of the stainless steel wires.

4.5 Experimental Work

In order to assess the effectiveness of the adaptive absorbers in controlling the flexural waves at various tuned frequencies, a series of experiments was carried out. First, the tuning range of the absorbers was investigated. Next, the absorbers were attached to a beam to control the flexural waves at various tuned frequencies.

4.5.1 Tuning range of the adaptive absorbers

Initially, the characteristics of the SMA ATVA were estimated at the ambient temperature which was about 16°C (i.e. no DC current input), by following the same techniques and using the same equipment utilised for the TVA that was described in section 3.5.2. Therefore, the following characteristics were estimated experimentally: $f_a = 140\,\text{Hz}$, $\gamma = 0.024$ and $\eta = 0.02$ where the effective mass of the absorber $m_a = 24.7\,\text{g}$. Note that the theoretical prediction of the absorber frequency is $\hat{f}_a \approx 120\,\text{Hz}$. This was estimated from the data provided in Tables 4.1 and 4.3 and using equation (4.1).

Increasing the absorber frequency above 150 Hz would avoid the significant effects of the nearfield waves around that frequency when the absorber is attached to the steel beam discussed in the previous chapter to control the transmitted waves.

The effective length of each cantilever was reduced to 30 mm by sliding the tip masses (i.e. brass blocks) at each cantilever towards the centre of the absorber. The net mass of the concentrated blocks at the end of each cantilever is now represented by the mass of the brass blocks plus the mass of the SMA wires outstanding from the effective length. Note that the mass ratio of brass blocks to that of the outstanding SMA wires is approximately 6:1. The reduction in the effective length has increased the stiffness of the absorber and in turn the absorber frequency to 217 Hz which was obtained experimentally. In addition, γ slightly increased to 0.028. For the new effective length, the theoretical prediction of the absorber frequency $\hat{f}_a = 223\,\text{Hz}$. This was predicted by taking into consideration the outstanding mass of the SMA wires. However, ignoring the mass of the outstanding SMA wires would increase the difference between estimated and measured absorber frequencies by $\approx 6.5\%$.

The performance of the SMA ATVA in changing the absorber frequency was manually tested using a power supply Lambda ZUP10-20 to heat up the SMA wires. This power supply could generate a current I of 21 A. The surface temperature of the wires was measured using a Fluke 52 thermocouple. A constant current was input to the SMA ATVA and the characteristics of the SMA ATVA were measured when the steady-state was reached for each current (i.e. temperature). This was obtained by implementing the same techniques and equipment described in section 3.5.2. The time required to reach the steady-state was found experimentally to be about 15 minutes. Heating the ATVA for a time longer than 15 minutes did not significantly change the surface temperature of the ATVA.

The variation of the absorber frequency f_a and the resonance frequency f_r of the ATVA with temperature is shown in Figure 4.4. The frequencies were obtained experimentally, as discussed in section 3.5.2 for a beam-like absorber, when the steady-state is reached for each temperature. Increasing the temperature below $A_s \approx 45°\text{C}$ decreases both f_a and f_r. This was unexpected behaviour. In addition, increasing the temperature should increase the stiffness of the SMA wires and in turn the absorber frequency. However, heating the SMA wires at temperatures above A_s and below $A_f \approx 60°\mathrm{C}$ increased both f_a and f_r. Reduction in stiffness of the ATVA was also observed for temperatures above A_f where the phase of the SMA has completely transformed to austenite. It was thought that, the reduction in the ATVA's stiffness at temperatures $T < A_s$ and $T > A_f$ can be due to significant softening that could have arisen in the centre (mounting materials) of the SMA ATVA. Increasing the temperature of the SMA wires above A_s activated the phase transformation from the martensitic phase to the austenitic phase and the increase in the stiffness of the SMA wires is counteracted by the softening effect of the material in the mounting block of the absorber. When the phase of the SMA is fully austenitic, i.e. at temperatures above A_f, then any increase in temperature will no longer increase the stiffness of the SMA wires, and further softening occurs in the materials in the mounting block of the absorber. The maximum change achieved in the absorber frequency was about 20%.

It is noted that the hysteresis caused upon heating and cooling is less than $10°\mathrm{C}$. The behaviour of the SMA ATVA with temperature was verified by repeating the test and the results are shown in Appendix 2.

Figure 4.5 shows the variation of the absorber's stiffness k_a with temperature. The absorber's stiffness was calculated in the same way to the stiffness of the TVA discussed in section 3.5.2, using the characteristics of the ATVA obtained experimentally, when the steady-state is reached for each temperature. The softening effect is noticeable at temperatures $T < A_s$ and $T > A_f$.

The variation of structural damping of the SMA ATVA with temperature is shown in Figure 4.6. This was estimated experimentally using the circle fit method when the steady-state was reached for each temperature. It is clear that the damping increases rapidly for temperatures between $50°\mathrm{C}$ and $70°\mathrm{C}$. This contradicts the damping behaviour of SMAs on phase transformation as observed by Liang and Rogers [60].

However, the glass transition temperature of the epoxy-resins is $T_g \approx 40°\mathrm{C}$. Above this temperature the crystalline structure of the epoxy-resins becomes amorphous (rubbery structure); this is accompanied by a high level of damping. Moreover, when $\xi \approx 0$ (martensitic phase is completely transformed above A_f), the structural damping of the SMA wires reduces significantly and in turn the overall damping of the SMA ATVA as shown at temperatures above $A_f \approx 60°\mathrm{C}$.

The temperature distribution along the SMA wires was investigated by performing a series of tests. A DC current of 9A was applied to the SMA ATVA for up to 15 minutes in each test and the surface temperature was measured at two different points along the absorber. The maximum difference in temperature measured along the SMA wires and the brass blocks was less than $10°\mathrm{C}$. Appendix 3 includes the results obtained from the experimental tests, showing the temperature difference with time at various points along the absorber.

The experimental tests described above for the SMA ATVA indicated that the change in elastic properties of the mounting block could be larger than those of the SMA. Hence the experiments were repeated for the thermo-elastic absorber to investigate the effect of temperature on the characteristics of the mounting materials. The effective length of the absorber was reduced to 30 mm similar to the SMA ATVA, in order to increase the absorber frequency and the mass ratio. The following parameters were measured at the ambient temperature; $f_a = 387.5\,\mathrm{Hz}$, $\gamma = 0.04$ and $\eta = 0.018$. The estimated absorber frequency is $\hat{f}_a \approx 485\,\mathrm{Hz}$.

Figure 4.7 shows the effect of temperature on the frequencies f_a and f_r of the thermo-elastic absorber. It is clear that increasing the temperature of the absorber decreases both f_a and f_r. Heating the stainless steel wires heats up the mounting materials fitted at the centre of the absorber. It was found that the maximum change in the absorber frequency is about 27%. Therefore, the tuning range obtained by the thermo-elastic ATVA is greater than that obtained by the SMA ATVA.

The behaviour of the thermo-elastic ATVA with temperature was repeated and the results are shown in Appendix 4. The maximum hysteresis recorded was about 12°C.

The significant reduction in the absorber frequency with temperature is directly related to the softening that has arisen in the material in the centre of the absorber. Figure 4.8 shows the variation of the stiffness of the thermo-elastic ATVA with temperature. It is clear that the stiffness of the absorber decreases significantly with temperature.

Figure 4.9 shows the variation of structural damping of the thermo-elastic ATVA with temperature. It is clear that increasing the temperature of the ATVA up to 65°C increases the damping. However, at temperature greater than 65°C the structural damping decreases significantly. This can be related to the stress changes in the mounting materials as the temperature changes.

4.5.2 Implementation of the adaptive absorbers

In this section, the control of the transmission of propagating flexural waves on a beam structure using the ATVAs discussed in the previous section is described. The tuned frequency of the ATVAs was manually changed using a power supply (Lambda ZUP10-20) and the surface temperature was monitored using a thermocouple (Fluke 52).

The effectiveness of the ATVAs for controlling the transmitted waves was examined at a steady temperature. Each ATVA was attached to the steel beam discussed in Chapter 3. The beam was excited by a Ling V201 shaker with band limited random noise over a frequency range 50 – 800 Hz. The experimental set-up is shown in Figure 4.10. The propagating wave amplitudes were estimated using the frequency domain wave decomposition approach discussed in Chapter 2. The transmission and reflection ratios were predicted from the estimated wave amplitudes as discussed in Chapter 3. The experimental results, reported in this section, validate the control of the transmitted waves for an ATVA attached in the farfield of the point disturbance ($l/\lambda_a > 1$).

Figure 4.11a compares the numerical prediction of the transmission ratio τ_t given by equation (3.18) to the experimental result for the SMA ATVA attached to the beam with no current input (i.e. at the ambient temperature $\approx 18°\mathrm{C}$). The maximum attenuation achieved at the tuned frequency, $f_t \approx 219\,\mathrm{Hz}$, was approximately $9\mathrm{dB}$. However, the thermo-elastic ATVA has a maximum attenuation of 11dB with a larger bandwidth $\Delta\Omega$ as shown in Figure 4.11b. Note that the mass ratio γ for the thermo-elastic ATVA is greater than that of the SMA ATVA. In general, there is good agreement between the theoretical and experimental results.

The ability of the ATVAs to control the transmission at various tuned frequencies was examined by manual adjustment of the ATVAs temperature. Results are shown in Figure 4.12 for the SMA ATVA. Heating up the SMA wires at various temperatures achieves a clear attenuation (notch) in τ_t around the tuned frequency for each temperature when the steady-state is reached (see Figure 4.12a). The attenuation attained at each temperature is directly related to the structural damping as discussed in Chapter 3 (i.e. increasing the loss factor reduces the attention in the transmission ratio). The ultimate change achieved in the tuned frequency was about 20%, with the minimum tuned frequency being $202.2\,\mathrm{Hz}$ and the maximum tuned frequency being $252.7\,\mathrm{Hz}$. Figure 4.12b shows the attenuation of the transmission ratio at various temperatures during cooling. The tuned frequencies obtained upon heating (Figure 4.12a) are not exactly the same as those obtained upon cooling (Figure 4.12b). This is due to hysteresis.

Figure 4.13 shows the transmission ratio at various temperatures using the thermo-elastic ATVA. Using this ATVA increased the ultimate change achieved in the tuned frequency ($\approx 28\%$). The minimum tuned frequency $f_{t,\min} \approx 282.76\,\mathrm{Hz}$ was achieved at the highest temperature reached $T_{\max} = 95°\mathrm{C}$, while the maximum tuned frequency $f_{t,\max} \approx 392.5\,\mathrm{Hz}$ was achieved at the ambient temperature $T_{ambient} \approx 18°\mathrm{C}$. The maximum attenuation achieved was about 12 dB. Note that the degree of attenuation at the tuned frequency is related to the damping of the thermo-elastic ATVA discussed in the characterisation of the ATVA and shown in Figure 4.9.

Another steel beam with a smaller cross-sectional area ($3.2\text{mm} \times 24.6\text{mm} \times 5630\text{mm}$) was used to highlight the effect of the mass ratio on f_t, $\Delta\Omega$ and the maximum attenuation in τ_t. The measured wavelength of the new beam was such that $k = 1.17\sqrt{f}$. The mass ratio of the thermo-elastic ATVA was predicted to be $\gamma = 0.22$ (i.e. at the ambient temperature). Note that the absorber frequency ($f_a = 387.5\,\text{Hz}$) only depends on the characteristics of the absorber. Figure 4.14 compares the experimental results obtained for the attenuation achieved in τ_t for both beams when no current is input to the thermo-elastic ATVA. The theoretical prediction for the different mass ratios is also plotted. The maximum attenuation achieved for the smaller cross-section beam is about 20 dB. This is approximately twice the attenuation achieved for the larger cross-section beam. There is about 2% difference in the tuned frequency obtained by the numerical prediction and the experimental results; this might be due to the variation in the ambient temperature which affects the stiffness of the ATVA and in turn f_a.

Figure 4.15 shows the transmission ratio at various temperatures using the thermo-elastic ATVA attached to the beam with the smaller cross-section area ($\gamma = 0.22$ at the ambient temperature). The change achieved for the tuned frequency was about 27%. The tuned frequency at the ambient temperature was about 420 Hz, while that at the maximum temperature reached, $T_{\max} = 81°\text{C}$, was about 310 Hz.

4.6 Discussion and Conclusions

Two variable stiffness beam-like absorbers have been introduced in this chapter. The first absorber is called the SMA ATVA and it employs shape memory alloys, epoxy-resins and jelutong as the variable stiffness elements, while the second absorber is called the thermo-elastic ATVA and it only employs epoxy-resins and jelutong as the variable stiffness elements. The stimulus of both designs is varying the temperature of the elements by means of a DC current.

The two ATVAs were implemented and manually tuned to control the transmitted propagating waves at various tuned frequencies. Experimental results have proven the effectiveness of both absorbers. The ultimate change achieved in the tuned frequency using the SMA ATVA was about 20%. Part of this was a result of the softening of the epoxy-resins and jelutong in the centre of the SMA ATVA. A higher tunable range, about 27%, was obtained using the thermo-elastic ATVA which only includes the epoxy-resins and jelutong materials as the variable stiffness elements. In addition, greater attenuation was also obtained. However, heating-up the thermo-elastic ATVA would increase the structural damping which in turn would limit the attenuation of the transmitting power.

Self-tuning control of transmitted power on a beam structure using these variable stiffness vibration absorbers will be discussed in the next chapter. The thermo-elastic ATVA is implemented due to the proven effectiveness described in this chapter.

FIGURES FOR CHAPTER 4

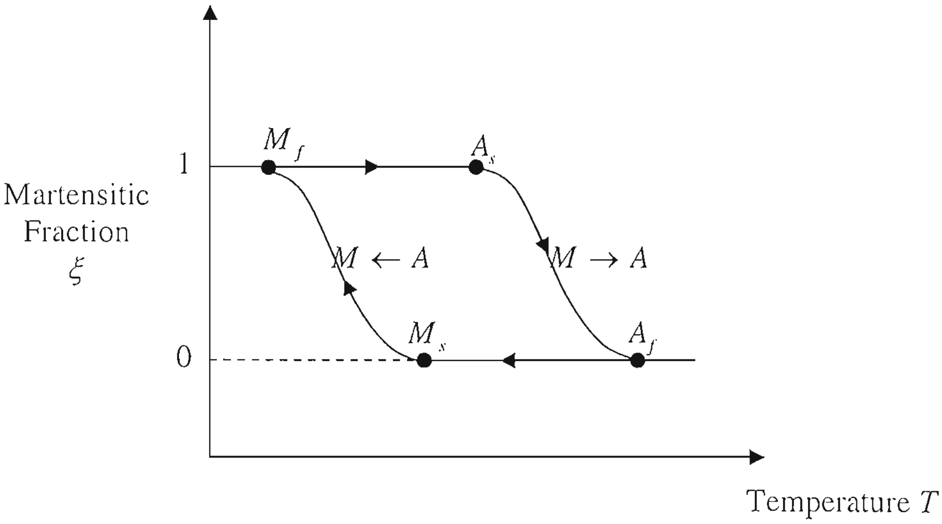

Figure 4.1. Martensitic fraction in SMA.

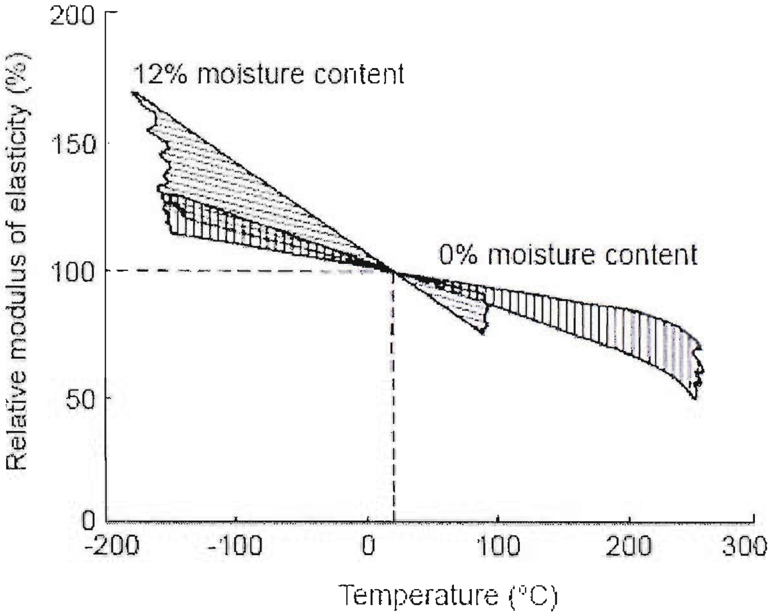

Figure 4.2. Effect of rapid temperature change on modulus of elasticity of wood at two moisture content levels relative to value at 20°C (Forest Product Laboratory [67]).

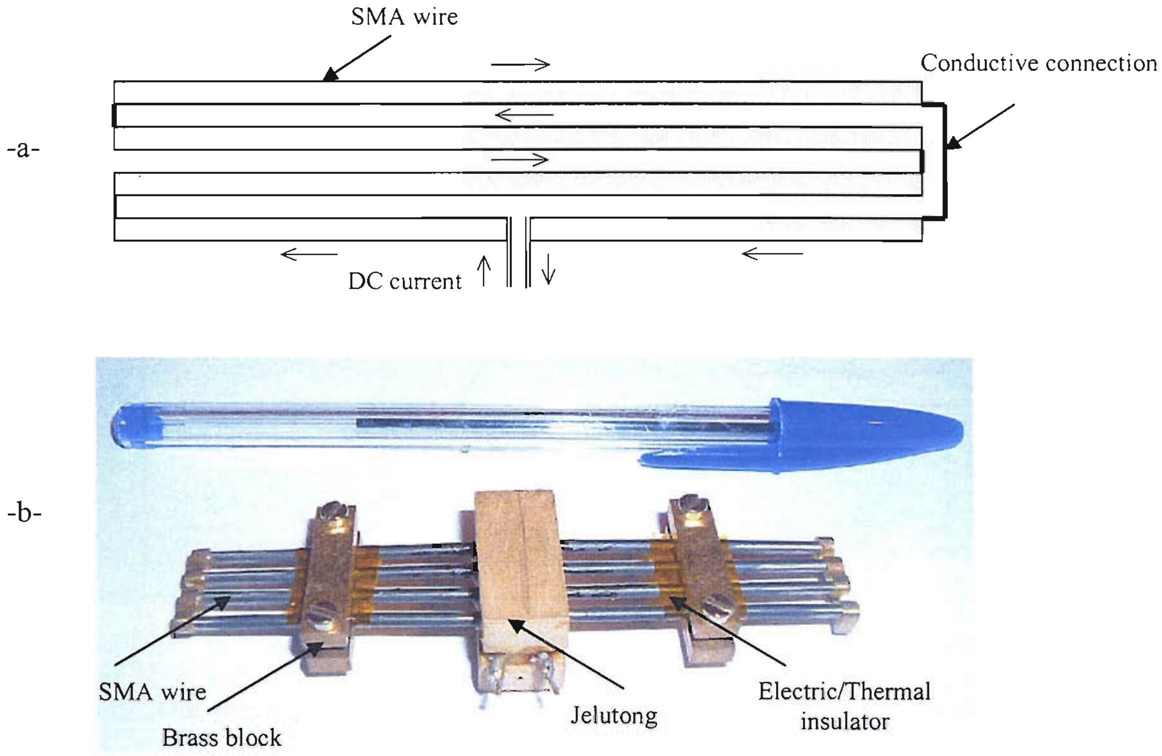

Figure 4.3. SMA ATVA: (a) sketch of the electric circuit; (b) The SMA ATVA.

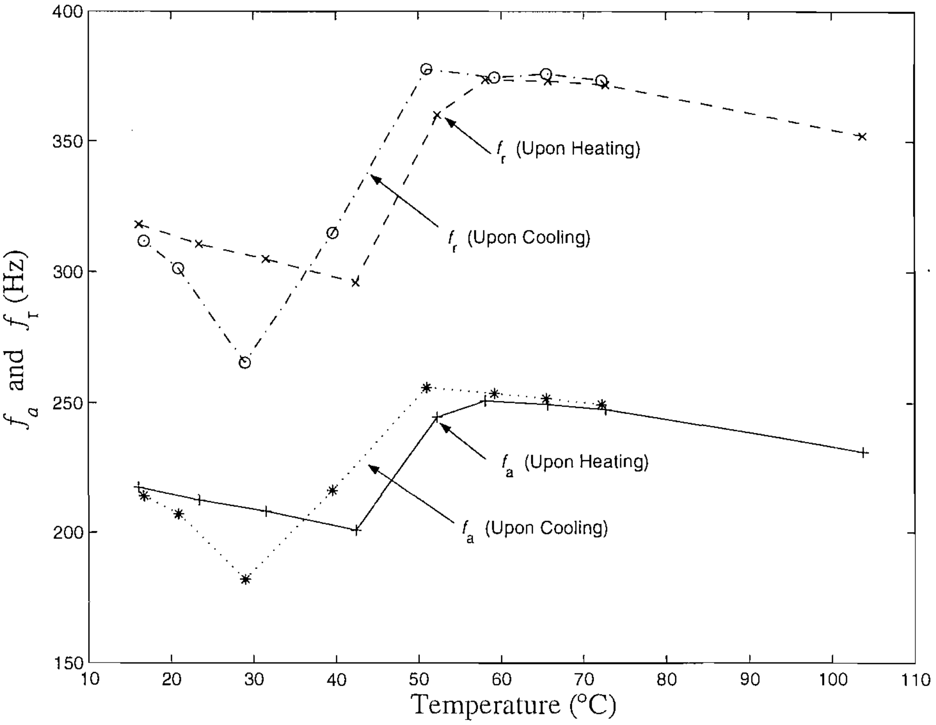

Figure 4.4. The variation of the absorber frequency f_a and the resonance frequency f_r of the SMA ATVA with temperature:
—— f_a upon heating;········f_a upon cooling;- - - - f_r upon heating;-·-·-f_r upon cooling

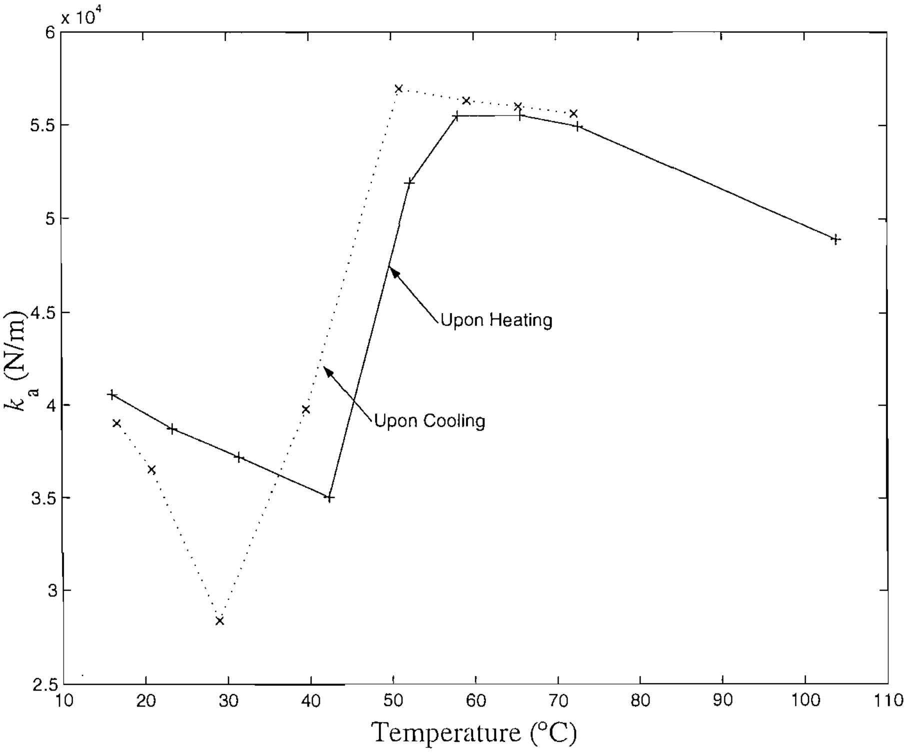

Figure 4.5. The variation of the SMA ATVA's stiffness with temperature upon heating-up (——) and cooling-down (··········).

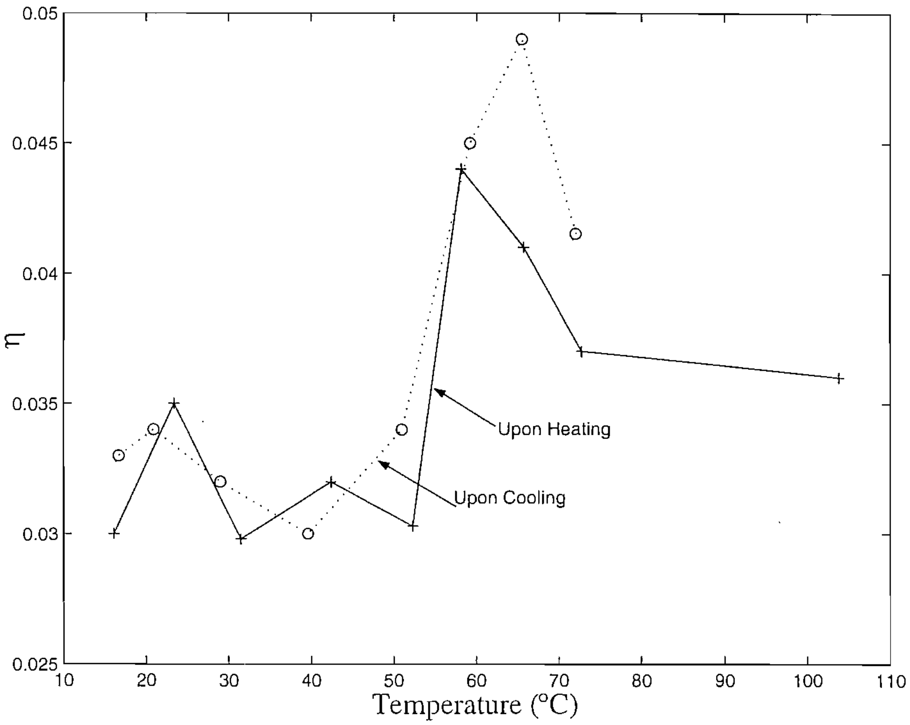

Figure 4.6. Effect of temperature on structural damping of SMA ATVA:
——— η upon heating; ········ η upon cooling.

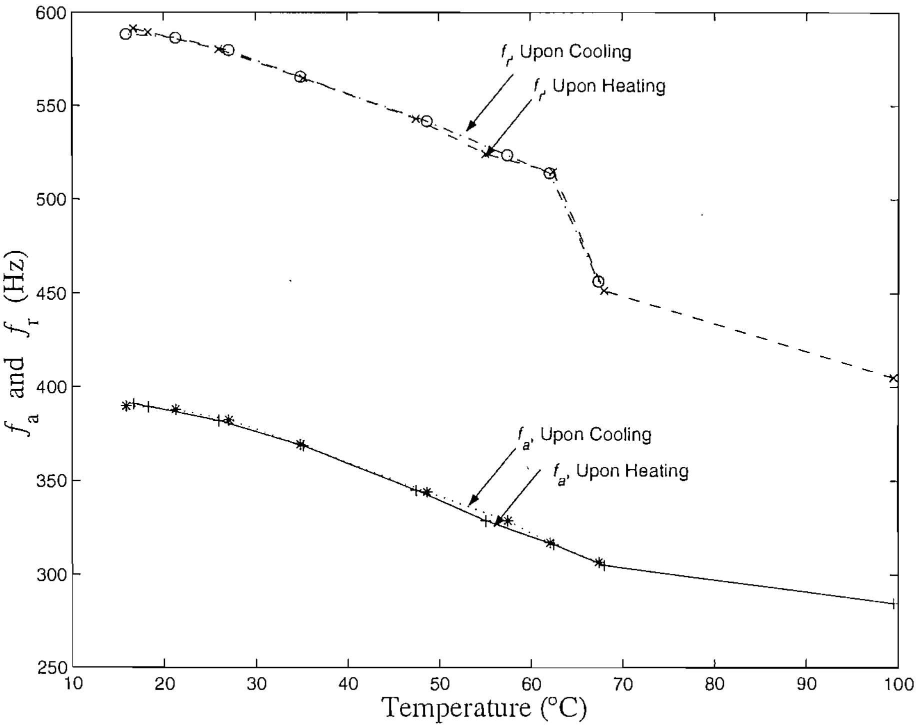

Figure 4.7. The variation of the absorber frequency f_a and the resonance frequency f_r of the thermo-elastic absorber with temperature:
——— f_a upon heating; ········ f_a upon cooling; - - - - - f_r upon heating; - · - · - f_r upon cooling

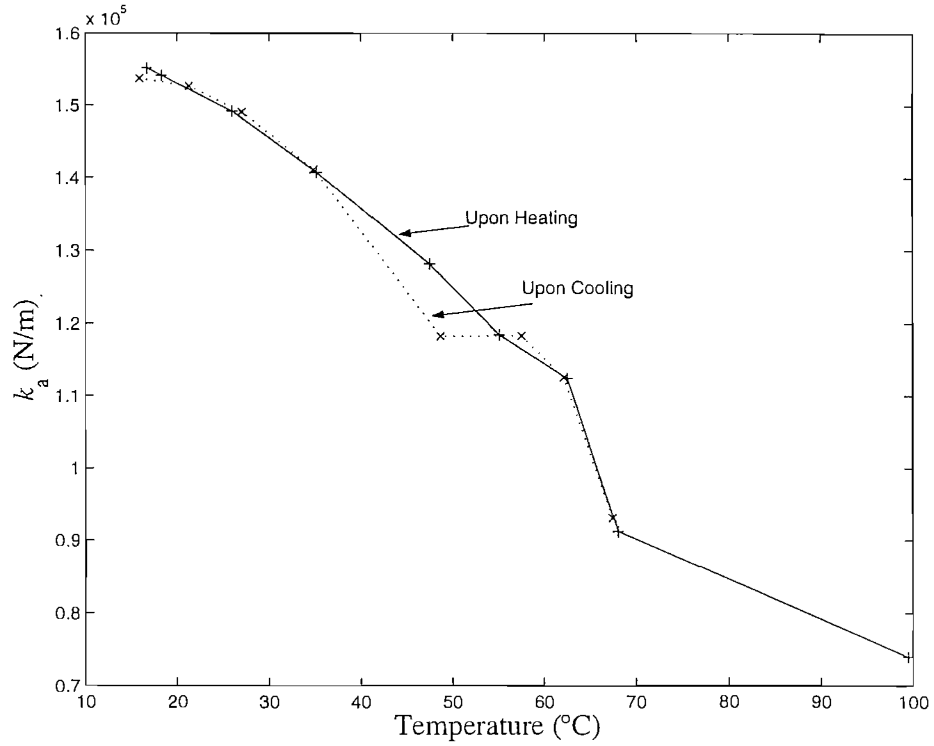

Figure 4.8. The variation of the thermo-elastic ATVA's stiffness with temperature upon heating-up (———) and cooling-down (·········).

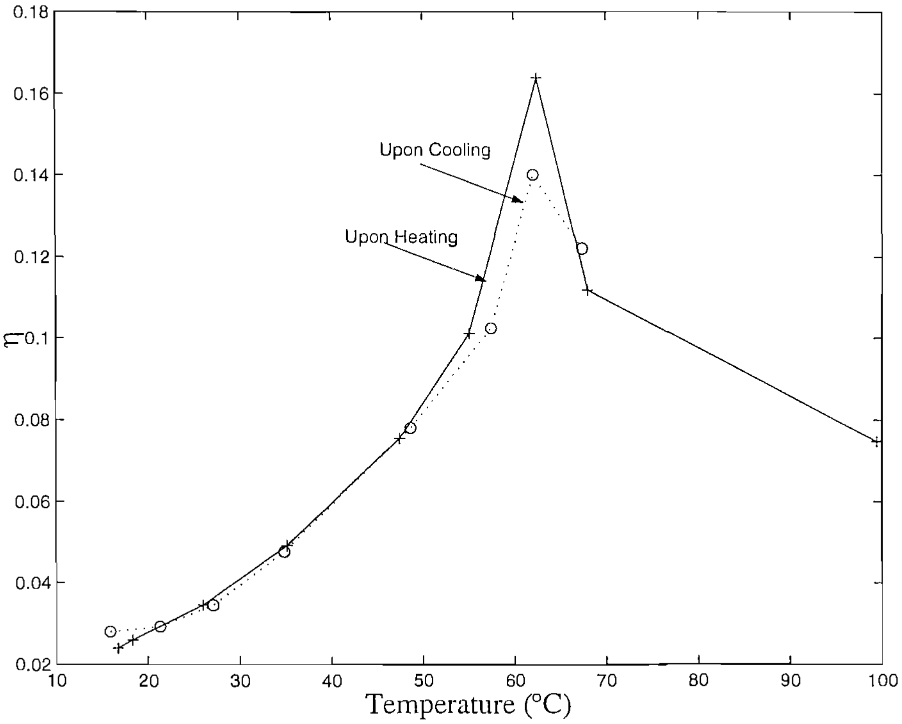

Figure 4.9. Effect of temperature on structural damping of thermo-elastic ATVA: ——— η upon heating; ········· η upon cooling.

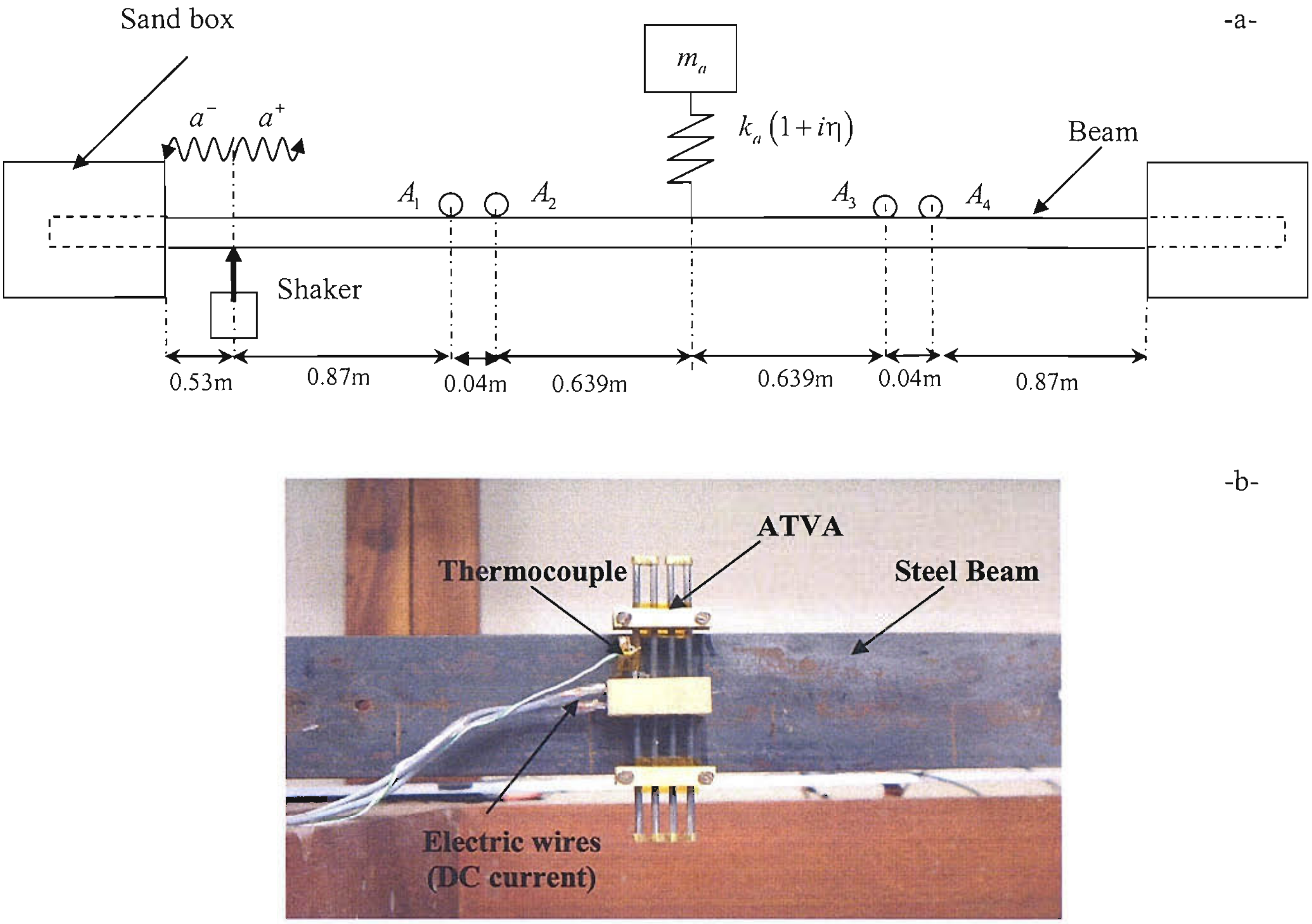

Figure 4.10. Experimental set-up: (a) sketch , ○ accelerometer; (b) actual system.

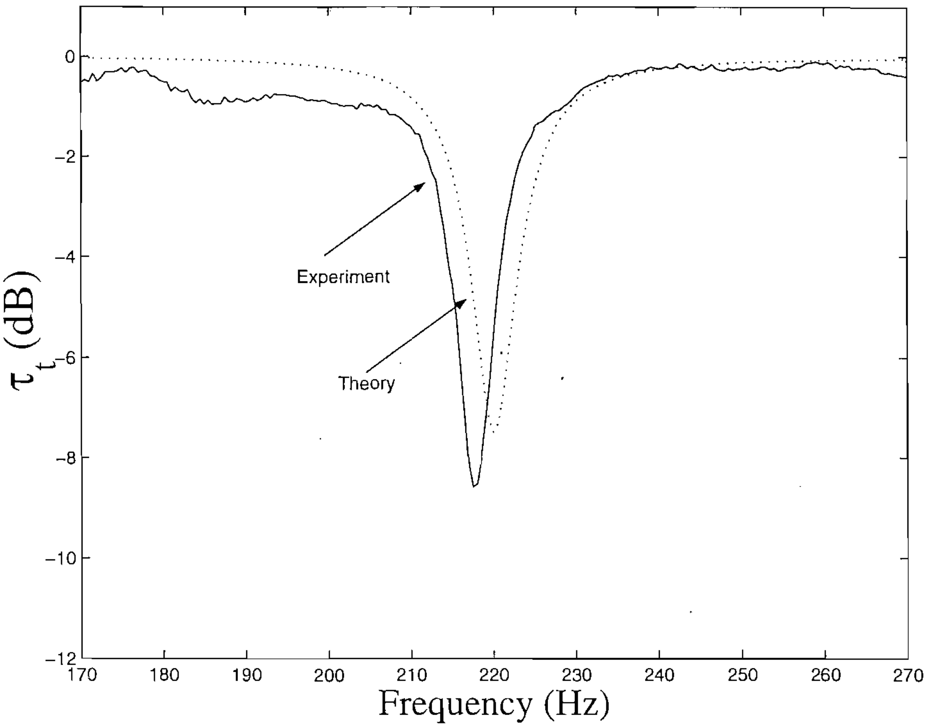

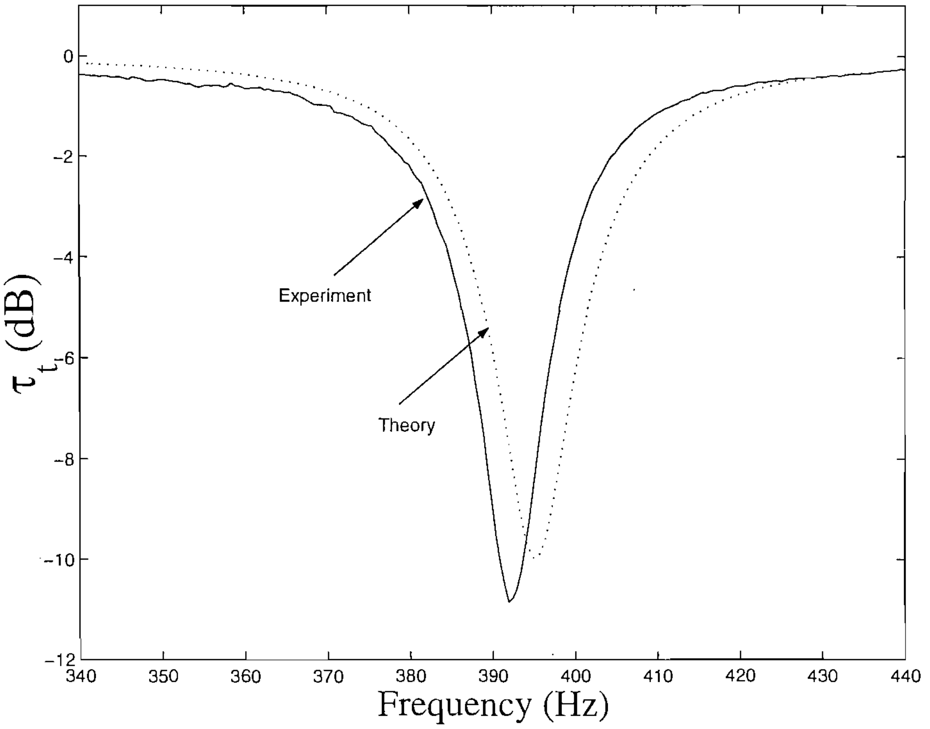

Figure 4.11. Transmission ratio using the ATVA at the ambient temperature: (a) SMA ATVA; (b) thermo-elastic ATVA.

——— τ_t, experiment; ········· τ_t, theory.

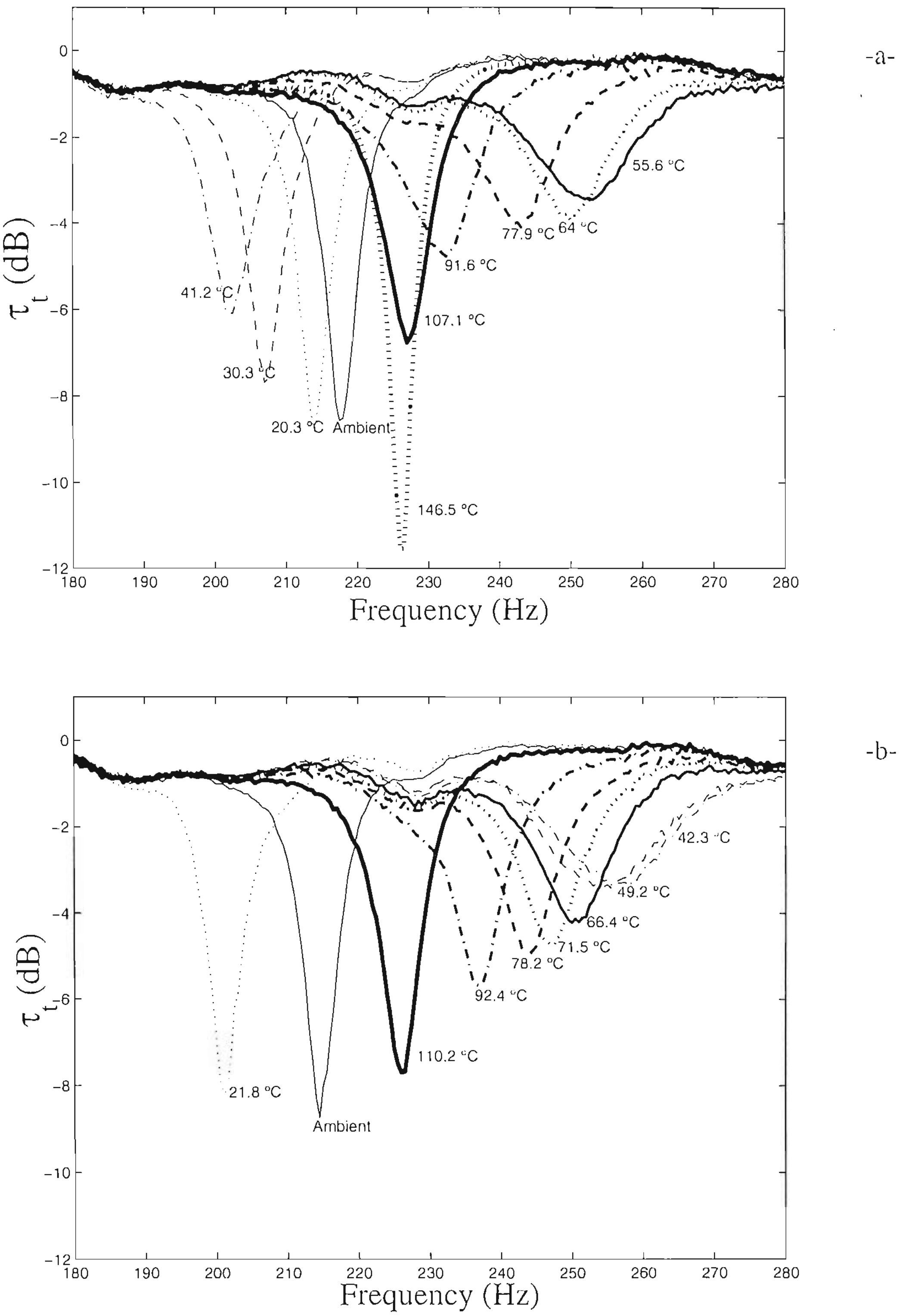

Figure 4.12. Transmission ratio for the SMA ATVA at various temperatures: (a) heating-up; (b) cooling-down.

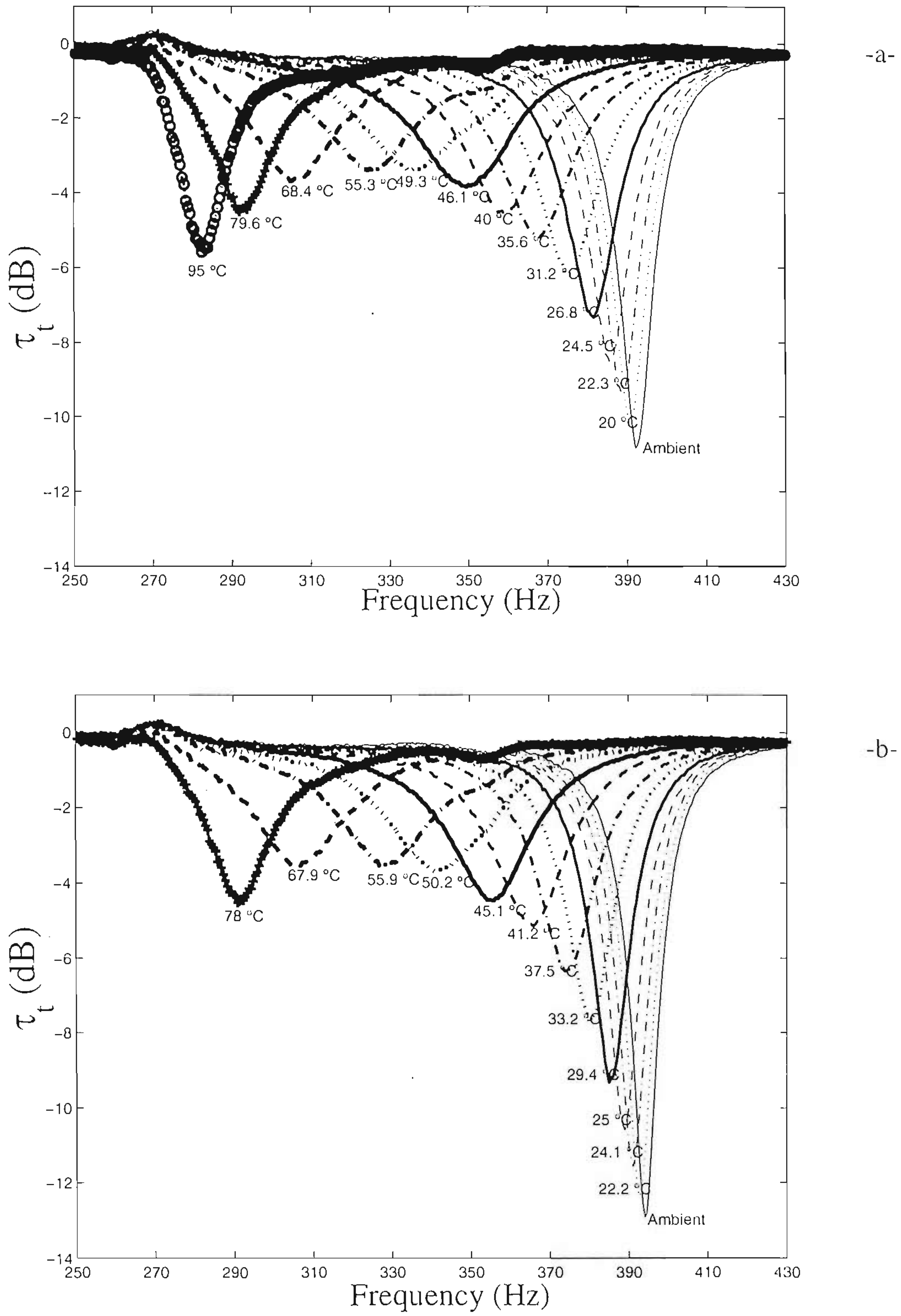

Figure 4.13. Transmission ratio for the thermo-elastic ATVA at various temperatures: (a) heating-up; (b) cooling down.

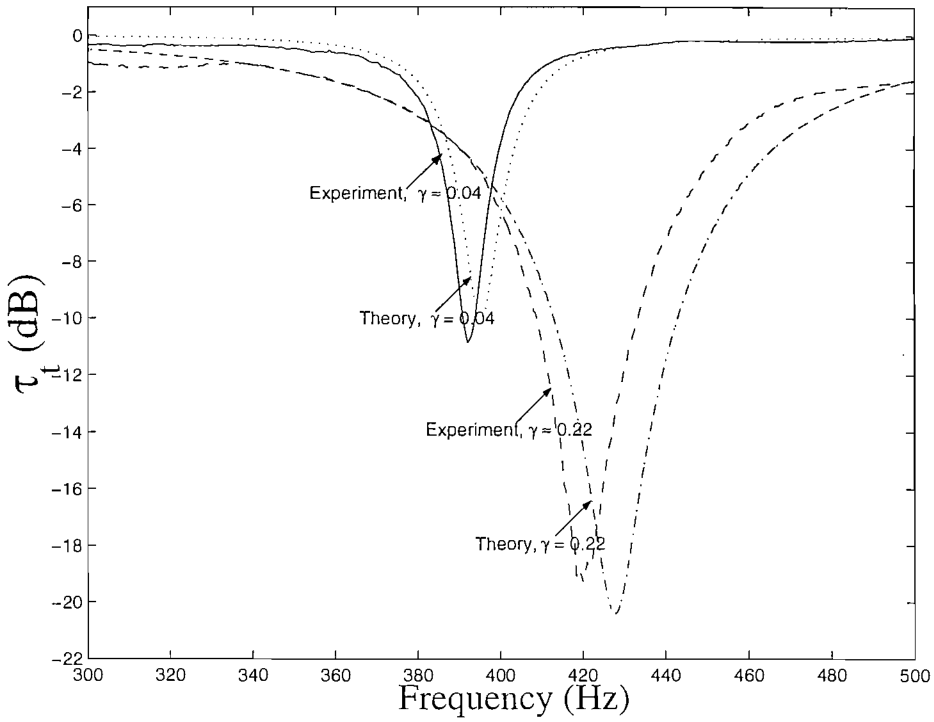

Figure 4.14. Transmission ratio for the thermo-elastic ATVA for two different values of γ:

smaller cross-sectional beam ($\gamma = 0.04$), ——— τ_t , theory; ………. τ_t , experiment.

bigger cross-sectional beam ($\gamma = 0.22$), -·-·-·- τ_t , theory; - - - - - τ_t , experiment.

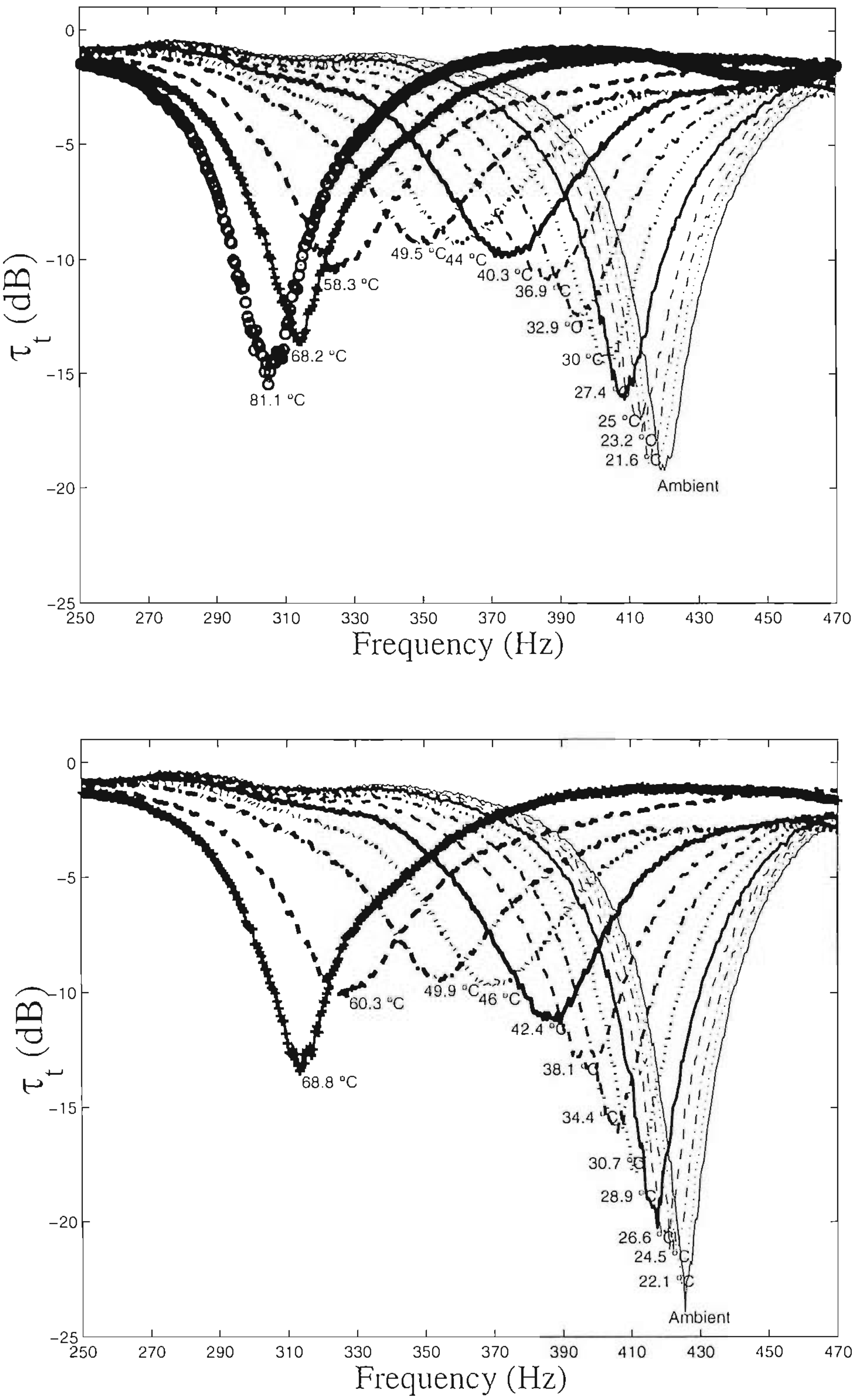

Figure 4.15. Transmission ratio for the thermo-elastic ATVA at various temperatures, $\gamma = 0.22$ at the ambient temperature: (a) heating-up; (b) cooling down.

Alloy Composition	Nickel (nominal)	54.5 wt.%
	Titanium	Balance
	Oxygen (max)	0.05 wt.%
	Carbon (max)	0.05 wt.%
Mechanical Properties	Ultimate Tensile Strength (UTS)	min. 1100 MPa
	Total Elongation	min. 10%
Physical Properties	Melting Point	1310°C
	Density ρ	6450 kg/m^3
	Electrical Resistivity ρ_e	760×10^{-9} Ωm
	Modulus of Elasticity E	$28 - 41 \times 10^3$ MPa
Shape Memory Properties	Shape Memory Strain (max)	8%
	Austenite Start Temperature	$A_s = 45°C$
	Austenite Finish Temperature	$A_f = 60°C$
	Martensite Start Temperature	$M_s = 50°C$
	Martensite Finish Temperature	$M_f = 35°C$

Table 4.1. Typical properties of Nitinol SM 495 wire.

Properties / Materials	Young's Modulus (MPa)	Density (kg/m^3)
Jelutong	10.04×10^3	450
Epoxy-resins Araldite 2011/A ($T_g \approx 40°C$)	21.6 (at room temperature), 1.62 (at 150°C)	1150

Table 4.2. Mechanical properties of the mounting materials.

Young's Modulus (GPa) E	101
Density (kg/m^3) ρ	8550
Electrical Resistivity (Ω.m) ρ_e	62×10^{-9}

Table 4.3. Physical properties of brass.

Young's Modulus (GPa) E	201
Density (kg/m^3) ρ	7970
Electrical Resistivity (Ω.m) ρ_e	760×10^{-9}

Table 4.4. Physical properties of stainless steel.

CHAPTER 5: CONTROL

5.1 Introduction

Chapter 4 described two variable stiffness adaptive tuned vibration absorbers. These were able to control the transmitted waves at various frequencies when tuned manually by adjusting the temperature of the absorbers via the use of an electric current.

The aim of this chapter is to discuss automatic online tuning of the absorber to adjust the absorber stiffness to keep the power transmitted downstream to a minimum in the face of a varying disturbance frequency. One optimisation method is considered in detail. This implements the gradient descent algorithm that utilises an error function which indicates optimum tuning when it is zero. The sign of the error function indicates the tuning direction when the absorber is not tuned, i.e. a positive (or negative) value indicates that the stiffness needs to be increased (or decreased).

This chapter is arranged in 5 sections as follows. Following the introduction, section 5.2 reviews some possible control strategies that would achieve a self-tuning control system. The rest of the chapter concerns the gradient descent approach. An analytical investigation for an appropriate error function is presented in section 5.3. This is employed in a gradient descent algorithm in section 5.4. Finally, the discussion and brief conclusions of this stage of the work are presented in section 5.5.

5.2 Control Strategies

The conventional procedures for control involve systems with fixed coefficients (constant parameters) and the design methods are based upon a linear, time-invariant assumption. In practical situations, system parameters often vary with time. Self-tuning control is one design philosophy for monitoring time variations and incorporating them into the design process. Therefore, a self-tuning controller is required to ensure that the variable stiffness absorber described in the previous chapter is continuously tuned to the disturbance frequency.

The basic idea of self-tuning systems is to construct an algorithm that will automatically change the parameters of the system to meet a specific condition. This is done by the addition of an adjustment mechanism to the standard feedback system as illustrated in Figure 5.1 [69, 70]. This mechanism monitors the system and adjusts the coefficients of the corresponding controller to maintain a required performance. For the ATVAs discussed in the previous chapter this involves changing the current in the variable stiffness elements towards the optimum value, hence changing the tuned frequency. Generally, the frequency range, within which the ATVA is active, is dependent upon the adaptive properties of the absorber material and the limitation introduced by the controller.

The fact that the TVA is optimally tuned when τ_t is minimum, can directly be employed as an objective function in a trial-error iteration process such as the "gradient search algorithm" [71]. This is an optimisation algorithm to find a minimum value of a function. The basic idea is to change one control variable while observing the effect on the objective function. If the new adjustment has decreased the objective function then the adjustment process is repeated in the same direction, while if the objective function has increased then the adjustment process is reversed to the opposite direction. The algorithm iterates until a minimum value of the objective function is reached [72]. In practice, for the ATVAs designed in the previous chapter, the current is changed slightly and the new value of τ_t estimated and compared to the previous value. If τ_t has decreased the current is changed in the same direction, while if τ_t has increased the current is changed in the other direction. The process is then repeated. However, the process would need to be repeated many times to find the tuning direction. This would cause a major problem due to the large thermal time constant associated with the ATVAs, where the response to changing the current is slow. In addition, the existence of any local minimum that occurs at frequencies near to the tuned frequency would not give the optimum result from the ATVA. Therefore, implementing this algorithm with the designed ATVAs would form an inefficient self-tuning system.

The problems associated with the determination of the direction of tuning can be avoided by utilising an error function that should be zero to realise optimum tuning. Furthermore, this error function is positive (or negative) if the system is overtuned (or undertuned) so that it indicates both the degree of mistune and the direction towards the optimum tuning. The gradient here points in the direction of a zero value and has different signs at the neighbouring points of the optimum value (i.e. zero). Following the gradient in iterated steps may achieve a precise tuning as it provides a direction scheme towards the optimal tuning. This error function can be employed in a feedback control algorithm such as the gradient decent algorithm, the fuzzy control and the proportional-integral-derivative (PID) control [73]. The implementation of the error function in one of these algorithms would avoid the problems of slow convergence at local minimums, which might exist at frequencies near the tuned frequency (i.e. avoiding the problems associated with the gradient search algorithm).

An alternative method to self-tuning control systems can be the use of the look-up table (gain scheduling) method [69, 74]; this can achieve a simple automatic system. The method maps an input to an output using interpolation of stored values. A series of preliminary tests should be carried on a specific ATVA attached to a specific beam structure prior to applying the control system. The results of the test are stored in two vectors. The input vector represents the measured tonal excitation frequencies while the output vector represents the corresponding control decisions i.e. current, which actuates the ATVA to reach the optimum stiffness. If the measured input does not match any element in the stored input vector, the system interpolates between the two appropriate elements of the table to determine an output value. However, if the measured input is less than the first or greater than the last input vector element, an extrapolation takes place using the first two or the last two points. This method is limited to a particular ATVA/beam system and requires a large number of experimental tests to acquire the data necessary to give an accurate control decision. Otherwise, only a rough tuning is satisfied.

Only one algorithm will be implemented in this project. This is the gradient descent algorithm for the advantages described above.

5.3 Error Functions

Three possible error functions are described in this section. The performance of these error functions in indicating the optimum tuning is investigated. The most effective one will be implemented in the gradient descent algorithm introduced in the next section.

5.3.1 Phase between motions of absorber and primary system

The first suggested error function e_1 is the phase between motions of absorber and primary system. This has been used for tuning a vibration absorber mounted on a primary system and it was implemented in the past in many applications [12, 18, 20, 22, 75-77]. For an undamped absorber, the optimum tuning is satisfied when the relative phase between the absorber vibration and the primary system vibration (ϕ_1) is $90°$. This suggestion provides direction and quality of tuning by utilising $e_1 = \cos\phi_1$ as an error function, where $\cos\phi_1 = 0$ when the ATVA is tuned. The optimum tuning condition for this system corresponds to exact matching between the absorber's frequency and the excitation frequency ($\Omega_t = 1$). Thus for an absorber tuned to a frequency $\Omega > 1$, the two masses respond in phase such that e_1 is positive. In contrast for an absorber tuned to a frequency $\Omega < 1$, the two masses respond out of phase such that e_1 is negative.

The existence of damping in the absorber means that this error function does not give the exact indication for the optimal tuning. The differences are small, unless the damping is large. A detailed investigation of the effect of damping on the performance of e_1 as an exact indicator is given in Williams *et al* [61].

The error function e_1 does not indicate proper tuning for controlling the power transmission in beam structures. The reason is that the tuning condition of an absorber attached to a beam structure at $l/\lambda_a \neq 0$ is different as discussed in Chapter 3; i.e. $\Omega_t \neq 1$. Therefore, an alternative function is required to indicate the tuning of the

TVA. This can be found by exploring the optimum phase difference between any two reference motions that indicates the status of the TVA when tuned.

5.3.2 Phase between velocity and angular acceleration at the absorber location on a beam

Consider an undamped absorber ($\eta = 0$) attached to an infinite beam ($c^- = 0$) as shown in Figure 3.1. Assuming the absorber is mounted in the farfield of the point disturbance ($b_N^+ = 0$), the displacement of the beam w in the downstream region $x \geq 0$ is therefore given by

$$w(x,t) = b^+ \left(te^{-ikx} + t_N e^{-kx}\right)e^{i\omega t}. \tag{5.1}$$

The transmission coefficients t and t_N of the propagating and the evanescent waves respectively are discussed in Chapter 3 and are given by

$$\begin{aligned} t &= \frac{\Omega^2 - \left(1 + \gamma\Omega^{1/2}\right)}{\Omega^2 - \left(1 + \gamma\Omega^{1/2}(1+i)\right)} \\ t_N &= \frac{\gamma\Omega^{1/2}}{\Omega^2 - \left(1 + \gamma\Omega^{1/2}(1+i)\right)} \end{aligned}. \tag{5.2}$$

Both transmission coefficients share a common denominator $d_c = \Omega^2 - \left(1 + \gamma\Omega^{1/2}(1+i)\right)$. Therefore, equation (5.1) can be rewritten, such that

$$w(x,t) = \alpha\left(Te^{-ikx} + T_N e^{-kx}\right)e^{i\omega t}, \tag{5.3}$$

where $T = \Omega^2 - \gamma\Omega^{1/2} - 1$ and $T_N = \gamma\Omega^{1/2}$ are the numerators of t and t_N respectively, and $\alpha = b^+ / d_c$. Figure 5.2 shows the feasibility of instigating a direction scheme to tune an ATVA for various mass ratios γ. It is shown that $T = 0$ at the tuned frequency ratio Ω_t for each γ, and has a different sign if either the absorber is over-tuned $\Omega < \Omega_t$ (negative value) or under-tuned $\Omega > \Omega_t$ (positive value).

From equation (5.3) the angular displacement $w' = \partial w / \partial x$ and translational acceleration $\ddot{w} = \partial^2 w / \partial t^2$ at $x = 0$ are found to be

$$w'(0,t) = -\alpha k \left(iT + T_N\right) e^{i\omega t}; \quad \ddot{w}(0,t) = -\alpha\omega^2 \left(T + T_N\right) e^{i\omega t}. \tag{5.4}$$

Plotting w' and $\ddot{w}$ in the complex plane shows that the TVA is optimally tuned ($T = 0$) when both signals are in phase ($\theta = 0°$) as illustrated in Figure 5.3. Taking the cosine of the phase between w' and $\ddot{w}$, $\cos\theta$, as the error function would not present an appropriate direction for the optimum tuning since $\cos\theta = 1$ when the ATVA is optimally tuned. Furthermore, in practical situations, i.e. accelerometers are used, w' and $\ddot{w}$ requires to apply a number of mathematical manipulations to the measured signals (accelerations). A solution can be obtained by taking the error function $e_2 = \cos\phi_2$, where ϕ_2 is the phase between the velocity $\dot{w}$ and the angular acceleration $\ddot{w}'$ in $\cos\phi_2$ instead. This phase angle equals $90°$ when the ATVA is optimally tuned, hence the error function e_2 would have a different sign if the ATVA is over- or under-tuned. Table 5.1 includes a list of other possible reference signals that gives a $90°$ phase shift when the ATVA is optimally tuned.

The error function e_2 can be calculated numerically by time averaging the product of the two reference signals

$$\overline{\dot{w}\ddot{w}'} = \frac{1}{2}\left|\dot{W}\right|\left|\ddot{W}'\right|\cos\phi_2, \tag{5.5}$$

where $\dot{W}$ and $\ddot{W}'$ represent the amplitudes of the velocity and the angular acceleration respectively while $\overline{\dot{w}\ddot{w}'}$ is the time average of $\dot{w}$ and $\ddot{w}'$. Therefore, the error function can be represented by

$$e_2 = \cos\phi_2 = \frac{2\,\overline{\dot{w}\ddot{w}'}}{|\dot{W}||\ddot{W}'|}. \tag{5.6}$$

This solution is independent of the amplitudes of motion, and it only presents the optimum tuning ($\phi_2 = 90°$) if $\eta = 0$.

The effect of damping on the performance of the error function is investigated numerically and the result is shown in Figure 5.4. If there is no damping, then $\cos\phi_2 = 0$ when the TVA is properly tuned. For $\gamma = 0.2$, this occurs when $\Omega_t \approx 1.1$. The effectiveness of e_2 in the region $\Omega < \Omega_t$ is limited to a certain frequency range as the beam is pinned ($\dot{w} = 0$) when $\Omega = 1$ and a 180° phase shift occurs. As a consequence, e_2 turns from negative to positive at this specific frequency ratio. For a small amount of damping (e.g. $\eta = 0.01$) the error function approximates the ideal. However, the frequency range in which $e_2 < 0$ becomes smaller as damping increases since $e_2 = 0$ at $\Omega < \Omega_t$, and the phase shift occurs at $\Omega > 1$. Furthermore, for large enough damping (e.g. $\eta = 0.1$) e_2 is always positive. Consequently, the error function will no longer be an exact indicator of optimal tuning if a high level of damping exists in the TVA. This can be related to the significant effect of damping on the attenuation of the power transmitted. Thus $\phi_2 \neq 90°$ when the absorber is optimally tuned.

Figure 5.5 shows the variation of e_2 with Ω when $\eta = 0$ for various mass ratios γ. For any given γ, the frequency ratio $\Omega > \Omega_t$ gives a positive value for e_2. On the other hand, for the frequency range $1 < \Omega < \Omega_t$, e_2 has a negative value. Increasing the mass ratio increases Ω_t, and this in turn increases the effectiveness of e_2 in the frequency range $1 < \Omega < \Omega_t$. Note that the frequency range in which e_2 indicates the direction of mistune accurately is for $\Omega > 1$, and that range can be quite narrow if γ is small.

5.3.3 The two-sensor approach

It has been seen that even a small level of damping significantly reduces the effectiveness of the error function e_2. Therefore, a third error function e_3 is required.

Consider an absorber attached to a beam at $x = 0$, with a general impedance $\bar{Z}$. The reflection and transmission coefficients are found in Chapter 2 to be $t = 1 + i\mu$, $r = i\mu$ and $t_N = r_N = \mu$, where $\mu = Z/(4 - Z(1+i))$ represents the effect of the translational constraint and where $Z = i\bar{Z}\omega / EIk^3$ is the dimensionless impedance. Consequently, the outputs of two sensors (e.g. accelerometers) A_1 and A_2 attached at a distance Δ from each side of the point discontinuity (see Figure 5.6) are given by

$$\begin{aligned} A_1 &= b^+\left(e^{ik\Delta} + i\mu e^{-ik\Delta} + \mu e^{-k\Delta}\right) \\ A_2 &= b^+\left((1+i\mu)e^{-ik\Delta} + \mu e^{-k\Delta}\right) \end{aligned}. \tag{5.7}$$

Evaluating A_1 and A_2, for a distances $\Delta = \lambda_a/4 = \pi/2k$, gives

$$\begin{aligned} A_1 &= b^+\left(i + \mu + \mu e^{-\pi/2}\right) \\ A_2 &= b^+\left(\mu - i + \mu e^{-\pi/2}\right) \end{aligned}. \tag{5.8}$$

Performing the sum and difference of these signals and integrating the former gives two signals

$$s_1 = \frac{A_1 + A_2}{2i\omega}; \quad s_2 = \frac{A_2 - A_1}{2\Delta}. \tag{5.9}$$

Substituting equation (5.8) into equation (5.9) yields

$$s_1 = \frac{2\mu\left(1+e^{-\pi/2}\right)}{2i\omega} b^+ ;\ s_2 = \frac{-2i}{\pi} b^+ , \tag{5.10}$$

therefore, the ratio of s_2 to s_1 is given by

$$\frac{s_2}{s_1} = \frac{2\omega}{\mu\left(1+e^{-\pi/2}\right)} . \tag{5.11}$$

It is clear that the phase between s_1 and s_2 is only dependent on the phase of μ. Since the absorber is optimally tuned when $t = 0$ so that $\mu = -i$ then μ has a phase $\phi_3 = -90°$. Thus s_1 and s_2 are in quadrature and their product can be utilised as an error function.

The third error function e_3 is thus taken to be the cosine of the phase between s_1 and s_2 when they are obtained using two sensors located at a distance $k\Delta = \pi\kappa_o / 2$ from each side of the absorber. κ_o is an odd integer. The error function e_3 can then be estimated by

$$e_3 = \left. \frac{2\,\overline{s_1 s_2}}{\left|S_1\right|\left|S_2\right|} \right|_{k\Delta = \frac{\pi\kappa_o}{2}} . \tag{5.12}$$

where S_1 and S_2 represent the amplitudes of the signals while $\overline{s_1 s_2}$ is the time average of their product.

Figure 5.7 shows the variation of e_3 with the normalised spacing (Δ / λ_a) at $\Omega_t \approx 1.1$ for various η. When $\eta = 0$, the error function $e_3 = 0$ for all Δ / λ_a. However, for $\eta \neq 0$ then $e_3 = 0$ only at certain points which are close to $\Delta / \lambda_a \approx 0.25\kappa_o$. These are called the optimum spacings Δ_{opt}. On the other hand, at spacings approximately $\Delta / \lambda_a \approx 0.5\kappa_e$, where κ_e is an even integer, the phase angle between s_1 and s_2

changes by $180°$. These spacings are defined as the critical spacings Δ_c. Moreover, for each Δ_{opt} / λ_a, e_3 is positive when $\Delta / \lambda_a < \Delta_{opt} / \lambda_a$, while it is negative when $\Delta / \lambda_a > \Delta_{opt} / \lambda_a$. Note that $e_3 = 0$ when $\Delta = \Delta_{opt}$ irrespective of the level of damping: thus, if the sensors are optimally positioned and the absorber is optimally tuned, $e_3 = 0$, independent of the level of damping.

Figure 5.8 shows the variation of e_3 as a function of Ω for the sensors located at two different spacings and for various η. Generally, for $\Delta / \lambda_a \approx 0.25$, $e_3 = 0$ at $\Omega = \Omega_t$ for all η as shown in Figure 5.8a. Furthermore, e_3 is positive for $\Omega > \Omega_t$ and negative for $\Omega < \Omega_t$. However, it was found that, the spacing which is optimum at Ω_t becomes critical Δ_c / λ_a at two other frequencies limiting the effectiveness of e_3 as shown in Figure 5.8a to between about $\Omega = 0.7$ and $\Omega = 1.6$. Nevertheless, the range of frequencies within which e_3 is effective is very much greater than the range for e_2 (see Figure 5.4) and the cost function is very much less sensitive to damping (i.e. for $\eta = 0.1$, e_3 is still an accurate indicator of mistune operative over a reasonably wide frequency range). For the sensors attached at $\Delta / \lambda_a \neq \Delta_{opt} / \lambda_a$, e.g. $\Delta / \lambda_a \approx 0.15$, then $e_3 > 0$ at Ω_t for $\eta = 0.1$ (i.e. the error function becomes more sensitive to damping) as shown in Figure 5.8b. In addition, the frequency range within which e_3 accurately indicates mistune is smaller than that when $\Delta / \lambda_a \approx 0.25$.

5.4 Control Using the Gradient Descent Algorithm

This section discusses the application of the gradient descent algorithm in a self-tuning control system to maintain the optimum tuning of the variable stiffness ATVA in the face of a disturbance of varying frequency. This involves the use of the error function e_3, which indicates optimum tuning when it is zero. A flow chart of the control strategy is introduced. The performance of the gradient descent algorithm and the error function is investigated numerically when the disturbance is tonal. The ATVA dynamics are not considered, with the simulations assuming that the ATVA stiffness can be controlled directly.

5.4.1 Gradient descent algorithm

This is an optimisation method that approaches the location of the zero of a function by taking steps proportional to the gradient of that function at the current point. The gradient here points in the direction of a zero value and has different signs at the neighbouring points of the optimum value (i.e. $e_3 = 0$).

The gradient descent algorithm can be employed for the self-tuning control system, such that the algorithm utilises e_3. This can be represented as follows. At the *n*th time step, the ATVA's stiffness is changed according to the estimate of the error function at the *n*th time step $e_{3,n}$ so that

$$k_{a,n} = k_{a,n-1} + Pe_{3,n}, \tag{5.13}$$

where $Pe_{3,n}$ is the update in the parameter. Here only a linear update is considered so that P is some constant. Therefore, when $e_{3,n} \neq 0$, the controller will be active, and continues to update the stiffness of the ATVA until $e_{3,n} = 0$. The sign of the error function will guide the controller in the optimum direction.

In order to illustrate the control mechanism, the variation of $e_{3,n}$ with the ATVA stiffness k_a is considered. When the frequency ratio is less than the tuned value ($\Omega < \Omega_t$), the sign of $e_{3,n}$ will be negative and the controller will need to decrease the stiffness of the ATVA to reach the optimum value. On the contrary, when $\Omega > \Omega_t$, the sign of $e_{3,n}$ will be positive and the controller will need to increase the stiffness of the ATVA (see Figure 5.9).

5.4.2 Flow chart of the control strategy

A flow chart of the control strategy is shown in Figure 5.10. At the *n*th time step, the measured signals of the two sensors (i.e. accelerometers), located at $k\Delta = \pi\kappa_a / 2$ from each side of the ATVA, are mathematically processed to obtain s_1 and s_2. The error function $e_{3,n}$ is then calculated and a proportional control action is taken when $e_{3,n} \neq 0$ to change the stiffness of the ATVA in the direction towards the optimum tuning.

A control system other than the linear proportional method utilised in this thesis can also be used to give a different response and maybe a better performance.

5.4.3 Numerical simulations

In this section simulations of a self-tuning control system applied to a variable stiffness ATVA mounted on a beam are described. This is achieved by solving the mathematical model of the ATVA/beam system described previously assuming quasi-steady state and time harmonic behaviour. The dynamics of the ATVA are not considered in the numerical simulations where the response of the modelled ATVA is instant (i.e. In practice, the electric current input to the ATVA is changed which in turn changes the stiffness). The system is run over a number of time steps. The frequency of the tonal disturbance may change and the response of the control system, in tuning the ATVA, is monitored. This was achieved using Simulink and Matlab toolboxes ©, which enable block diagrams to represent the mathematical model of the system and the control algorithms to be built. In general, Simulink simulates a dynamic system by computing its state at successive time steps over a specified time span using information provided by the model [74].

Generally, the system including the controller is considered to be in the quasi-steady state, where the excitation frequency is discrete, the response at that frequency is in the steady state and the controller retunes the system at a rate that is slow compared to the excitation frequency.

At the outset, a Simulink model of an incident wave propagating on an infinite thin beam with a variable stiffness ATVA mounted as a discontinuity at $x = 0$ is designed. The Simulink model is shown in Appendix 5. The data provided for the numerical simulations are for the thermo-elastic ATVA attached to the thin steel beam and they are tabulated in Table 5.2. The disturbance is modelled by a sinusoidal wave block. This generates an incident wave at a frequency f which can change with time. Both the incident wave amplitude and the value of the excitation frequency at each time step are input to a block (ATVA/Beam) that represents the ATVA attached to the beam described in Chapter 4. The disturbance frequency is input to a block to calculate the frequency ratio Ω. The damping ratio η and the initial value of the mass ratio γ are also found numerically in this block using the data of the absorber and the beam. These values are stored in other subsystem blocks. The calculated parameters are then used to find the reflection and transmission coefficients as discussed in Chapter 3. These coefficients are then multiplied with the amplitude of the incident sinusoidal wave, to produce numerical values for the transmitted and reflected waves, including the evanescent components. The phase change $\Delta\Phi = k\Delta$ experienced by a wave as it propagates over a distance Δ is then included by time delaying the wave by an amount $\Delta t = \Delta\Phi / \omega$. The evanescent waves are represented by multiplying the wave amplitudes influenced by the nearfield reflection and transmission coefficients with an exponential term $e^{-k\Delta}$. The motion of the beam due to the propagating and nearfield waves at points Δ on either side of the ATVA can then be calculated to simulate the signals A_1 and A_2. These signals are then input to another block (Signal manipulation) to find the reference signals s_1 and s_2 using equation (5.9). These signals are input to another block (Control system) to estimate $e_{3,n}$ which is evaluated using equation (5.12).

Hence, the error function $e_{3,n}$ can be estimated numerically at the *n*th time step. A similar control system was previously developed by Rustighi *et al* [12] to tune an ATVA attached to a primary structure.

The motion at three points on the beam (A_1, A_2 and A_3) caused by the transmitted and the reflected waves are estimated. The points are illustrated in Figure 5.6: distances Δ upstream and downstream of the ATVA and in the downstream farfield. The latter is used to monitor the effectiveness of the control.

The performance of both the gradient descent algorithm and the error function is investigated by running the Simulink model, shown in Appendix 5, for 500 time steps. The disturbance frequency f is varied over fixed periods of the simulation steps as shown in Figure 5.11. The controller was set to update at each step, with $P = 1.5\times 10^3$. At the start of the simulation $f = 420$ Hz, the initial stiffness was chosen to be close to optimal, hence $\tau_t \approx 0$ and $e_{3,n} \approx 0$. The frequency dropped to 380 Hz ($\Omega < \Omega_t$), for the simulation steps between 100 and 250 steps. The estimated cost function $e_{3,n} < 0$ and the controller decision was to decrease the stiffness, hence reducing the absorber frequency and bringing τ_t to a minimum. A smaller drop in excitation frequency to $f = 360$ Hz took place for simulation steps between 250 and 350 steps, therefore the number of steps taken for the ATVA to adapt was less than the number taken in the previous excitation period. The performance of $e_{3,n}$ in guiding the controller towards the optimum stiffness was validated by increasing the frequency to $f = 400$ Hz for the last period of the simulation steps (350 and 500 steps). The stiffness of the ATVA increases to bring τ_t to a minimum.

The effect of the controller on the beam motions A_1, A_2 and A_3, predicted at the three points discussed previously, for $\eta = 0$ is shown in Figure 5.12a. For the first 100 steps $f = 420$ Hz, then the disturbance frequency decreases to 380 Hz. In the first period of the simulation, the ATVA is tuned. The upstream nearfield acceleration A_1 was large due to the fact that the incident wave is reflected with $|r| = 1$, together with the small effect of the nearfield wave at that point. In addition, the downstream nearfield acceleration A_2 is not totally suppressed, because of the small effect of the transmitted nearfield wave. However, the downstream farfield acceleration $A_3 \approx 0$, as the nearfield waves are insignificant in the farfield. There is noticeable transmission for those time steps during which the ATVA is self-tuning. For the same reason A_1 is somewhat smaller during this time period as the ATVA adapts to the optimum stiffness of the new disturbance frequency. In contrast, A_2 and A_3 increase abruptly (see Figures 5.12b and c), then decrease gradually until $A_3 \approx 0$.

For a damped ATVA ($\eta = 0.05$), the effect of the controller on the beam motion is illustrated in Figure 5.13. The excitation is the same as that applied for the example above. Not all of the incident wave is reflected back to the upstream when the ATVA is optimally tuned in this situation. Some of the power is absorbed by the ATVA, and some is transmitted downstream as shown in Figures 5.13a-c.

5.5 Discussion and Conclusions

In this chapter, methods for a self-tuning control system that optimally tunes the adaptive vibration absorber were introduced. These were designed to control the transmitted power along a beam structure at various tonal frequencies. Only one control strategy was investigated in detail.

One algorithm was proposed for varying the absorber stiffness; the gradient descent algorithm. This algorithm employs an error function that should be zero to realise optimum tuning. Furthermore, the error function indicates both the degree of mistune and the direction towards the optimum tuning. Three error functions were considered. The first one has been used previously to tune an ATVA attached to a vibrating host structure. This error function represents the cosine of the phase difference between the motions of the ATVA and the primary structure. The tuning condition for this error function is different than the optimum tuning for an ATVA to control power transmission in a beam. The second error function gives an exact indication of the optimal tuning. This equals the cosine of the phase between the velocity and the angular acceleration at the position where the ATVA is attached to the beam (other possible reference signals were also listed). However it was found to be very sensitive to damping. In addition, it is only effective over a limited range of frequencies. The third error function does not suffer from these disadvantages. It is found by locating two accelerometers at half a wave length apart; one at each side of the ATVA. Their outputs are summed and differenced, with one time integration of the former. The phase between these two signals is 90° when the ATVA is tuned.

Numerical simulations illustrated the effectiveness of the control algorithm and the error function in varying the stiffness of an ATVA towards the optimum value.

Increasing the value of the proportional constant would reduce the time taken to reach the optimal value. However, this could only achieve rough tuning. Control systems other than the proportional method can also be used to enhance the performance of the self-tuning system.

The next chapter discusses the experimental validation of the error function discussed in this chapter and the experimental implementation of the gradient descent algorithm in a self-tuning control system that integrates the thermo-elastic ATVA.

FIGURES FOR CHAPTER 5

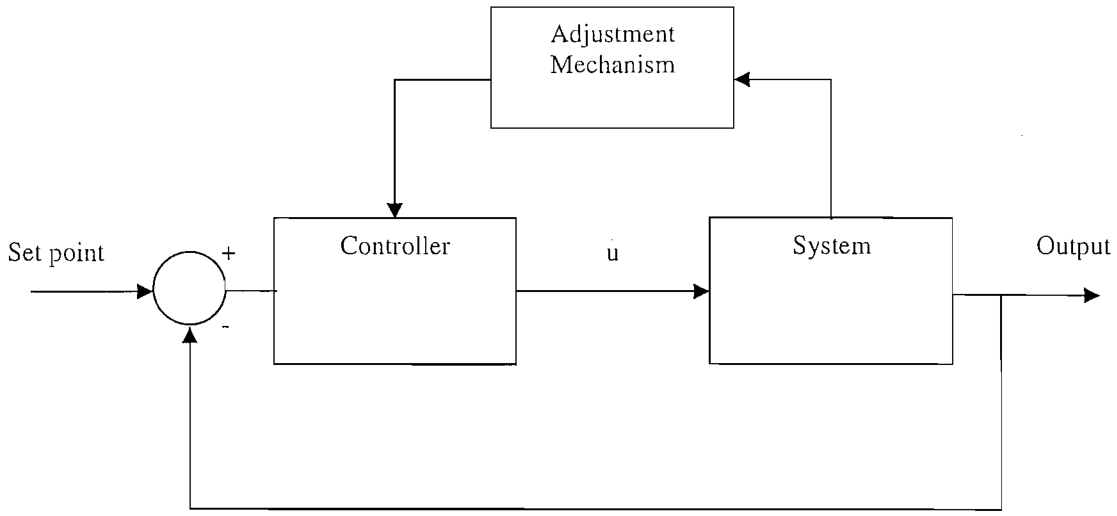

Figure 5.1. Standard self-tuning controller.

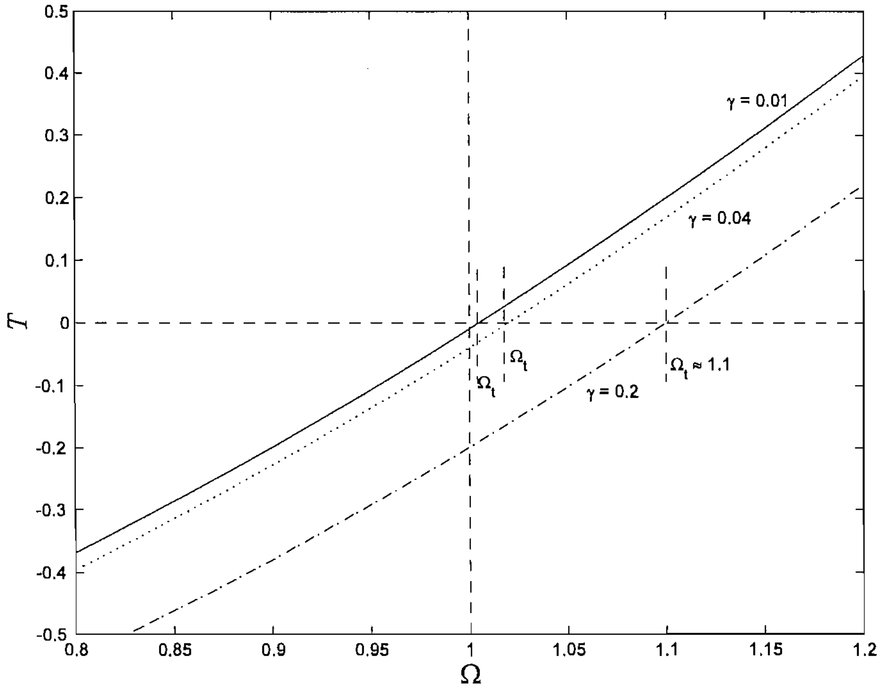

Figure 5.2. The numerator of τ_t as function of Ω for various γ, $\eta = 0$.

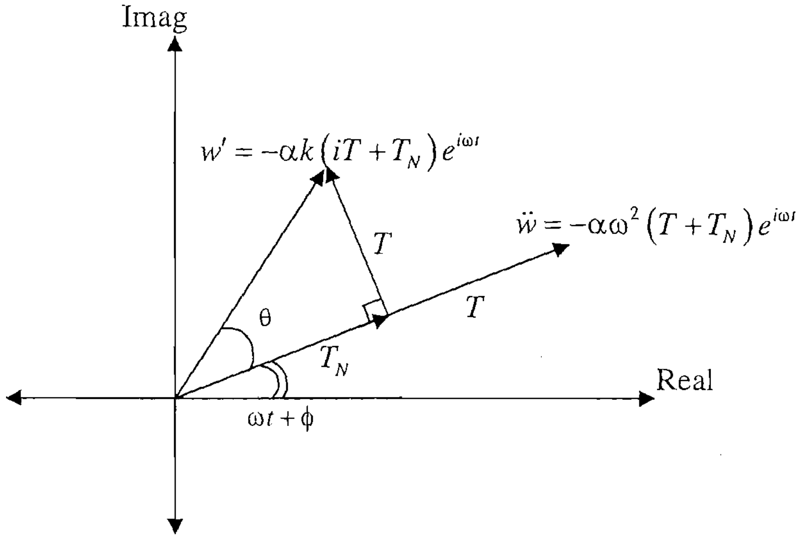

Figure 5.3. Angular displacement and acceleration of the beam in the complex plane.

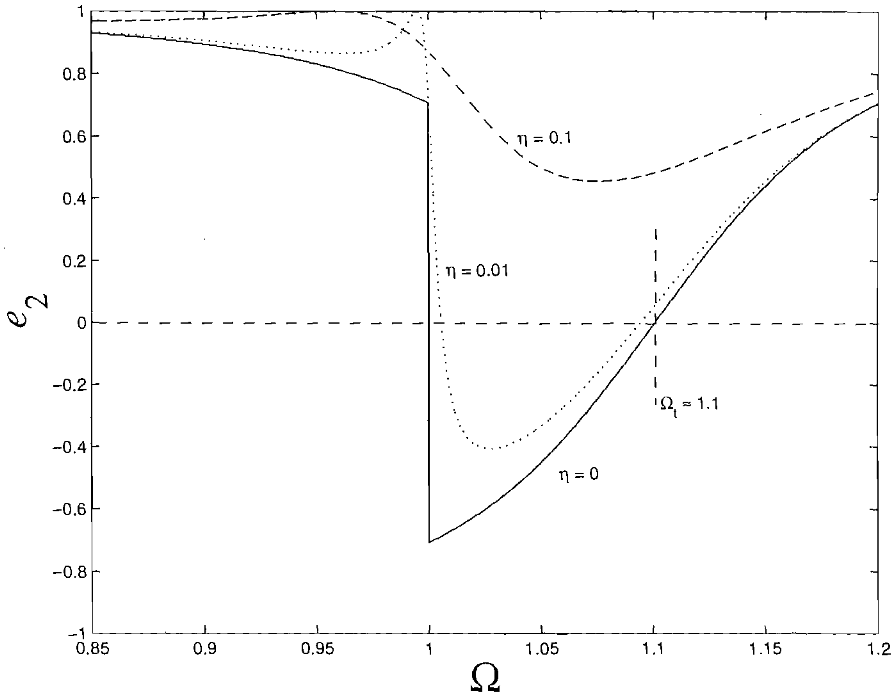

Figure 5.4. Variation of error function with Ω for various η, $\gamma = 0.2$.

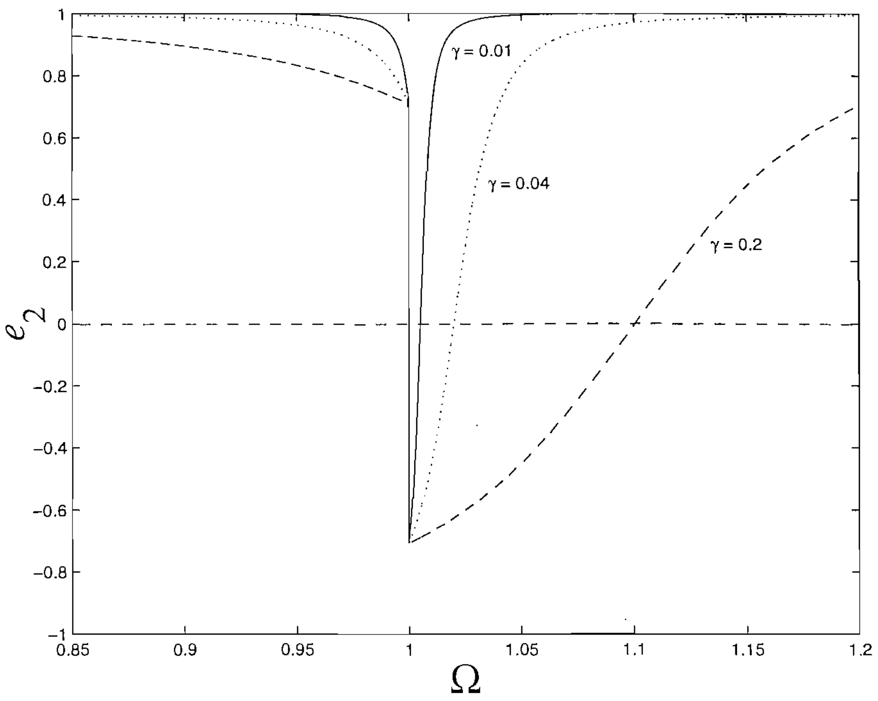

Figure 5.5. Variation of error function e_2 with Ω for various γ, $\eta = 0$.

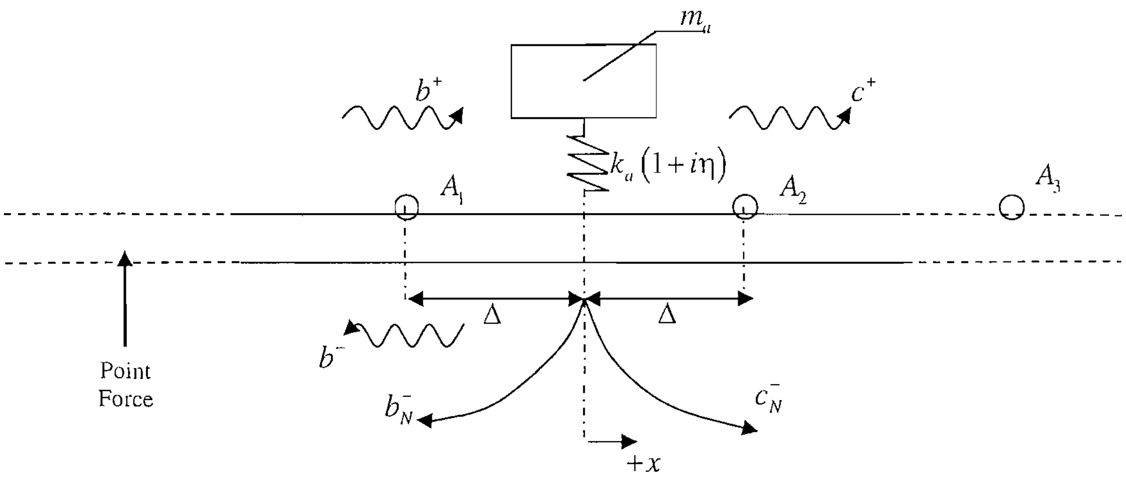

Figure 5.6. TVA mounted on an infinite beam in the farfield of a point force;

○ accelerometer

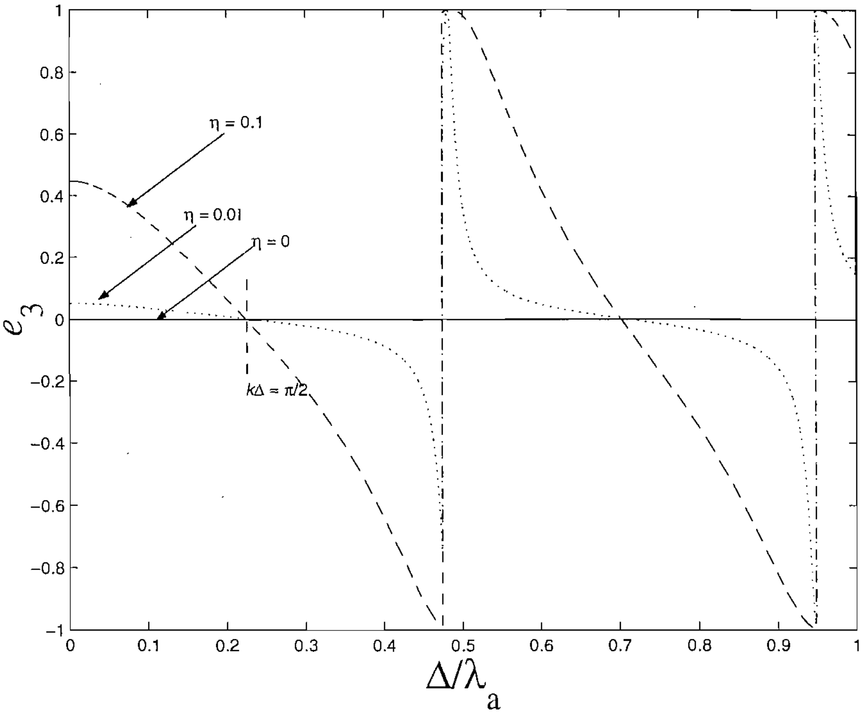

Figure 5.7. Variation of error function e_3 at $\Omega_l \approx 1.1$ with normalised spacing for various η; $\gamma = 0.2$.

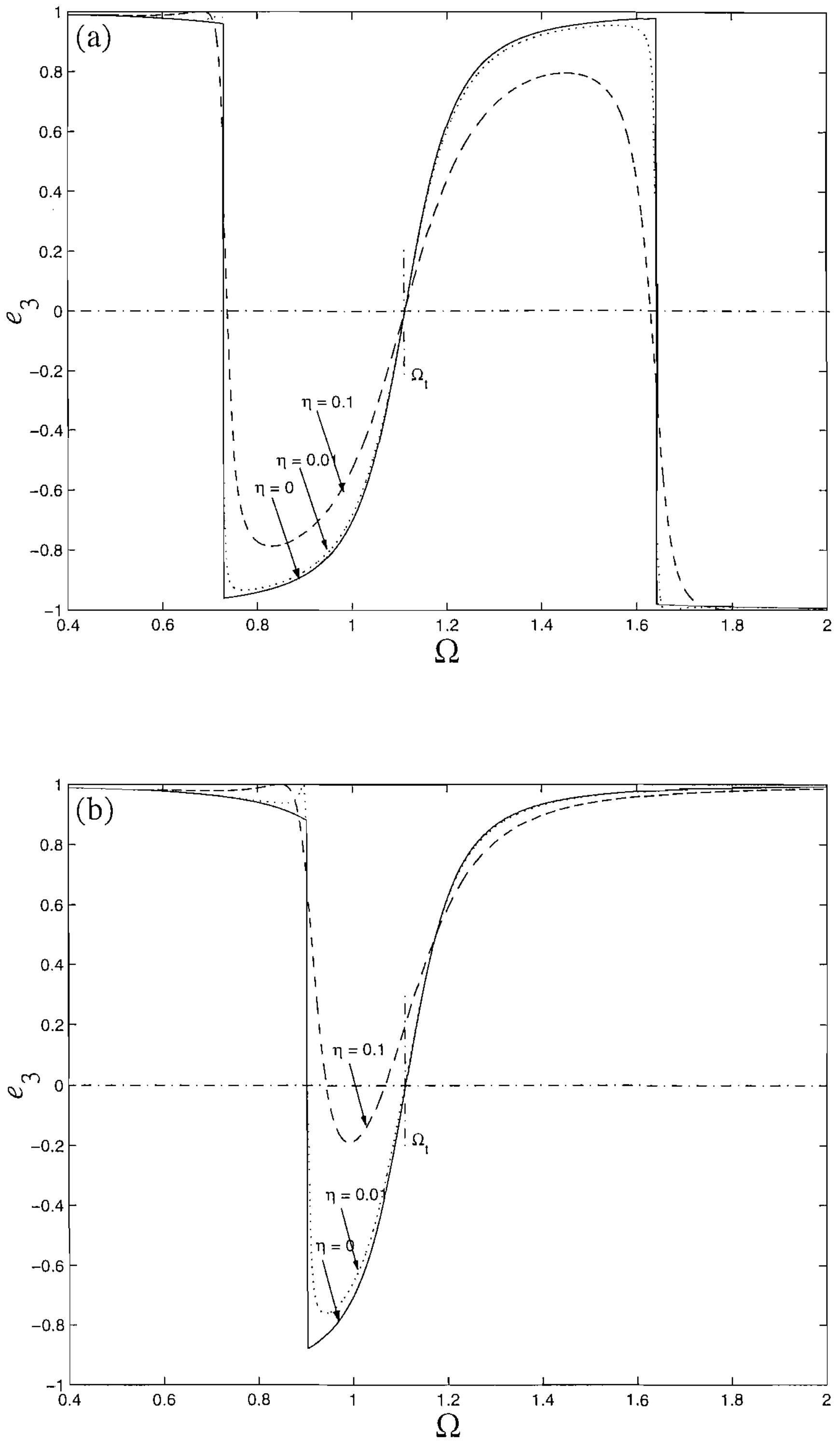

Figure 5.8. Variation e_3 with Ω for various η, $\gamma = 0.2$: (a) $\Delta / \lambda_a \approx 0.25$; (b) $\Delta / \lambda_a \approx 0.15$.

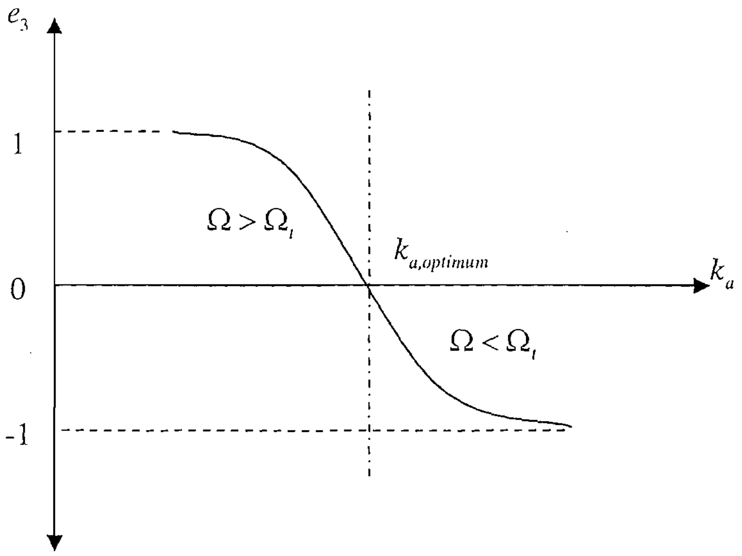

Figure 5.9. Variation of error function e_3 with ATVA stiffness k_a.

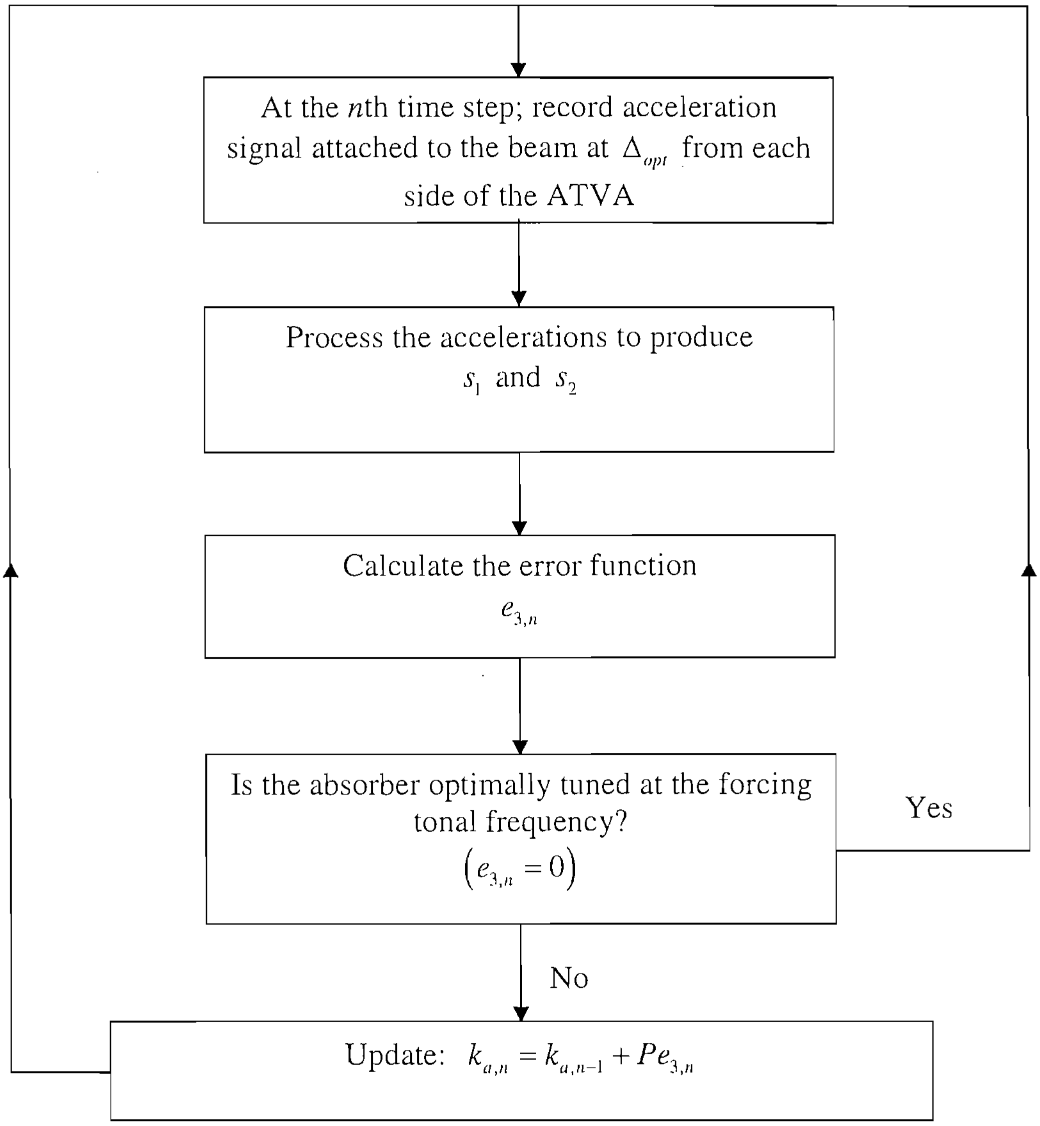

Figure 5.10. Flow chart of the control strategy.

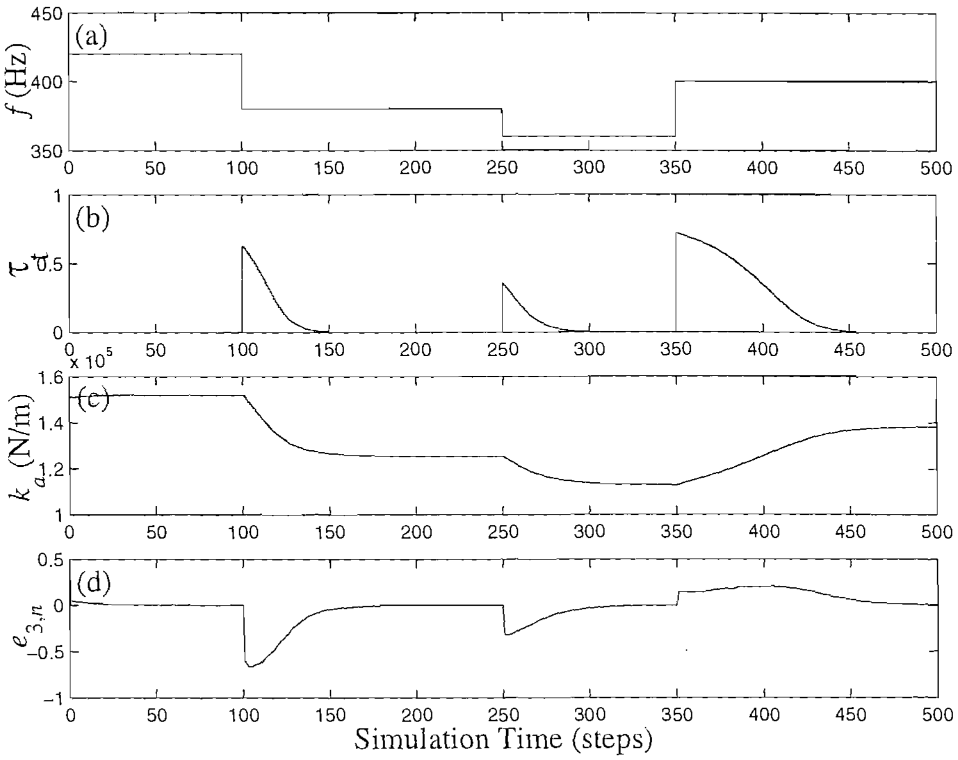

Figure 5.11. Control of the power transmitted on a beam; $P = 1.5\times10^3$, $\eta = 0$ and initial $\gamma = 0.2$: (a) disturbance frequency f; (b) τ_t; (c) k_a; (d) $e_{3,n}$.

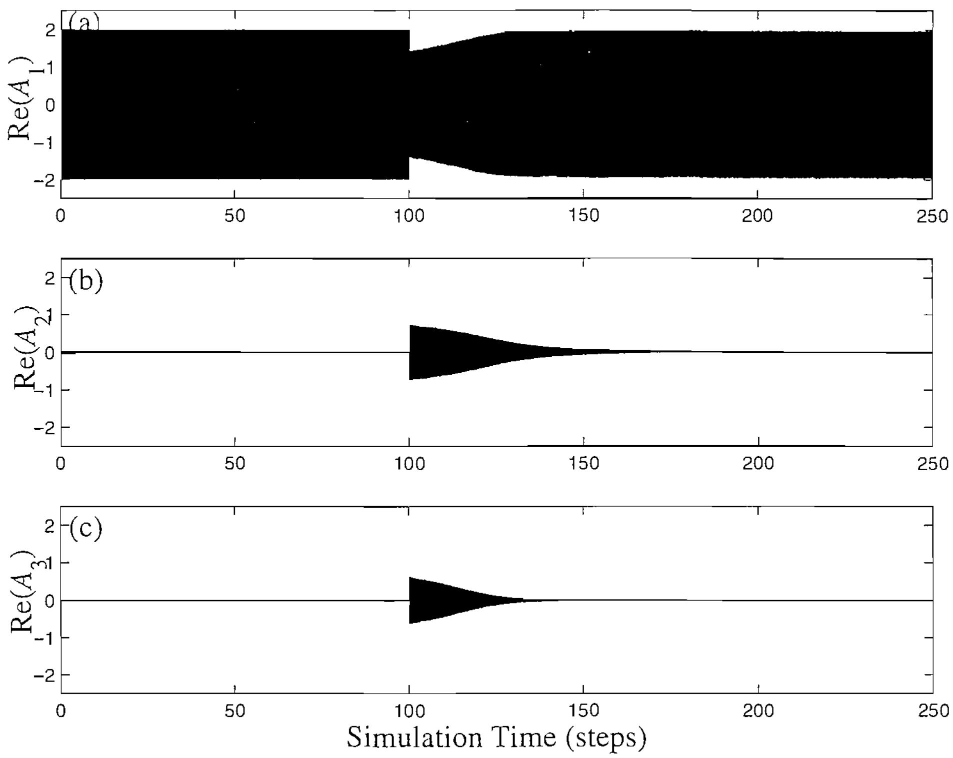

Figure 5.12. Response of the beam due to varying the disturbance frequency from 420 Hz to 380 Hz at simulation step = 100; $\eta = 0$ and initial $\gamma = 0.2$: (a) motion of the beam at distance Δ upstream of the ATVA; (b) motion of the beam at distance Δ downstream of the ATVA; (c) motion of the beam in the downstream farfield.

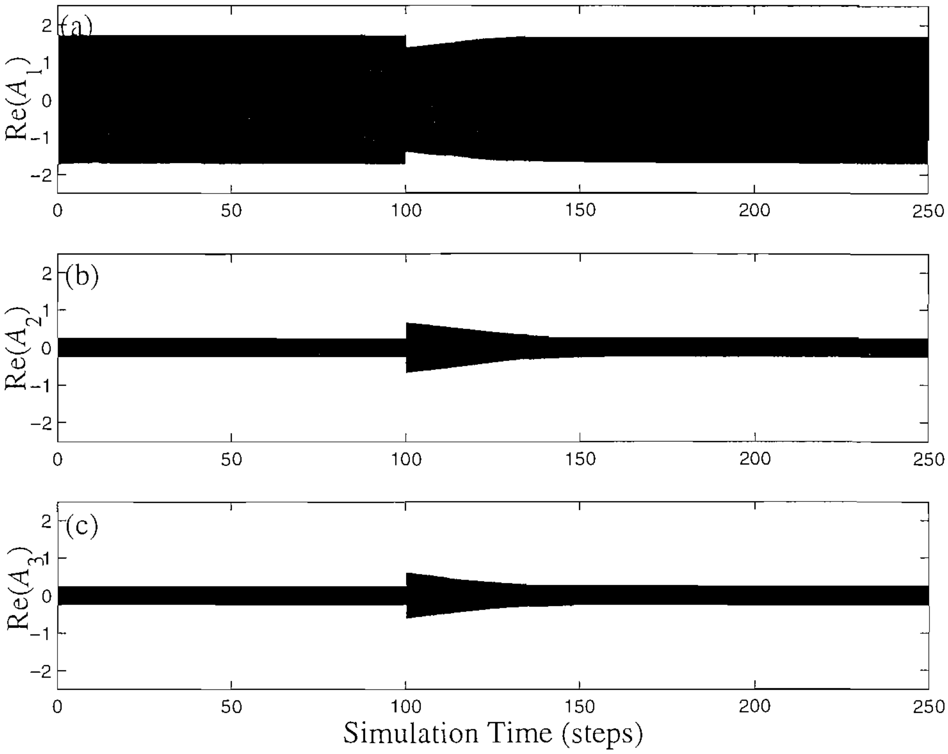

Figure 5.13. Response of the beam due to varying the disturbance frequency from 420 Hz to 380 Hz at simulation step = 100; $\eta = 0.05$ and initial $\gamma = 0.2$: (a) motion of the beam at distance Δ upstream of the ATVA; (b) motion of the beam at distance Δ downstream of the ATVA; (c) motion of the beam in the downstream farfield.

LIST OF TABLES

Reference Signal 1	Reference Signal 2
w	$\dot{w}'$
$\dot{w}$	w'
$\ddot{w}$	$\dot{w}'$
$\ddot{w}'$	$\dot{w}$

Table 5.1. Possible reference signals for optimum tuning

Parameter	Value
η	0
Initial γ	0.2
k (m^{-1})	$1.17\sqrt{f}$
Initial λ_a (m)	0.26
Initial k_a (N/m)	150×10^3

Table 5.2. Properties of an ATVA attached on a thin beam

CHAPTER 6: EXPERIMENTAL IMPLEMENTATION OF REAL-TIME CONTROL

6.1 Introduction

In Chapters 4 and 5 it was shown that the flexural waves propagating along a beam structure can be effectively reduced using a single adaptive tuned vibration absorber. With an ATVA the tuned frequency can be changed to match the current frequency of the disturbance. The variable stiffness absorber was manually re-tuned to control the flexural waves for various excitation frequencies and numerical simulations of self-tuning control were presented. An error function was developed in the previous chapter and utilised in numerical simulations involving a gradient descent algorithm. This error function indicates both the degree of mistune and the direction towards the optimum tuning, at which the transmitted power is minimum.

One objective of this research is to implement a self-tuning adaptive absorber on a beam such that the vibration absorber should tune automatically under computer control. In this chapter the effectiveness of the error function e_3 is examined experimentally and the control of the power transmission in real-time is presented.

Following the introduction, section 6.2 describes the experimental work undertaken to automate the control of the vibration absorber. In section 6.3 a discussion and some conclusions are drawn.

6.2 Experimental Work

The self tuning control of transmitted waves, using a variable stiffness ATVA discussed in the previous chapter, is applied experimentally in this section. The control system implements the developed error function e_3 in a gradient descent algorithm. Initially, a series of experiments are conducted in the frequency domain to test the effectiveness of the error function and the validation of the two sensor approach over a wide frequency range. Then the control algorithm is applied to change the stiffness of the thermo-elastic ATVA when the tonal frequency, exciting a thin steel beam, is varied within the tunable range of the ATVA.

6.2.1 Experimental testing of the error function e_3

The system comprising the thermo-elastic ATVA mounted to the thin steel beam described in Chapter 4 is used to validate the two sensor approach. The beam was excited by a Ling V201 shaker with band limited random noise from 50 to 800 Hz generated by an 8 channel HP 3566A analyser. Six PCB type 352C22 accelerometers were employed to measure the required signals. The accelerometers were divided into three pairs as shown in Figure 6.1. The purpose of the two pairs located away from the ATVA is to measure the powers incident, reflected and transmitted, whilst the pair located at distances Δ from the ATVA is used for measuring the required signals to calculate the error function e_3. Other equipment included a power amplifier and two PCB type 441A42 signal conditioners.

Figure 6.2 compares the numerical prediction of the error function e_3 to the experimental measurement for two different spacings; $\Delta_{opt} / \lambda_a \approx 0.25$ and $\Delta / \lambda_a \approx 0.13$. The thermo-elastic ATVA is attached in the farfield of the point disturbance with zero current input (ambient temperature). The error function e_3 was predicted using equation (5.12). Locating the accelerometers at $\Delta_{opt} / \lambda_a \approx 0.25$ each side of the ATVA is shown to be effective over a substantial frequency range. It is zero at the tuned frequency and its sign indicates over- or under-tuned. On the other hand, the effectiveness of the error function becomes limited when the accelerometers are located at a spacing ($\Delta / \lambda_a \approx 0.13$) other than the optimum spacing. For example, for frequencies less than about 350 Hz e_3 indicates an incorrect amount of mistune.

The performance of the error function at different stiffness values was validated experimentally as shown in Figure 6.3. The thermo-elastic ATVA was heated to four different temperatures and e_3 was measured for each temperature when the steady state was reached. The measured transmission ratio is also plotted for each temperature to demonstrate the validity of the error function, for different stiffness values, in indicating that minimum transmission occurs when $e_3 = 0$. At the tuned frequency (i.e. the frequency at which τ_t is minimum) for each temperature, shown in Figure 6.3a, the corresponding error functions $e_3 \approx 0$ (see Figure 6.3b). Furthermore, the 180° phase shift that occurs between the reference signals (s_1 and s_2) and discussed in the previous chapter tends to occur at lower frequencies when the stiffness of the absorber is decreased. The range of frequencies within which e_3 is operative (i.e. within which the sign of e_3 indicates the direction of miss-tune) becomes less with respect to temperature because of the reduction that occurs in the bandwidth $\Delta\Omega$ (γ decreases by decreasing k_a) and the fact that the value of Δ_{opt}/λ_a (i.e. $\Delta_{opt} \approx 0.06\,\mathrm{m}$) was initially set for the characteristics (absorber frequency) of the thermo-elastic ATVA at the ambient temperature. Nevertheless, the error function is effective over a reasonably wide frequency range for the cases where the absorber was operating at elevated temperatures.

The transmission ratios and the corresponding error functions obtained when cooling down the absorber are shown in Appendix 6. The measurements approximately agree with those shown in Figure 6.3 which was obtained when the absorber was being heated.

6.2.2 Experimental implementation of real-time control

The simulations presented in the previous chapter for self-tuning control using a variable stiffness ATVA are demonstrated experimentally in this section. This utilises the gradient descent algorithm and the error function e_3 discussed previously. The controller is applied to a thin steel beam with the thermo-elastic ATVA described in Chapter 4. Three PCB accelerometers are used. Two of the accelerometers are located at the optimum spacing $\Delta_{opt} \approx 0.06\mathrm{m}$ ($\Delta_{opt}/\lambda_a \approx 0.25$) each side of the ATVA while the third is mounted in the farfield of the point disturbance to monitor the performance of the self-tuning approach as illustrated in Figure 6.4. The control system was implemented using Simulink® including the Real Time Workshop and the Real Time Windows Target toolboxes. The use of such software enables the control system, which was used in the numerical simulation discussed in the previous chapter to be implemented. Parts of the Simulink model, including the estimation of the error function and the control algorithm blocks, were used previously by Rustighi *et al* [12] for the self-tuning control of an SMA ATVA attached on a vibrating host structure.

The disturbance and control signals were generated by a Pentium III 1 GHz PC, equipped with a National Instruments PCI-MIO-16E-4, I/O board for analogue and digital data acquisition. All real-time processing was performed using Matlab and Simulink software incorporating the real-time toolboxes. The disturbance generated by the computer was used to drive a Ling V201 shaker while the control signal generated by the controller/Simulink was used to drive a Lambda ZUP10-20 current supply. The electric current generated by the power supply could generate a maximum voltage of 10 V or a maximum current of 21 A. The measured accelerations were fed into a signal conditioner then to the PC to estimate the cost function e_3. Then the consequent control signal was generated. A thermocouple was used to monitor the surface temperature of the stainless steel wires during the experiments. In order to avoid any high frequency noise that might contaminate the signal sent to the shaker, a low pass filter (Kemo® BenchMaster VBF 8) was used with a cut-off frequency of 500 Hz, well above the adaptive rate of the thermo-elastic ATVA.

The Simulink model used for the self-tuning control and is described in Appendix 7. The model includes a block that generates a sinusoidal signal, which is sent to drive the shaker. The signals measured from the two accelerometers attached at the optimum locations were input to a block that derived the reference signals s_1 and s_2 from which the error function e_3 was estimated. High pass digital filters are used to remove any DC offset. The error function is input to the control block and the control algorithm. The control signal that is updated in proportion to the error function is the electric current passed through the ATVA. Note that increasing the current decreases the stiffness of the ATVA. Thus, the control algorithm shown in equation (5.13) that uses stiffness as a control parameter becomes

$$I_{n+1} = I_n - Pe_{3,n} . \qquad (6.1)$$

The current generator has an analogue voltage input which determines the output current, i.e. an input signal between 0 and 4 Volts can be used to produce a current between 0 and 21 A. In order to avoid the possibility of over-heating the variable stiffness elements of the ATVA, a saturation block was implemented to prevent the power supply from generating a current over 9 A (100 °C).

Experimental tests were carried out to investigate the response of the control system including the performance of the thermo-elastic ATVA. The controller updates at the sampling frequency of 1 kHz, and the constant P was set to 1.5×10^{-3}.

For the first test, the disturbance frequency was initially set to approximately the lowest tuned frequency the absorber can reach 314 Hz, and the system run for 1000 sec (≈ 18 minutes) to allow the steady-state to be reached. The frequency then increased to 420 Hz (i.e. the tuned frequency at the ambient temperature) and the system continued to run for 2000 sec (≈ 33 minutes). The results of this test are shown in Figure 6.5. For the first part of the test, when the excitation frequency is 314 Hz, the estimated error function was negative (see Figure 6.5a), which in turn directed the controller to drive current through the ATVA to heat it. The current increased and reached the saturation limit of 9 A after 20 sec, then remained at that value for about 350 sec (≈ 6 minutes) after which optimal tuning was close to be achieved. This involved a 25% change in the tuned frequency. The attenuation achieved at that frequency was about 11 dB. This agrees with the attenuation achieved for the results obtained in the frequency domain at constant frequency (see Figure 4.15). The error function decreased and fluctuated around zero as the controller was trying to maintain the tuned stiffness at that excitation frequency, as shown in Figure 6.5b. The sensitivity of the stiffness elements used in the ATVA, towards heat transfer can elucidate the difficulty in continuously maintaining $e_3 = 0$ with time. However, this did not affect the significant attenuation achieved. The reflected power has increased correspondingly as expected and shown in Figure 6.5c. It should be noted that Figure 6.5c shows the envelope of the acceleration amplitudes, calculated by taking the absolute value of the Hilbert transform of the data [78]. When the disturbance frequency decreased to 420 Hz the error function was positive, this in turn directed the controller to reduce the electric current. After about 1 minute from the time the disturbance frequency increased to 420 Hz the current reached 0 A allowing the ATVA to stiffen slowly, as this process depends on the temperature of the ATVA, which in turn depends on the ambient temperature. The maximum attenuation achieved for the second stage was about 14 dB and this was achieved after about 1000 sec (≈ 18 minutes). This was less than that measured using the steady-state frequency behaviour (20 dB). Note that there was a change in the ambient temperature when results are recorded. It is worthy of note that the thermal behaviour of the thermo-elastic ATVA is slow.

Another experimental test was conducted for 3000 sec (50 minutes) with the disturbance frequency changing from 420 Hz to 314 Hz after 500 sec. The results are shown in Figure 6.6. The first disturbance frequency was 420 Hz with the absorber close to being tuned and with $I = 0$. The controller decision was to take no action. Decreasing the disturbance frequency to 314 Hz gives a negative value for the error function; hence the controller increases the current and this heat up the absorber. Optimum tuning is reached after about 350 sec (≈ 6). It should be noted that the time taken by the controller to tune the absorber optimally was the same as in the previous test. Afterwards, the error function fluctuated around zero as described previously. The control is seen to oscillate, with current being alternatively switched on and off. It is believed that this behaviour could be avoided with a different control strategy.

6.3 Discussion and Conclusions

The effectiveness of the error function has been validated experimentally, indicating the degree of tuning and the direction of re-tune towards the optimal tuning for the thermo-elastic ATVA.

The error function was successfully implemented in an adaptive control system that automatically tunes the thermo-elastic ATVA at various tonal frequencies. This has been examined experimentally and the results show that it is quicker to tune the absorber when the excitation frequency is less than the default tuned frequency due to the thermal time constants of the absorber materials. For a negative error function (i.e. the ATVA is at ambient temperature), the maximum shift in the tuned frequency of the thermo-elastic ATVA 25% was achieved after about 6 minutes by heating up the absorber. For a positive error function (i.e. the ATVA is too hot), the 25% shift in the tuned frequency is achieved after about 16 minutes in cooling down the absorber naturally. This depends on the ambient temperature.

In general, the self-tuning control system including the adaptive thermo-elastic absorber has proved effective at reducing the level of vibration in the farfield of a beam structure at different excitation frequencies.

FIGURES FOR CHAPTER 6

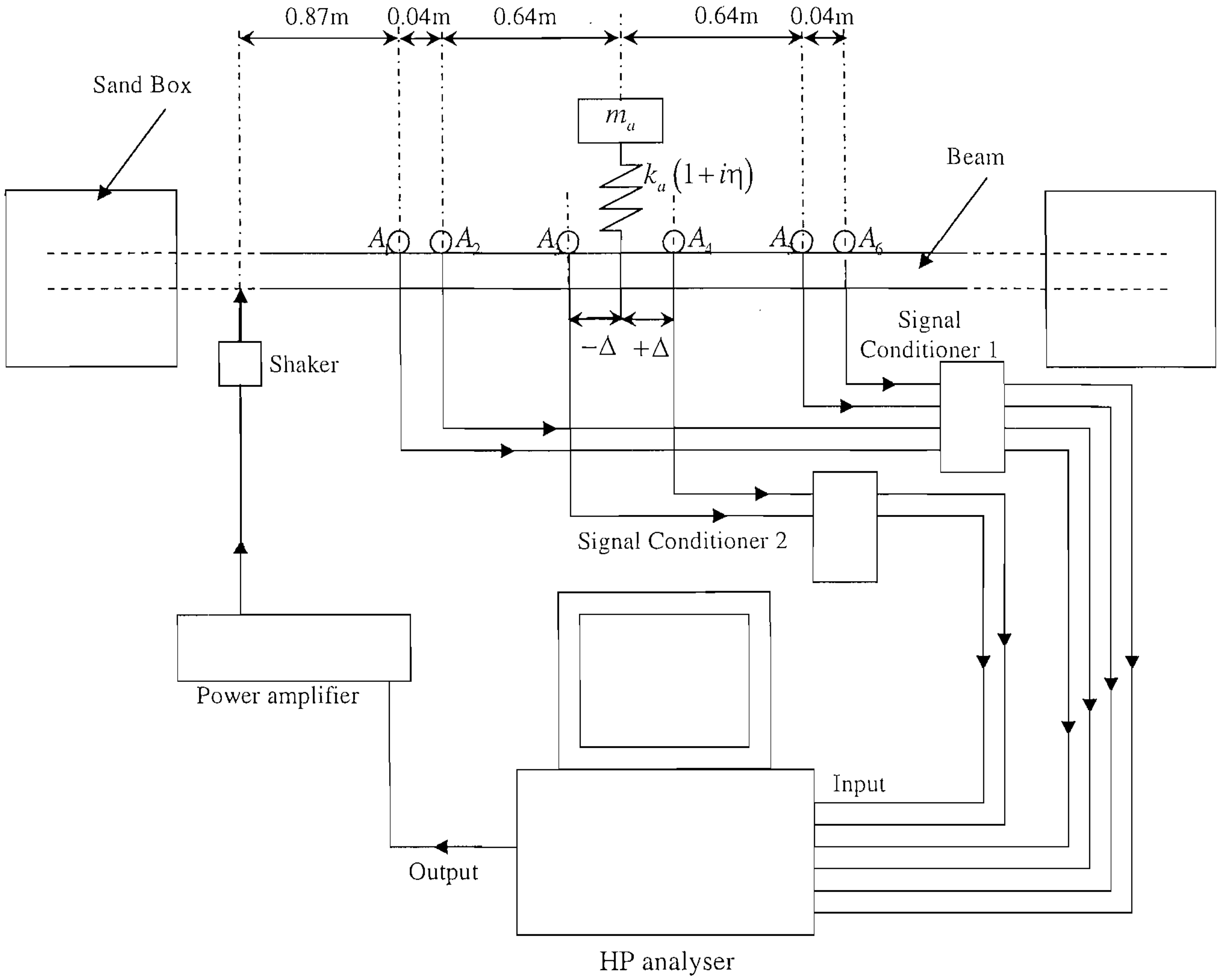

Figure 6.1. Experimental setup for validating the effectiveness of the error function;

○ accelerometer.

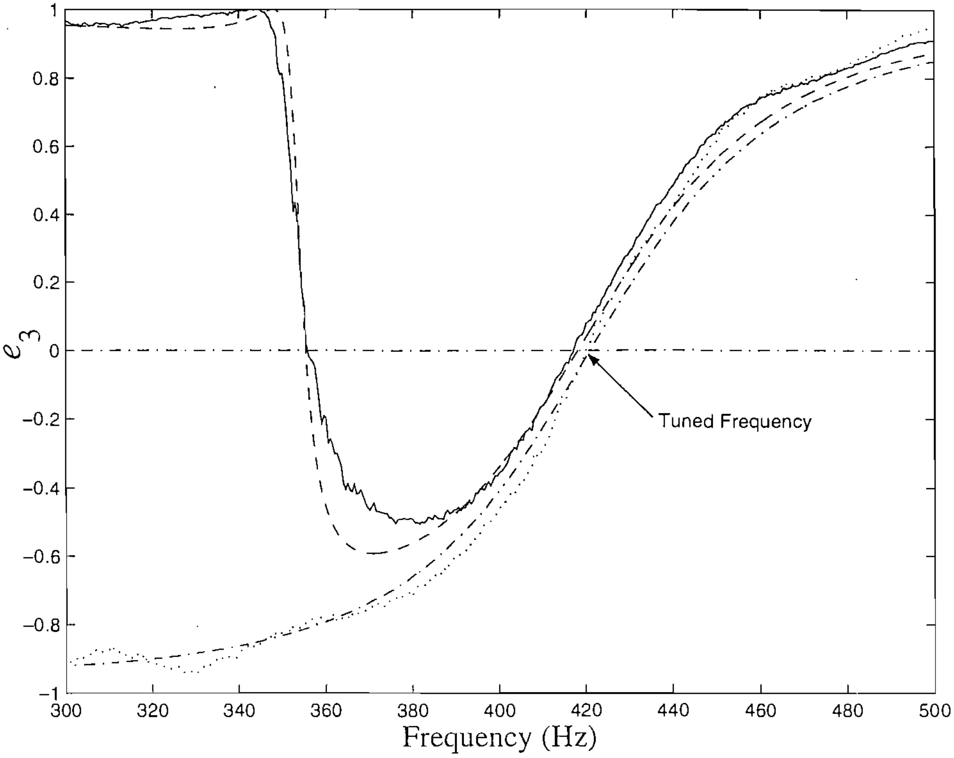

Figure 6.2. Variation of e_3 with frequency for different Δ from the thermo-elastic ATVA; $\eta \approx 0.018$.

———— $\Delta / \lambda_a \approx 0.13$, experiment; -------- $\Delta / \lambda_a \approx 0.13$, theory;

.... $\Delta / \lambda_a \approx 0.25$, experiment; -·-·-·-·- $\Delta / \lambda_a \approx 0.25$, theory

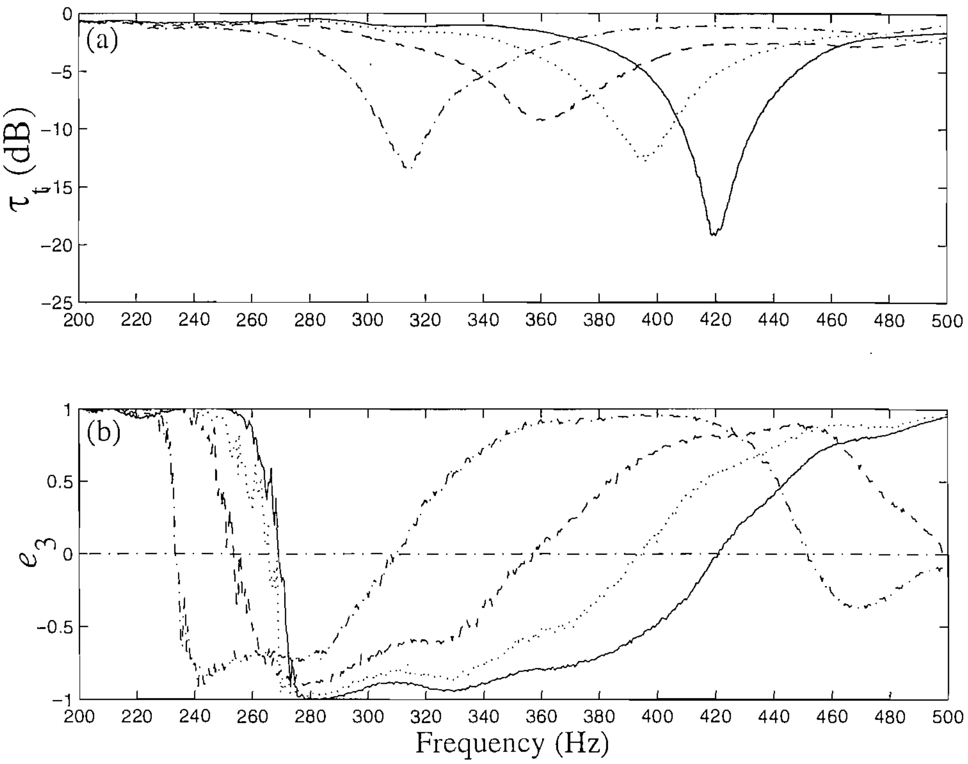

Figure 6.3. Effect of stiffness variation of the thermo-elastic ATVA on e_3 when $\Delta / \lambda_a \approx 0.25$. (a) τ_t ; (b) e_3.

——— $T_a = 21°C$; ………… $T = 33°C$; - - - - - - $T = 45°C$; -·-·-·- $T = 68°C$

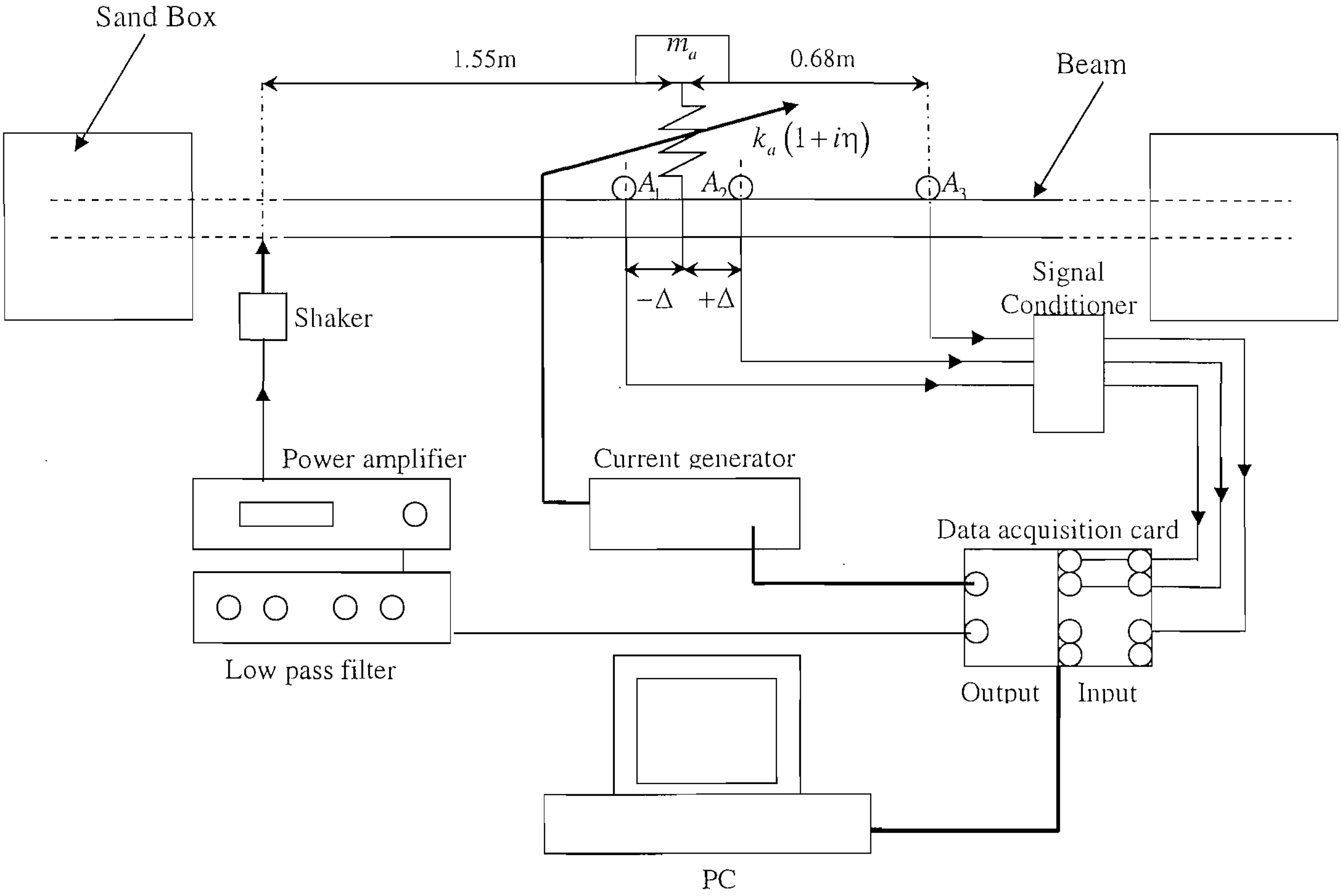

Figure 6.4. Experimental set-up for the self-tuning control.
○ accelerometer

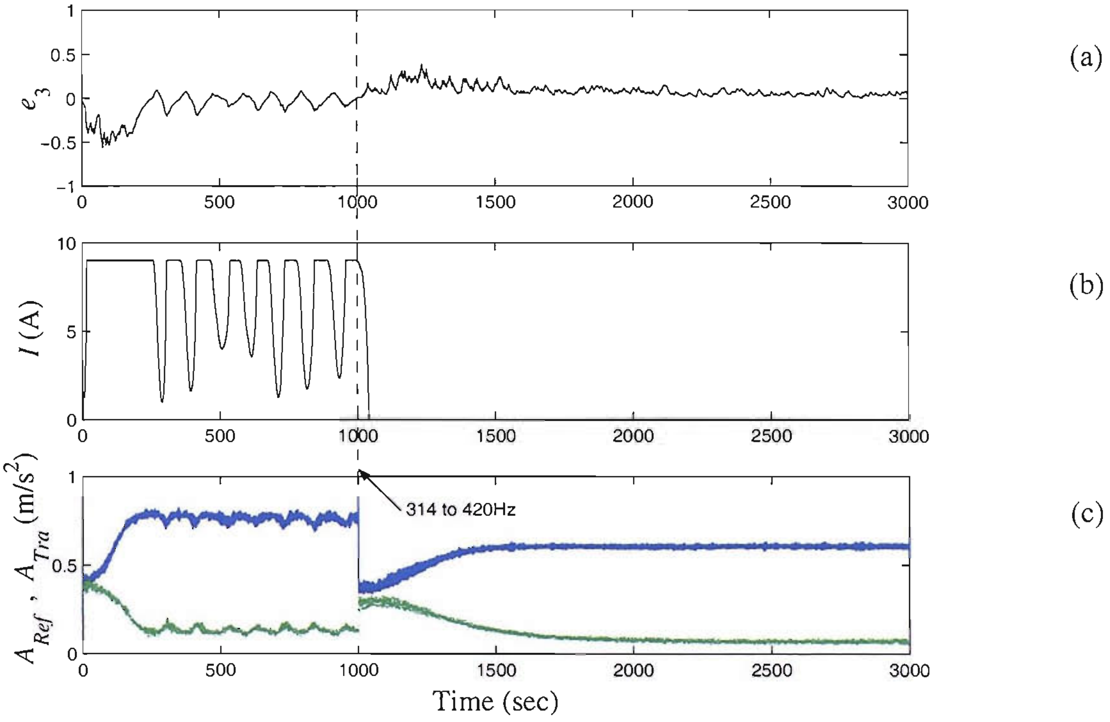

Figure 6.5. Real-time control of the farfield vibration for 3000 sec at an instantaneous frequency increase from 314 to 420 Hz at 1000 sec.
(a) error function; (b) electric current; (c) envelope of acceleration amplitudes at upstream——— A_{Ref} and downstream ·············· A_{Tra} location.

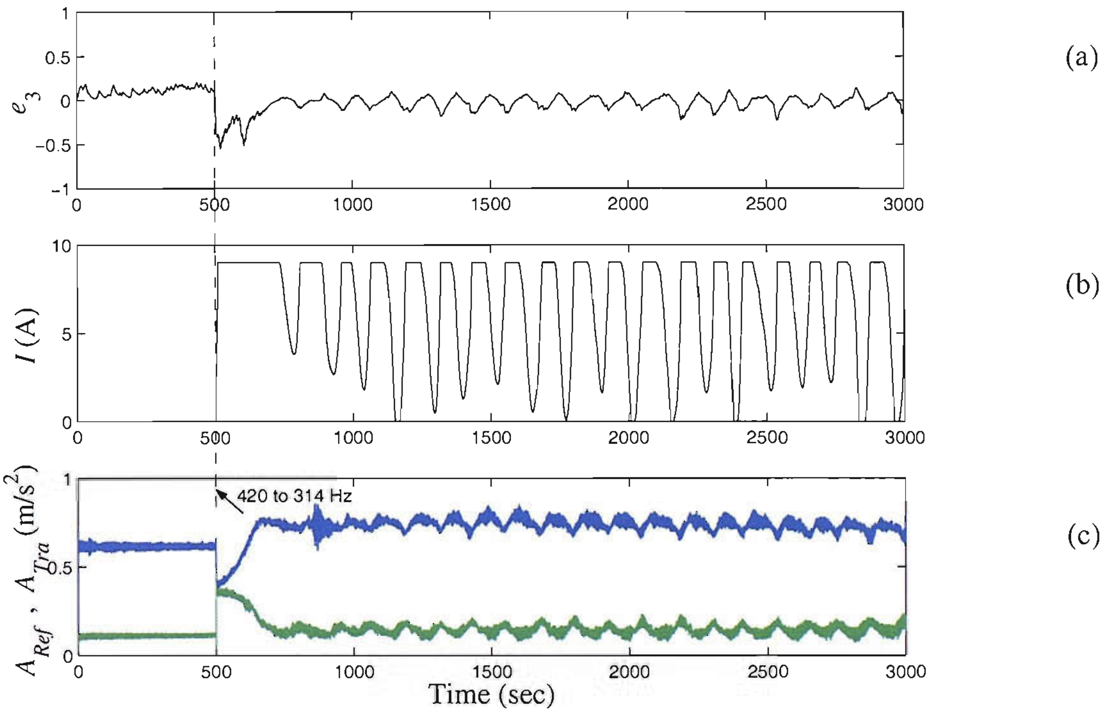

Figure 6.6. Real-time control of the farfield vibration for 3000 sec at an instantaneous frequency decrease from 420 to 314 Hz at 500 sec.
(a) error function; (b) electric current; (c) envelope of acceleration amplitudes at upstream———— A_{Ref} and downstream ·············· A_{Tra} location.

CHAPTER 7: CONCLUSIONS AND RECOMMENDATIONS FOR FURTHER WORK

7.1 Conclusions

This thesis concerned a self-tuning adaptive-passive vibration absorber to control the flexural waves propagating on a beam structure. In this chapter general conclusions of this thesis are summarised. Since the detailed points are contained in each chapter, only the major points will be reviewed here.

Following the introduction and literature review in Chapter 1, Chapter 2 discussed the principle types of wave motion in beam structures: longitudinal, flexural and torsional waves. The wave equations were stated with emphasis being placed on the importance of controlling flexural waves over longitudinal and torsional ones. However, the two latter waves may also exist in a beam exposed to vibration. The importance of nearfield waves was discussed. It was shown how these exponentially decaying waves are able to increase the power transmitted close to discontinuities and boundaries. Methods for measuring the wave amplitudes of the propagating waves and the wavenumber of a beam structure were described. These methods were implemented experimentally in the subsequent chapters. The reflection and transmission coefficients of a general point discontinuity subjected to an incident propagating wave were found. These coefficients were developed in Chapter 3 for a tuned vibration absorber mounted on a beam at a point.

Chapter 3 concerned the theoretical analysis and experimental investigation of the effect of a passive vibration absorber on controlling the flexural waves propagating on a beam structure. The tuned vibration absorber was modelled as a spring-mass system attached to a beam as a point translational impedance. Analytical expressions for reflection and transmission ratios of the vibration absorber were derived and found to be functions of four independent tuning parameters: the absorber frequency, the mass ratio, the damping ratio and the non-dimensional distance between the absorber and the disturbance. The effects of these parameters on the performance of the absorber in controlling the power transmission were investigated. It was shown how the location of the vibration absorber only affects the tuned frequency if the nearfield waves are significant. Attenuation in both waves, i.e. the power transmitted downstream of the vibration absorber and the total power reflected upstream of the point force, can be achieved at the tuned frequency. This is only the case if the absorber is attached at points whose distances from the absorber are approximately multiples of half the wavelength at the absorber frequency. It was found that the maximum power is dissipated by the vibration absorber when the mass ratio has approximately the same value as the damping ratio of the absorber. Experiments determining transmission and reflection ratios of a passive vibration absorber validated the theoretical predictions. The absorber was modelled as a beam-like absorber. Locating the absorber at the optimum locations gave attenuation in both power transmission and power reflection at the tuned frequency of up to 30 dB.

Controlling the power transmission over a range of frequencies required the use of an adaptive-passive vibration absorber. Chapter 4 presented two designs of variable stiffness absorbers that implemented different materials. The stiffnesses of the absorbers can be changed by varying the temperature of the materials used: the first absorber utilised shape memory alloy wires held together at the centre using epoxy-resins and was called the shape memory alloy absorber, while the second absorber utilised stainless steel wires with epoxy-resins at the centre and was called the thermo-elastic absorber. It was discussed how increasing the temperature of the shape memory alloys increased the stiffness of the absorber. On the other hand, increasing the temperature of the epoxy-resins decreased the stiffness. In the experimental validation, the shape memory alloy absorber showed about a 20% change in the tuned frequency with a maximum attenuation of 11dB at the ambient temperature while the thermo-elastic absorber exerted about 27% change in the tuned frequency with a maximum attenuation of 13 dB. Using the thermo-elastic vibration absorber to attenuate the transmission in a second beam with a smaller cross-section increased the maximum attenuation to 20 dB at the ambient temperature. In addition to the advantages offered by passive control, the advantages of the proposed adaptive absorbers can be summarised in the following: the simplicity of the design, the effectiveness in attenuating the power transmission over a range of frequencies, the low cost of the materials used, the small size of the absorbers and the fail-safe nature of the system. The time required by the absorbers to reach the steady state is the main drawback of the absorbers introduced in this thesis. Another disadvantage is that the damping ratio of both absorbers varies significantly with temperature, which affects the maximum attenuation that can be achieved at the tuned frequency.

Self-tuning control to change the stiffness of an adaptive absorber to suppress the power transmission at varying frequencies was discussed in Chapter 5. Only one control strategy was investigated; this implemented the gradient descent algorithm. The algorithm employs an error function that should be zero to realise optimum tuning where minimum power transmission is achieved. For this purpose, an appropriate error function was found by using two accelerometers. Each accelerometer is located a quarter of a wavelength from the absorber. The outputs of the accelerometers were summed and differenced, with one time integration of the summed value. The phase between these two signals is 90° when the absorber is tuned (i.e. the error function is the cosine of the phase between the two signals). The error function indicated both the degree of mistune and the direction towards the optimum tuning. This had the advantage of operating over a wide range of frequencies with damping having little effect on the accuracy of the error function. A series of numerical simulations validated the effect of the proposed control strategy on the attenuation of the power transmission, hence on the beam motion in the downstream region, for various tonal disturbances.

A number of experiments were conducted and reported in Chapter 6. The effectiveness of the error function in determining the direction of tuning towards the optimum stiffness was validated using the thermo-elastic absorber. This absorber was tuned automatically using the gradient descent algorithm and the error function found in Chapter 5 to control the power transmission for varying tonal disturbances. The experimental results showed that that absorber attained considerable reductions (up to 14 dB at the ambient temperature) in vibrations of the beam at the downstream position. This is slightly less than that obtained in the frequency domain which can be a result of the significant variation in the ambient temperature. Due to the thermal characteristics of the absorber, the time taken by the absorber to heat up was about one third the time taken when cooling down.

Overall the thesis demonstrates the ability to control the transmission of flexural waves on beam structures using a self-tuning adaptive-passive vibration absorber. The control system comprising a thermo-elastic vibration absorber, detection sensors and controller was capable of successfully attenuating the vibration transmission at single frequencies or over a narrow frequency band and tracking changes in this frequency.

7.2 Recommendations for Further Work

It was evident that, even if the amplitude of acceleration of the beam in the farfield region was significantly reduced, the electric current and the error function fluctuated and did not reach a steady value. Therefore, an alternative control algorithm could be developed and implemented to reduce the thermal effects of the thermo-elastic absorber which influences the time required to reach the steady state. The stability of the controller could be enhanced by adding a derivative action to the existing proportional control.

It is recommended that further work be undertaken to investigate the operational mode of the thermo-elastic absorber. This should provide knowledge to enhance the design of the absorber to reduce the thermal inertia which in turn would reduce the time required to reach the steady state and present a more effective absorber.

The work could also be extended by investigating the effect of thermoset plastics other than epoxy-resins on varying the stiffness with temperature for the purpose of obtaining a quicker response in the face of varying excitation frequency and acquiring a wider range in the tuned frequency when the temperature varies.

Appendix 1: Relative Calibration of Accelerometers

A set of preliminary experiments were undertaken prior to any measurement that necessitates the use of two or more accelerometers. These initial experiments concern the relative calibration of the accelerometers to avoid the erroneous data that may originate from defective accelerometer(s). Ideal accelerometers should measure identical response from a single point at a structure; however, accelerometers may deviate from the original sensitivity tabulated by the manufacturer due a number of reasons. These could be excessive temperatures, excessive loading stresses and damage caused by accidental drop of sensors. Therefore, a constant calibration factor c_{factor} can be found for each accelerometer relative to a chosen reference one. The calibration factor is found by

$$c_{\text{factor}} = \frac{\left|\overline{A_n(\omega)}\right|}{\left|\overline{A_{ref}(\omega)}\right|}, \tag{A1.1}$$

where A_n is the acceleration of any accelerometer needing a relative calibration while A_{ref} is the acceleration of the reference accelerometer.

The calibration factor of two PCB accelerometers type 352C22 (A_1 and A_2) was inspected with respect to a reference accelerometer of the same type (A_{ref}). Each of the accelerometers A_1 and A_2 were attached by means of wax one at a time to the reference accelerometer. Consequently, the accelerometers were excited by a Ling shaker V201 over a frequency span of 50-800 Hz. The calibration factor c_{factor} was found for each of the accelerometers using equation (A1.1). Therefore, $c_{\text{factor}} = 0.93$ for A_1, while $c_{\text{factor}} = 1.026$ for A_2. Figure A1.1a shows the relative accelerations as function of frequency without using the calibration factor. It is clear that both relative accelerations A_1 / A_{ref} and A_2 / A_{ref} have values close to 1. Nevertheless, these values are closer to 1 by using the calibration factor found for each accelerometer as shown in Figure A1.1b.

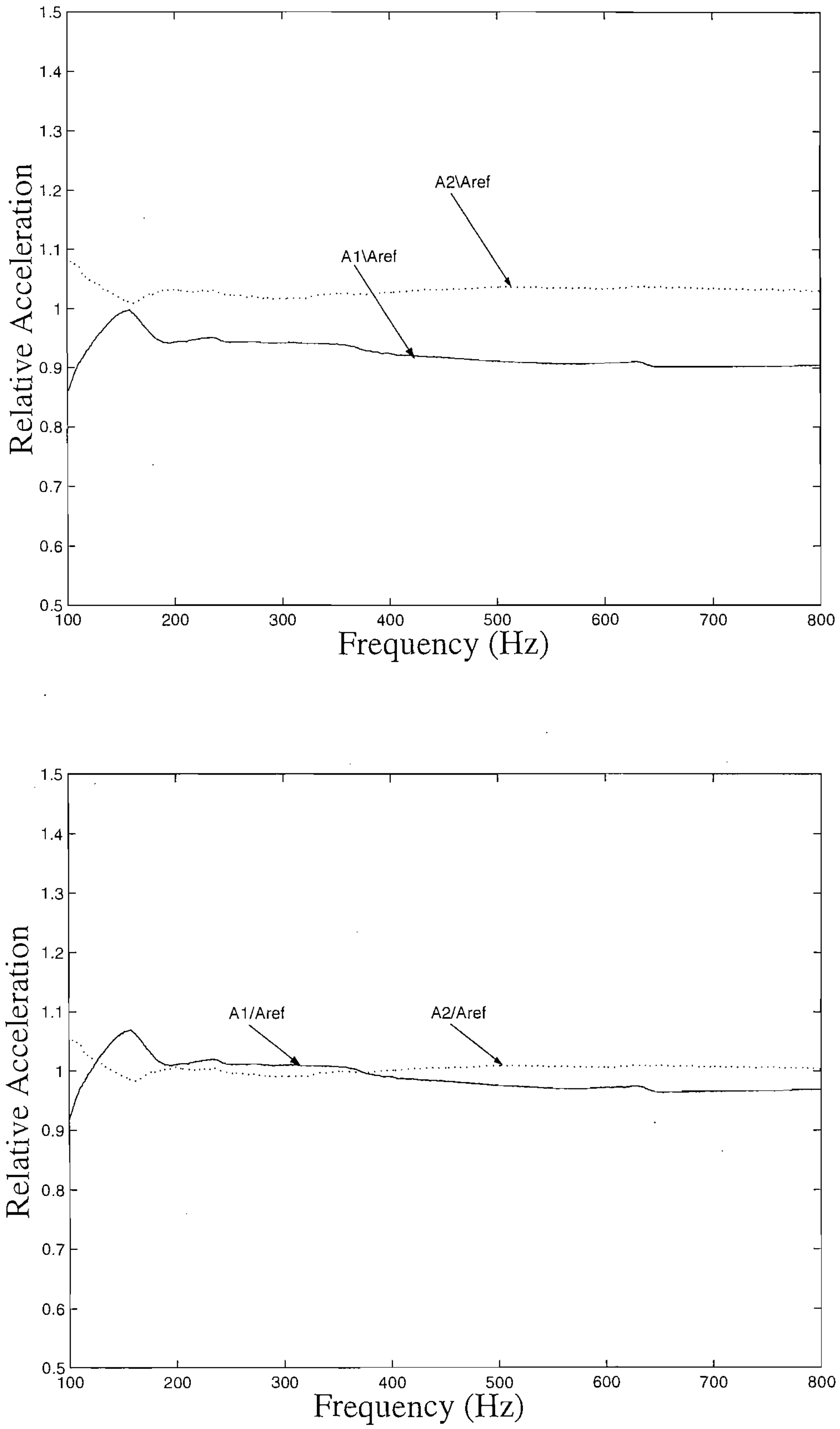

Figure A1.1. Relative accelerations: (a) without using c_{factor} ; (b) with using c_{factor} .

Appendix 2: Repeatability in the Response of the SMA Absorber with Temperature.

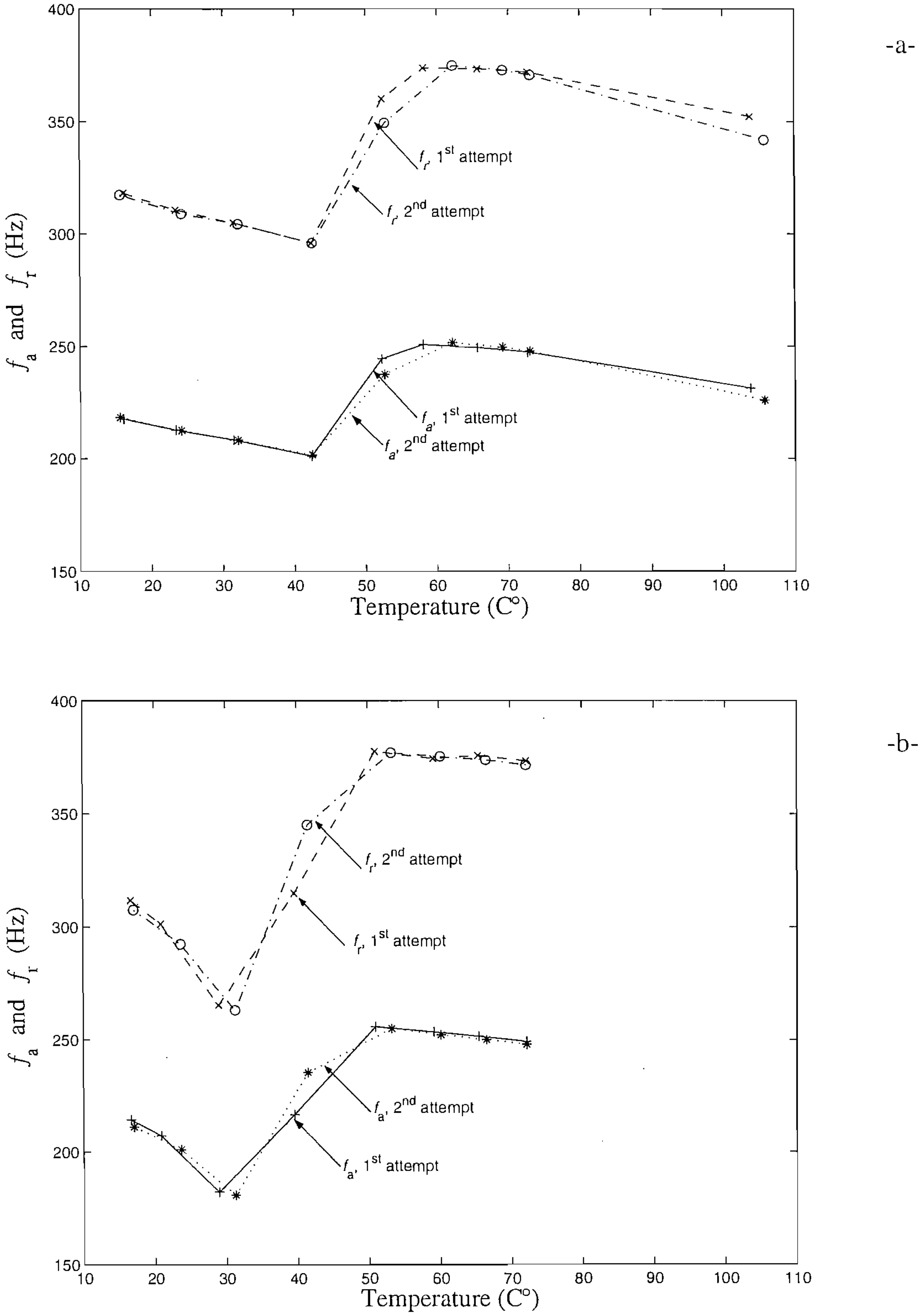

Appendix 2. Repeatability in the response of SMA ATVA with temperature:
(a) heating; (b) cooling.
———f_a, 1st attempt; ………f_a, 2nd attempt; - - - - - f_r, 1st attempt; - · - · f_r, 2nd attempt.

Appendix 3: Temperature Distribution along the SMA Wires

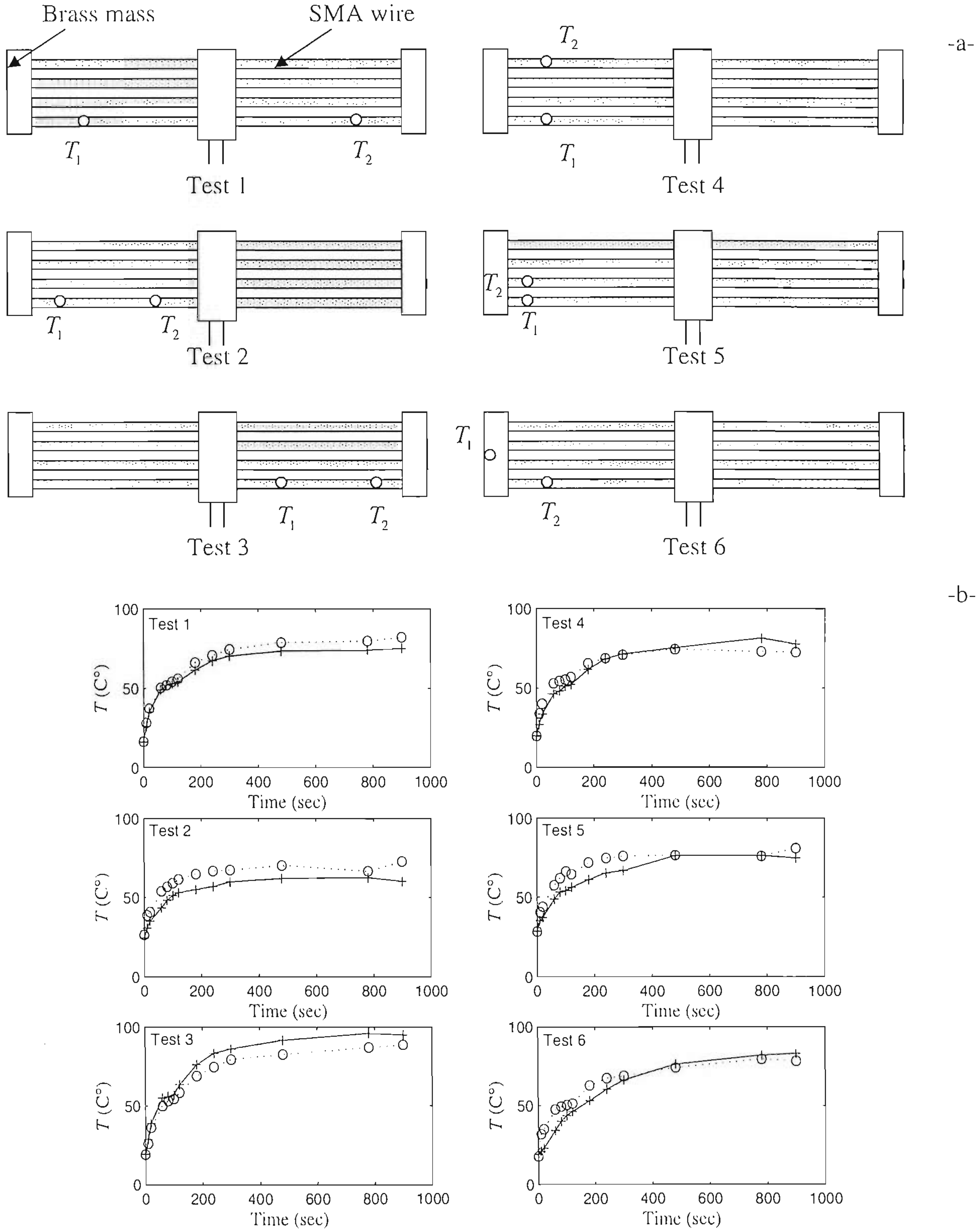

Appendix 3. Distribution of temperature along the SMA ATVA for 9 A current input: (a) location of thermocouple on the absorber; (b) temperature distribution.

———————— T_1; .... T_2

Appendix 4: Repeatability in the Response of the Thermo-Elastic Absorber with Temperature.

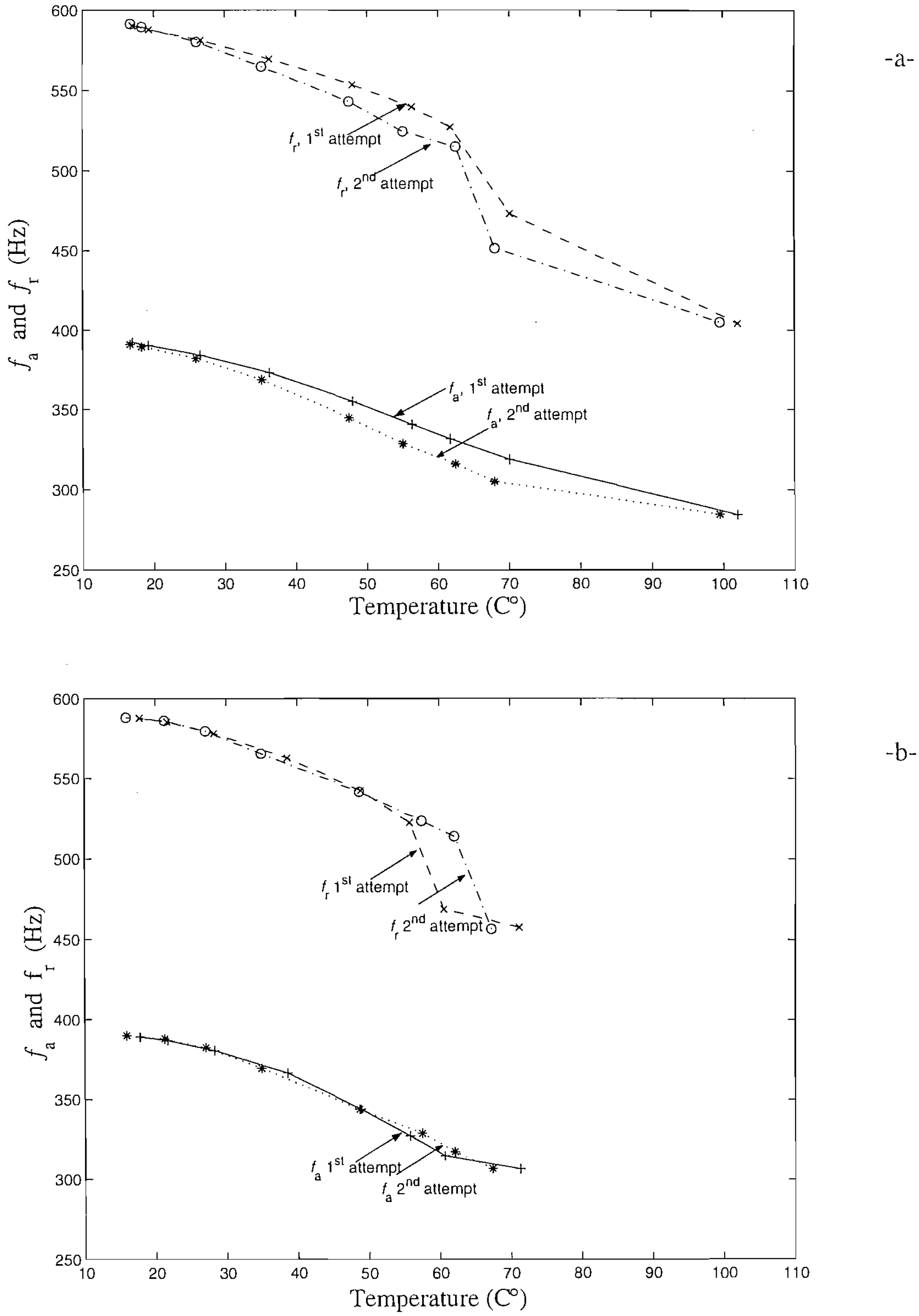

Appendix 4. Repeatability in the response of Thermo-Elastic ATVA with temperature: (a) heating; (b) cooling.

——— f_a, 1st attempt; ·········· f_a, 2nd attempt; - - - - - - f_r, 1st attempt; - · - · - f_r, 2nd attempt.

Appendix 5: The Simulink Model of the Gradient Descent Algorithm

The Simulink model implemented for the numerical simulations includes 4 main blocks. These are, a block that generates an incident wave at a frequency f which can change with time, a block "ATVA/Beam" that simulates the behaviour of an absorber attached to a beam, a block "Signal Processing" which obtain the reference signals s_1 and s_2 from the signals acquired from two sensors located at the optimum spacing form the ATVA and a block that finds the error function e_3 and applies the gradient descent algorithm.

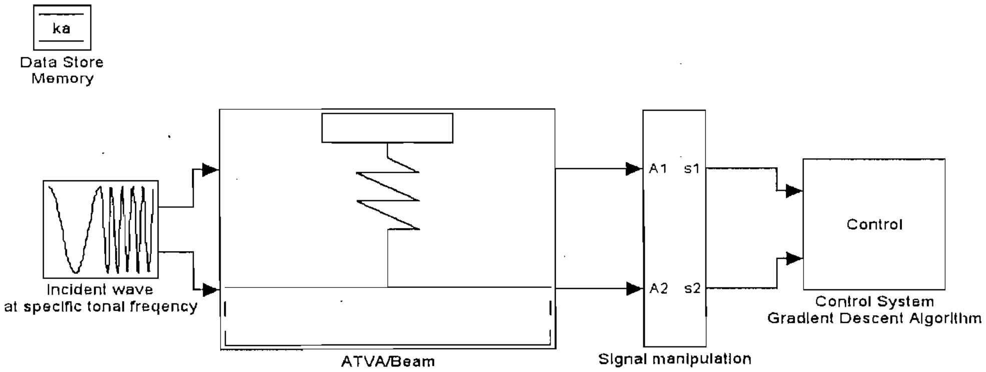

1- Subsystem of ATVA/Beam

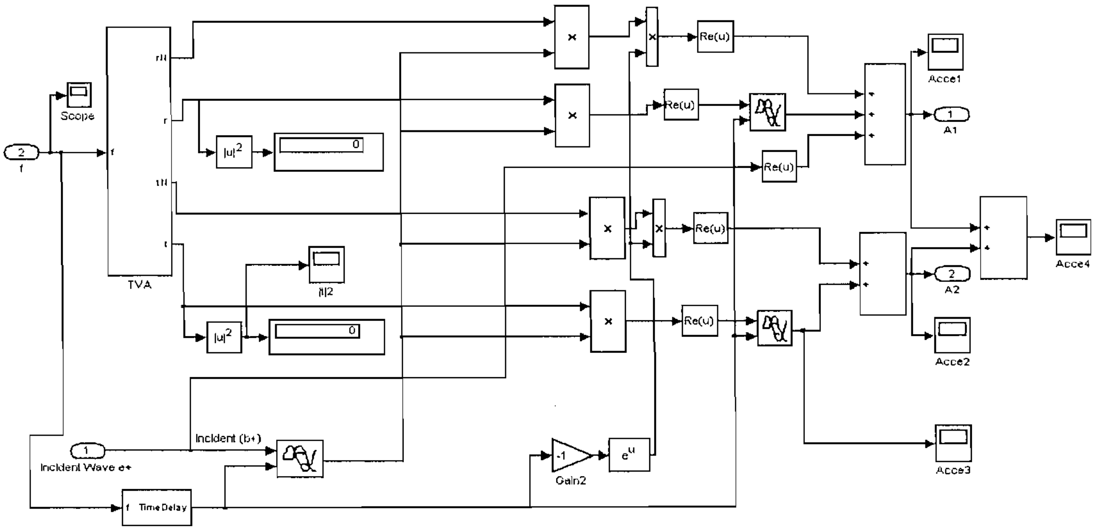

2- Subsystem of TVA

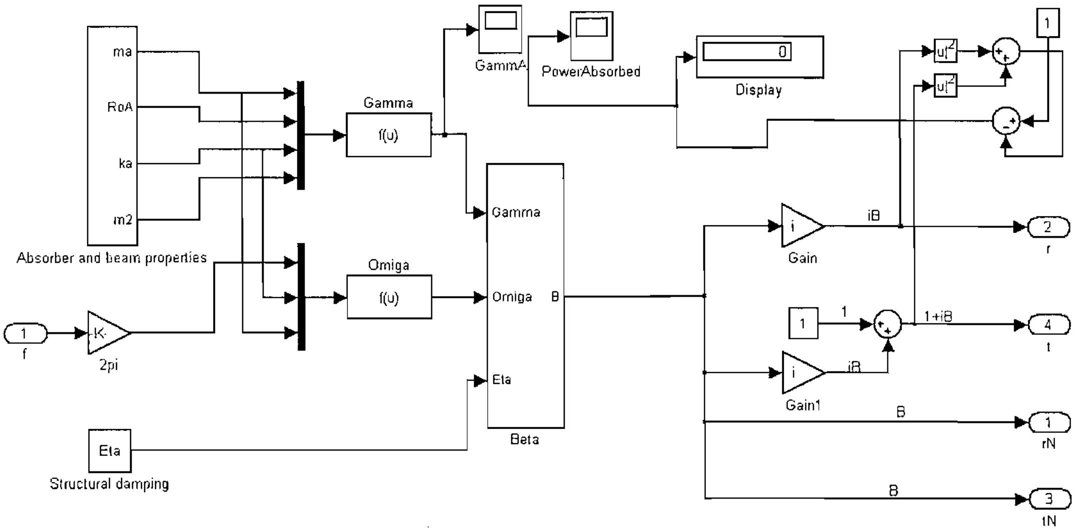

3- Subsystem of the absorber and beam properties

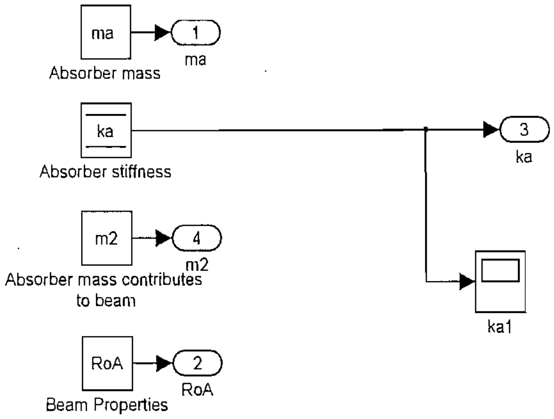

4- Subsystem of the signal processing

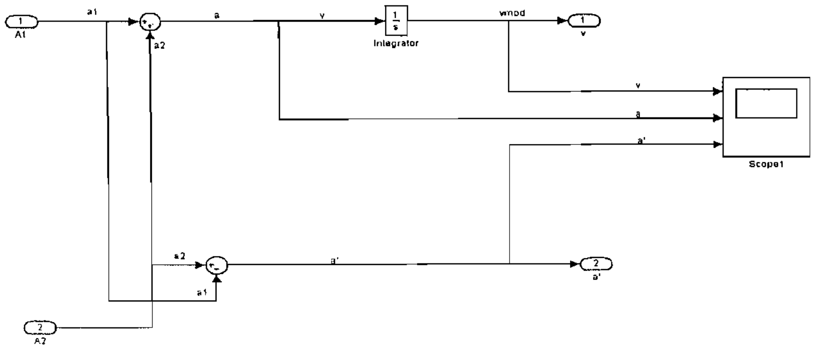

5- Subsystem of the control decision

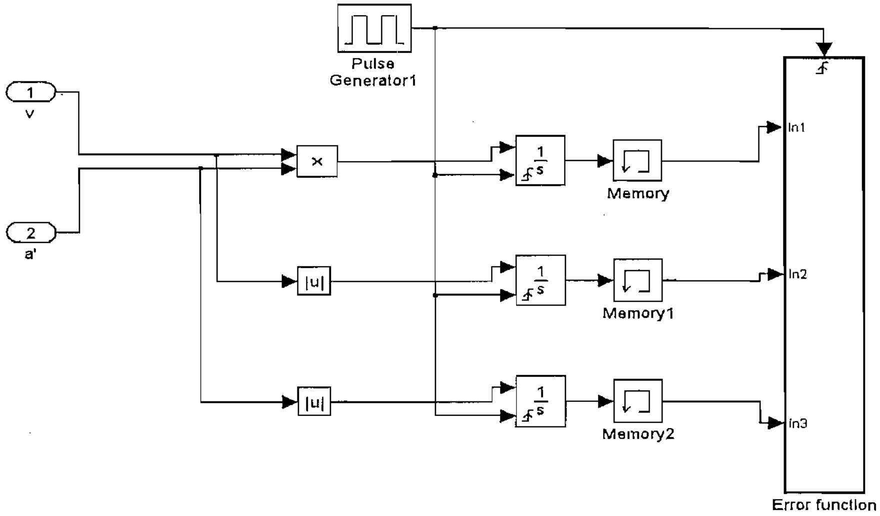

6- Subsystem of the error function

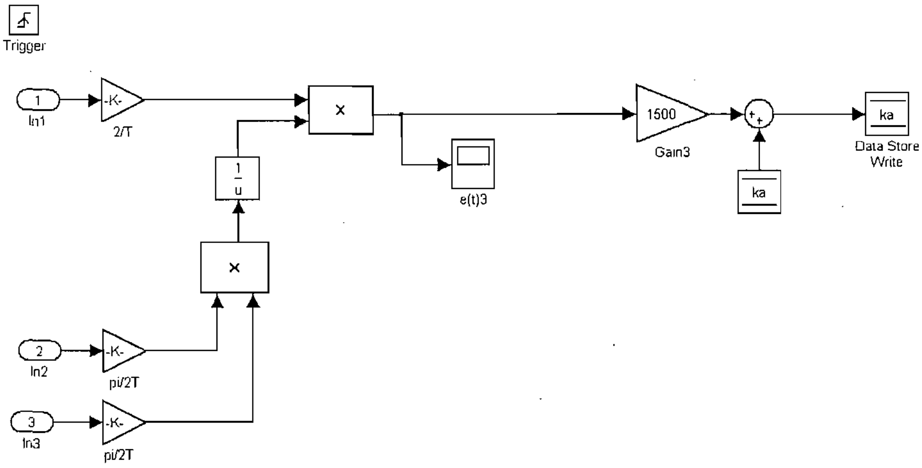

Appendix 6: Transmission Ratios and Corresponding Error Functions

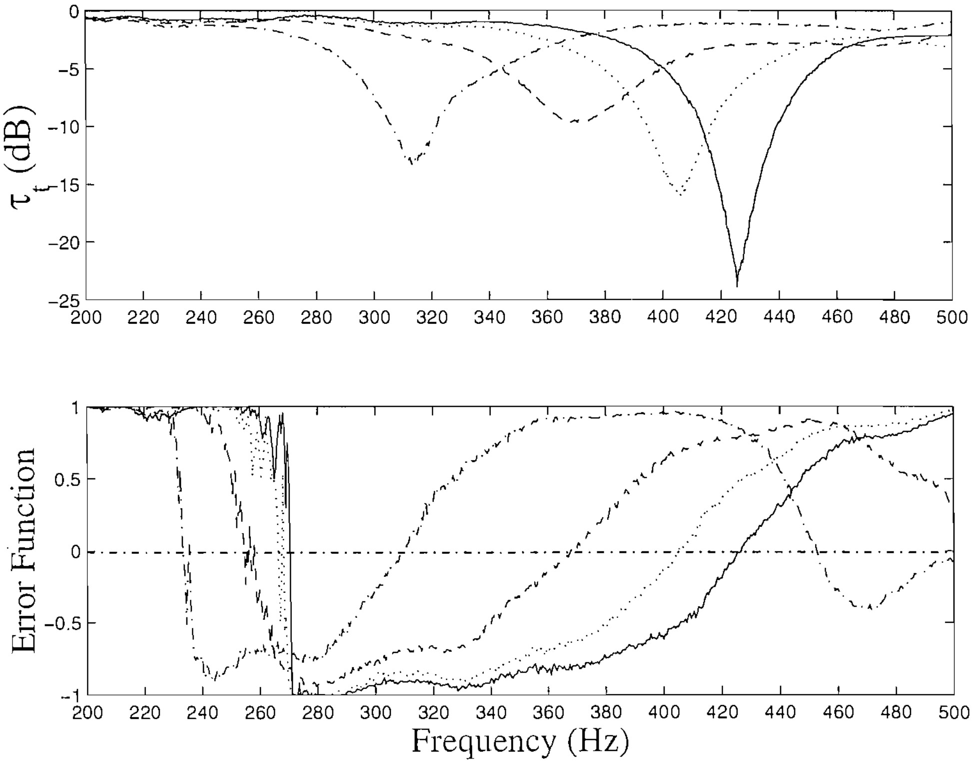

Appendix 6. Transmission ratios and corresponding error functions obtained experimentally by cooling down the Thermo-Elastic ATVA: (a) τ_t ; (b) e_3 .

——— $T_a = 20°C$;............ $T = 34.4°C$;------ $T = 46°C$;-.-.-.-. $T = 69°C$

Appendix 7: The Simulink Model Implemented Experimentally

The model implemented experimentally is similar to that shown in Appendix 5 except that there is no excitation block or the ATVA/Beam block. Changes mainly applies to the Signal Processing block (high pass digital filers) and to Control block (current is changed rather than stiffness).

1- Subsystem of the signal processing block

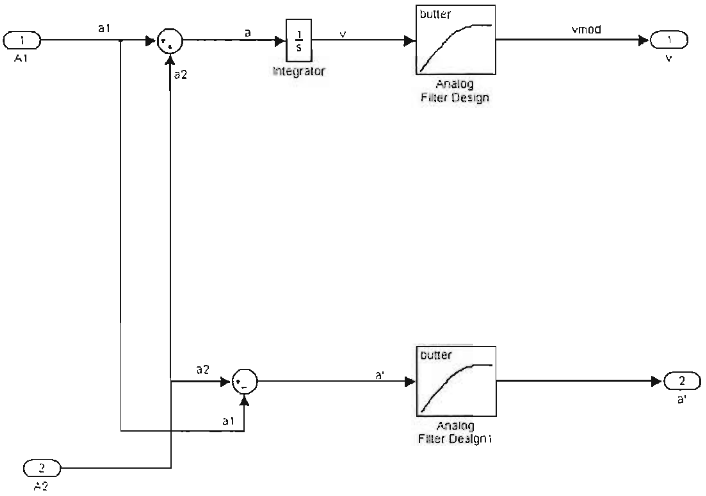

2- Subsystem of the error function

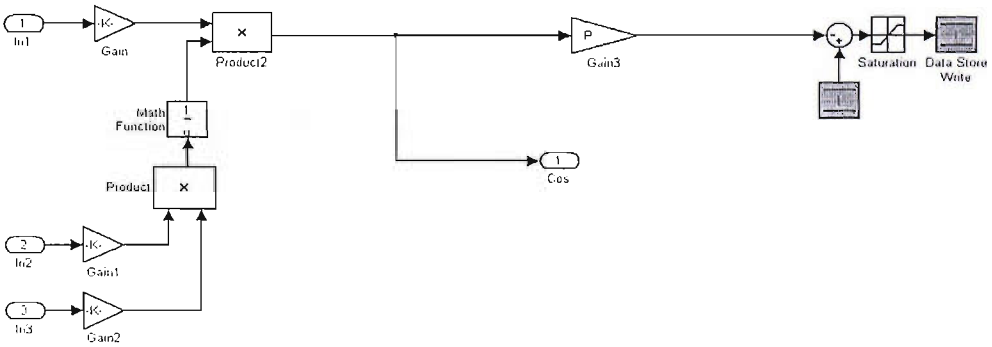

GLOSSARY OF TERMS

A = cross sectional area

A_s = start of austenitic phase

A_f = finish of austenitic phase

A_1 = point acceleration of the beam at the upstream nearfield position

A_2 = point acceleration of the beam at the downstream nearfield position

A_3 = point acceleration of the beam at the downstream farfield position

a = wave amplitude at point force

b = wave amplitude at absorber location

c = wave amplitude transmitted downstream

c_f = phase velocity of flexural wave

c_l = phase velocity of longitudinal wave

c_t = damping constant

d = diameter of wire

E = young's modulus

e = error function

EI = beam flexural rigidity

F = amplitude of harmonic force

f = frequency (Hz)

f_a = absorber frequency

f_r = anti-resonance frequency

$\mathbf{I}$ = identity matrix

I = electric current; second moment of area

i = $\sqrt{-1}$ complex operator; structural intensity

k = wavenumber

k_a = stiffness of absorber

$\bar{k}_t$ = spring stiffness

l = distance along the beam

M = bending moment
M_b = mass of the cantilever beam
M_e = mass of the concentrated block at the end of the cantilever
M_f = finish of martensitic phase
M_s = start of martensitic phase
m = mass
m_a = effective mass of absorber
m_b = mass of absorber that contributes to mass of the beam
n = any integer
P = control constant of the gradient descent algorithm
P_a = power absorbed by vibration absorber per input power
Q = shear force
$\mathrm{Re}\{\ \}$ = real part
$\mathbf{r}$ reflection matrix
r = reflection coefficient; radius of rod
S = slope; amplitude of the reference signal s
s = reference signal for the error function
T_g = glass transition temperature
$\mathbf{t}$ = transmission matrix
t = transmission coefficient; time
u = longitudinal displacement
w = transverse replacement
w' = angular displacement
$\dot{W}$ = velocity amplitude
$\dot{w}$ = velocity
$\ddot{w}$ = acceleration
$\ddot{W}'$ = angular acceleration amplitude
$\ddot{w}'$ = angular acceleration
x = longitudinal position
y = displacement of absorber mass

Z = dimensionless impedance

$\overline{Z}$ = point impedance

Z_{beam} = beam impedance

Z_{TVA} = absorber impedance

β = variable factor – equation (3.12)

γ = absorber mass/beam mass in a length of $2\lambda_a / \pi$

Δ = spacing between two accelerometers

Δ_{opt} = optimum spacing

Δ_c = critical spacing

δ = uniform elastic element of one dimensional structure

η = absorber loss factor

κ_e = even integer

κ_o = odd integer

λ = wavelength

λ_a = wavelength at absorber frequency

μ = effect of translational constraint

ξ = martensitic fraction

ρ = density

σ_x = axial stress

τ_t = transmission ratio

τ_r = reflection ratio

$\Delta\Phi$ = phase change

ϕ = relative phase

$\Delta\Omega$ = frequency bandwidth of attenuation

Ω = ratio of excitation frequency to absorber frequency ω / ω_a

Ω_1 = lower-half power point

Ω_2 = upper-half power point

Ω_b = frequency ratio at which maximum power absorption occurs

Ω_m = frequency ratio at which power transmission is maximum

Ω_t = tuned frequency ratio

ω = circular frequency (rad/sec)

ω_a = natural frequency of the absorber $\sqrt{k_a / m_a}$

Note that the subscripts used for propagating and nearfield waves are listed below:

$+$ = positive – going wave

$-$ = negative – going wave

N = nearfield

REFERENCES

[1] H. Frahm, Device for damping vibrations of bodies, US Patent No. 989 958, 1911.

[2] J. Ormandroyd and J.P. Den Hartog, Theory of the dynamic vibration absorber, *Transactions of the American Society of Mechanical Engineers*, (1928) 9-22.

[3] J.P. Den Hartog, *Mechanical Vibrations*, McGraw-Hill, New York, 1956.

[4] J.Q. Sun, M.R. Jolly and M.A. Norris, Passive, adaptive and active tuned vibration absorbers – a survey, *Transactions of the American Society of Mechanical Engineers*, 117 (1995) 234-242.

[5] J.B. Hunt, *Dynamic Vibration Absorbers*, Mechanical Engineering Publications Ltd, London, 1979.

[6] R.J. Bernhard, H.R. Hall and J.D. Jones, Adaptive-passive noise control, *Proceedings of Inter-Noise 92*, Toronto, Canada, 20–22 July 1992, pp. 427-430.

[7] A.H. Von Flotow, A. Beard and D. Bailey, Adaptive tuned vibration absorbers: tuning laws, tracking agility, sizing, and physical implementations, *Proceedings of Noise-Con 94*, Ft. Lauderdale, Florida, USA, 1-4 May 1994, pp. 437-454.

[8] M.A. Franchek, M.W. Ryan and R.J. Bernhard, Adaptive passive vibration control. *Journal of Sound and Vibration* 189(5) (1995) 565-585. doi:10.1006/jsvi.1996.0037

[9] M. Blaszkiewicz, R.E. Newnham and Q.C. Xu, Tunable transducers as smart materials, *Transactions of the Institute of Electrical and Electronic Engineers*, 91CH2817, pp.899-913, 1991.

[10] C.L. Davis and G.A. Lesieutre, An actively tuned solid-state vibration absorber using capacitive shunting of piezoelectric stiffness. *Journal of Sound and Vibration* 232(3) (2000) 601-617.doi:10.1006/jsvi.1999.2755.

[11] N.W. Hagwood and A.H. Von Flotow, Damping of structural vibrations with piezoelectric materials and passive electrical networks. *Journal of Sound and Vibration* 146(2) (1991) 243-268. doi:10.1016/0022-460X(91)90762-9

[12] E. Rustighi, M.J. Brennan and B.R. Mace, Design of an adaptive vibration absorber using shape memory alloy, ISVR Technical Memorandum No. 920, 2003.

[13] K. Williams, G. Chiu and R. Bernhard, Adaptive-Passive absorbers using shape-memory alloys. *Journal of Sound and Vibration*, 249(5) (2002) 835-848. doi:10.1006/jsvi.2000.3496.

[14] P.L. Walsh and J.S. Lamancusa, A variable stiffness vibration absorber for minimisation of transient vibrations. *Journal of Sound and Vibration* 158(2) (1992) 195-211. doi:10.1016/0022-460X(92)90045-Y

[15] M.J. Brennan, Actuators for active vibration control-tunable resonant devices. *Journal of Applied Mechanics and Engineering*, 5(1) (2000) 63-74.

[16] M.R.F. Kidner and M.J. Brennan, Variable stiffness of a beam-like neutraliser under fuzzy logic control, *Transactions of the American Society of Mechanical Engineers*, *Journal of Vibration and Acoustics* 124 (2002) 90-99.

[17] D.P Hong and Y.S. Ryu, Automatically controlled vibration absorber, US patent No. 4935651, 1985.

[18] M.A. Franchek, M.W. Ryan and R.J. Bernhard, Adaptive passive vibration control. *Journal of Sound and Vibration*, 189(5) (1995) 565-585. doi:10.1006/jsvi.1996.0037

[19] J.P. Carneal, F. Charette and C.R. Fuller, Minimization of sound radiation from plates using adaptive tuned vibration absorbers. *Journal of Sound and Vibration* 270(4-5) (2004) 781-792. doi:10.1016/S0022-460X(03)00257-8

[20] P. Bonello, M.J. Brennan and S.J. Elliot, Vibration control using a tunable vibration absorber with a variable shape stiffness element, *Proceedings of the Institute of Acoustics*, Spring Conference, Vol. 26, University of Southampton, 29-30 March 2004, pp. 534-545.

[21] J.M. Cronje, P.S. Heyns, N.J. Theron and P.W. Loveday, Development of a variable stiffness spring for adaptive vibration isolators, *Proceedings of the International Society for Optical Engineering*, Smart Structures and Materials, Vol. 5386, The Pennsylvania State University, July 2004, pp. 33-40.

[22] T. Long, M.J. Brennan and S.J. Elliot, Design of smart machinery installations to reduce transmitted vibrations by adaptive modification of internal forces, *Proceedings of the Institution of Mechanical Engineers. Journal of Systems and Control Engineering* 212(3) (1998) 215-228.

[23] J.S. Lai and K.W. Wang, Parametric control of structural vibrations via adaptable stiffness dynamic absorbers, *Transactions of the American Society of Mechanical Engineers. Journal of Vibrations and Acoustics* 118 (1996) 41-46.

[24] M.R.F. Kidner and M.J. Brennan, Real-time control of both stiffness and damping in an active vibration neutralizer. *Journal of Smart Materials and Structures, Institute of Physics Publishing* 10(4) (2001) 758-769.

[25] S.J. Elliot and L. Billet, Adaptive control of flexural waves propagating in a beam. *Journal of Sound and Vibration* 163(2) (1993) 295-310. doi:10.1006/jsvi.1993.1166

[26] C.R. Halkyard and B.R. Mace, Feedforward adaptive control of flexural vibration in a beam using wave amplitudes. *Journal of Sound and Vibration* 254 (2002) 117-141. doi:10.1006/jsvi.2001.4089

[27] N.R. Harland, R. W. Jones and B.R. Mace, Auto-tuning of a tunable structural insert. *Proceedings of the International Conference on Noise and Vibration Engineering,* Leuven, Belgium, 16-18 September 2002, PMA, 8pp.

[28] N.R. Harland, B.R. Mace, R.W. Jones and C.R. Halkyard, Control of vibration transmission using a tunable fluid filled beam inserts, *Proceedings of the International Symposium on Active Control of Sound and Vibration*, Fort Lauderdale, Florida, USA, December 1999, pp. 145-156.

[29] P. Clark, Devices for reduction of pipeline vibration, PhD Thesis, University of Southampton, 1995.

[30] M.J. Brennan, Control of flexural waves on a beam using a tunable vibration neutraliser. *Journal of Sound and Vibration* 222(3) (1998) 389-407. doi:10.1006/jsvi.1998.2031

[31] L. Jacobsen and R. Ayre, *Engineering Vibrations with Applications to Structures and Machinery*, McGraw-Hill, New York, 1958.

[32] W. Gough, J.P.G. Richards, R.P. Williams, *Vibrations and Waves*, Ellis Horwood, Chichester, 1983.

[33] L. Cremer, M. Heckl and E.E. Ungar, *Structure-borne Sound*, Springer – Verlag, New York, 1973.

[34] R.E.D. Bishop and D.C. Johnson, *Mechanics of Vibration*, Cambridge University press, 1960.

[35] C.R. Fuller, S.J. Elliot and P.A. Nelson, *Active Control of Vibration*, Academic Press Limited, London, 1996.

[36] C. L. Morfey, *Dictionary of Acoustics*, Academic press, London, 2001.

[37] K.F. Graff, *Wave Motion in Elastic Solids*, Dover Publications Inc., New York, 1975.

[38] B.R. Mace, Wave reflection and transmission in beams. *Journal of Sound and vibration* 97(2) (1984) 237-246. doi:10.1016/0022-460X(84)90320-1

[39] YU.I. Bobrovnitskii, On the energy flow in evanescent waves. *Journal of Sound and Vibration* 152 (1992) 175-176. doi:10.1016/0022-460X(92)90073-7

[40] S. Timoshenko, D.H. Young and W. Weamer, *Vibration Problems in Engineering*, John Wiley and Sons Inc., 4th Edition, 1974.

[41] B.R. Mace and C.R. Halkyard, Time domain estimation of response and intensity in beams using wave decomposition and reconstruction. *Journal of Sound and Vibration* 230(3) (2000) 561-589. doi:10.1006/jsvi.1999.2630

[42] C.R. Halkyard and B.R. Mace, Structural intensity in beams – waves, transducer systems and the conditioning problem. *Journal of Sound and Vibration* 185(2) (1995) 279-298. doi:10.1006/jsvi.1995.0380

[43] B.R. Mace, The effects of transducer inertia on beam vibration measurements. *Journal of Sound and Vibration* 145(3) (1991) 365 – 379. doi:10.1016/0022-460X(91)90108-V

[44] D.J. Mead, *Noise and Vibration* (R.G. WHITE and J.G. WALKER, editors), Chapter 9: Structural wave motion, Ellis Horwood Publishers, Chichester, 1982.

[45] J. Horner, Vibrational power transmission in beam-like structures, PhD Thesis, University of Southampton, 1990.

[46] R.G. Meadows, *Electric Network Analysis*, Chapter 6: Network theorems, equivalence and reduction, Penguin Education, 1972.

[47] M.J. Brennan, Vibration control using a tunable vibration neutraliser, *Proceedings of the Institution of Mechanical Engineers, Journal of Mechanical Engineering Science* 211 (1997) 91-108.

[48] C. Ting-Kong, Design of an adaptive dynamic vibration absorber, MSc thesis, University of Adelaide, 1999.

[49] S.S. Rao, *Mechanical Vibrations*, Prentice Hall, 3rd Edition, 1995.

[50] E.L. Hixson, *Shock and Vibration Handbook* (C. Harris and C. Crede, editors), Chapter 10: Mechanical impedance and mobility, McGraw-Hill, New York, 1976.

[51] D.J. Ewins, *Modal Testing: theory, practice and applications*, Research Studies Press Ltd., Hertfordshire, England, 2nd Edition, 2000.

[52] A.V. Srinivasan and D.M. McFarland, *Smart Structures*: analysis and design, Cambridge University press, 2001.

[53] N.D. Sims, R. Stanway and A.R. Johnson, Vibration control using smart fluids: a state-of-the-art review, *Proceedings of the Shock and Vibration Digest*, Vol. 31(3), 1999, pp. 195-203.

[54] J. Wang and G. Meng, Magnetorheological fluid devices: principles, characteristics and applications in mechanical engineering, *Proceedings of the Institution of Mechanical Engineers, Journal of Materials: Design and Applications – Part L* 215(3) (2001) 165-174.

[55] A. Olander, The crystal structure of Au-Cd-Zn. *Kristolograph* 83 (1932) 145-148.

[56] W.J. Buehler, R.C. Wiley and F.E. Wang, Nickel-Based Alloys, U.S. Patent No. 3,174,851, 1965.

[57] S.B. Basavaraj, A.K. Sudhakar and M.B. Kamal, A review on shape memory alloy structures. *International Journal of Acoustics and Vibration* 9(2) (2004) 61-68.

[58] W.B. Cross, A.H. Kariotis and F.J. Stimler, Nitinol characterisation study, NASA, CR-1433, Hampton, Virginia, 1970.

[59] D.C. Lagoudas, J.J. Mayes and M.M. Khan, Simplified shape memory alloy (SMA) material model for vibration isolation, *Proceedings of the International Society for Optical Engineering, 8th Annual International Symposium on Smart Structures and Materials*, Vol. 4326, Newport Beach, CA-USA, August 2001, pp. 452-461.

[60] C. Liang and C.A. Rogers, Design of shape memory alloy springs with applications in vibration control, *Transactions of the American Society of Mechanical Engineers, Journal of Vibration and Acoustics* 115 (1993) 129-135.

[61] K.A. Williams, G.T.-C Chiu and R.J. Bernhard, Dynamic modelling of a shape memory alloy adaptive tuned vibration absorber. *Journal of Sound and Vibration*, In press, Corrected Proof (2004). doi:10.1016/j.jsv.2003.12.040.

[62] J. Uchil, K.P. Mohanchandra, K.K. Mahesh and K.G. Kumara, Thermal and electrical characterization of R-phase dependence on heat-treat temperature in Nitinol. *Journal of Physica B: Condensed Matter* 253(1-2) (1998) 83-89. doi:10.1016/S0921-4526(98)00378-0

[63] S.K. Wu and H.C. Lin, Recent development of TiNi-based shape memory alloys in Taiwan. *Materials Chemistry and Physics* 64(2) (2000) 81–92. doi:10.1016/S0254-0584(99)00258-8

[64] M.C. Piedboeuf and R, Gauvin, Damping behaviour of shape memory alloys: strain amplitude, frequency and temperature effects. *Journal of Sound and Vibration* 214(5) (1998) 885-901. doi:10.1006/jsvi.1998.1578

[65] Compiled by Technolex , *Thermoset Resins for Composites*, Directory & Databook, Woodhead Publishing, 2nd Edition, 1998.

[66] P.F. Bruins, *Epoxy Resin Technology*, Interscience Publishers, 1968.

[67] Forest Products Laboratory, *Wood Handbook*: Wood as an engineering material, United States Department of Agriculture, General Technical Report, FPL-GTR-113.Chapter 4: mechanical properties of wood, 1999.

[68] J.H. Stephens, *Kempe's Engineers Year-Book*, Published by Miller Freeman, UK, 1997.

[69] P.E. Wellstead and M.B. Zarrop, *Self-tuning Systems*: control and signal processing, Chapter 1: Introduction, John Wiley and sons, 1st Edition, 1991.

[70] D.W. Clarke, *Self-tuning and Adaptive Control*: theory and applications (C.E. Harris and S.A. Billings, editors), Chapter 2: Introduction to self-tuning controllers, Peter Peregrinus Ltd., London, UK, 1981, re-issued 1985.

[71] P.A. Nelson and S.J. Elliott, *Active Control of Sound*, Academic Press Limited, Harcourt Brace & Company, Publishers, London, 1992.

[72] W.A. Gruver and E. Sachs, *Algorithmic Methods in Optimal Control*, Pitman Publishing Limited, London, 1980.

[73] R.C. Dorf and R.H. Bishop, *Modern Control Systems*, Pearson Prentice Hall 10th Edition, 2005.

[74] Simulink® - Help, The MathWorks, Inc., Matlab ® v6.1, Release 12.1, May 2001.

[75] S. Sato and H. Matsuhisa, Semi-active noise control by a resonator with variable parameters. *Proceedings of Inter-Noise 90*, Gothenburg, Sweden, 13-15 August 1990, pp. 1305-1308.

[76] C. Buhr, M.A. Franchek and R.J. Bernhard, Non-collocated adaptive-passive vibration control. *Journal of Sound and Vibration* 206(3) (1997) 371-398.

[77] M.J. Brennan, S.J. Elliot and T. Long, Automatic control of multiple tuned vibration neutralisers, *Proceedings of Inter-Noise*, 25th anniversary congress-Liverpool, UK, 30 July – 2 August 1996, pp. 1597-1602.

[78] R. Bracewell, *The Fourier Transform and its Applications*, McGraw-Hill, New York, 3rd edition, 1999.

LIST OF PUBLICATIONS

[1] H.M. El-Khatib, B.R. Mace and M.J. Brennan, Wave reflection and transmission in thin beams in the presence of undamped absorber, ISVR Technical Memorandum No. 903, 2003.

[2] H.M. El-Khatib, B.R. Mace and M.J. Brennan, Wave amplitude measurement in beams in the presence of a nearfield, ISVR Technical Memorandum No. 909, 2003.

[3] B.R. Mace, C.R. Halkyard and H.M. El-Khatib, Real-time measurement of wave amplitudes and intensity in a beam in the presence of a nearfield. *Journal of Sound and Vibration, In Press, Corrected Proof, Available online 5 January 2005*. doi:10.1016/j.jsv.2004.10.017

[4] H.M. El-Khatib, B.R. Mace and M.J. Brennan, The effects of a nearfield on the performance of tunable vibration absorbers in beam structures, *Proceedings of the VIIIth International Conference on Recent Structural Dynamics*, 14-16 July 2003, Southampton – UK, WIP 2.

[5] H.M. El-Khatib, B.R. Mace and M.J. Brennan, Suppression of bending waves in a beam using a tuned vibration absorber. *Accepted in Journal of Sound and Vibration YJSV: 7183 (2005).*

[6] H.M. El-Khatib, B.R. Mace and M.J. Brennan, Bending wave control in beams using a tunable vibration absorber, *Proceedings of the Institute of Acoustics*, Spring Conference, Vol. 26, University of Southampton, 29-30 March 2004, pp. 546-554.

[7] H.M. El-Khatib, B.R. Mace and M.J. Brennan, Control of bending waves in beam structure using an adaptive-passive vibration absorber, *Proceedings of The Eleventh International Congress on Sound and Vibration,* 5-8 July 2004, St. Petersburg, Russia, pp. 3455-3462